

Universiteit
Leiden
The Netherlands

Smoothly breaking unitarity : studying spontaneous collapse using two entangled, tuneable, coherent amplifiers

Reep, T.H.A. van der

Citation
Reep, T. H. A. van der. (2019, June 13). *Smoothly breaking unitarity : studying spontaneous collapse using two entangled, tuneable, coherent amplifiers*. *Casimir PhD Series*. Retrieved from https://hdl.handle.net/1887/73911

Version:	Not Applicable (or Unknown)
License:	Leiden University Non-exclusive license
Downloaded from:	https://hdl.handle.net/1887/73911

Note: To cite this publication please use the final published version (if applicable).

Cover Page



Universiteit Leiden



The handle http://hdl.handle.net/1887/73911 holds various files of this Leiden University dissertation.

Author: Reep T.H.A. van der
Title: Smoothly breaking unitarity : studying spontaneous collapse using two entangled, tuneable, coherent amplifiers
Issue Date: 2019-06-13

Smoothly breaking unitarity

Studying spontaneous collapse using two entangled, tuneable, coherent amplifiers

PROEFSCHRIFT

ter verkrijging van
de graad van Doctor aan de Universiteit Leiden,
op gezag van Rector Magnificus prof. mr. C.J.J.M. Stolker,
volgens besluit van het College voor Promoties
te verdedigen op donderdag 13 juni 2019
klokke 16.15 uur

door

Thomas Hendrik Abraham van der Reep

geboren te Rotterdam
in 1989

Promotor:	Prof. dr. ir. T.H. Oosterkamp
Promotiecommissie:	Prof. dr. H. Ulbricht (University of Southampton, United Kingdom)
	Prof. dr. G.A. Steele (Technische Universiteit Delft)
	Prof. dr. E.R. Eliel
	Prof. dr. M.A.G.J. Orrit
	Dr. M.J.A. de Dood

Casimir PhD series, Delft-Leiden 2019 – 21
ISBN: 978 – 90 – 8593 – 397 – 7

An electronic version of this thesis can be found at
https://openaccess.leidenuniv.nl

The work described in this thesis was performed at the Huygens-Kamerlingh Onnes Laboratory, Universiteit Leiden, Niels Bohrweg 2, 2333 CA, Leiden and at the Faculty of Applied Sciences, Technische Universiteit Delft, Lorentzweg 1, 2628 CJ, Delft.

Part of this research is supported by the NanoFront consortium, a programme of the Netherlands Organisation for Scientific Research (NWO) that is funded by the Dutch ministry of Education, Culture and Science (OCW).

Cover design by Tijs Hol – *What is large?* The cover visualises the underlying idea of this thesis. It shows an artist's impression of a phase space representation of a quantum state with pointers (measurement apparatuses). The larger the pointer, the more likely it is that a measurement of the state takes place, as indicated by the transparency of the pointers.

Copyright© 2019 T.H.A. van der Reep

Printed by Ridderprint BV

Contents

1 Introduction **1**
- 1.1 Setting the stage: the measurement problem and the photodetector 2
- 1.2 Interpretations of quantum state collapse 3
  - 1.2.1 The Copenhagen interpretation 3
  - 1.2.2 Bohmian Mechanics 4
  - 1.2.3 Many-worlds interpretation 4
  - 1.2.4 Environmental decoherence 5
  - 1.2.5 Spontaneous collapse 6
- 1.3 Undressing the photodetector: the parametric amplifier 6
- 1.4 Overview of the thesis 8
- References 9

2 Elements of microwave technology **11**
- 2.1 Introduction 12
- 2.2 Microwave transmission line theory 12
- 2.3 Microwave reflection 14
  - 2.3.1 Non-impedance-matched, dispersionless transmission lines 14
  - 2.3.2 Reflection planes 17
- 2.4 Coplanar waveguides 18
- 2.5 Microwave resonators (CPW) 20
- References 21

3 A mesoscopic Hamiltonian for Josephson travelling-wave parametric amplifiers **23**
- 3.1 Introduction 24
- 3.2 Terminology 25
- 3.3 The non-degenerate parametric amplifier with undepleted degenerate pump – classical theory 28
  - 3.3.1 Effect of phase matching 31
- 3.4 Quantum theory of parametric amplification (4WM) 33
  - 3.4.1 Energy in transmission lines 33
  - 3.4.2 Quantisation of a non-dispersive transmission line . . . 34

3.4.3 The influence of the Josephson capacitance: quantisation of a dispersive transmission line . . . 36
3.4.4 Adding the non-linearity: quantisation of a non-linear transmission line . . . 39
3.5 Implementations . . . 42
3.5.1 The non-degenerate parametric amplifier with undepleted degenerate classical pump – quantum theory . . . 42
3.5.2 Other implementations . . . 46
3.6 Paramp terminology – revisited . . . 48
3.7 Marrying the quantum and classical theories . . . 49
3.8 Validity . . . 50
3.9 Conclusions . . . 52
References . . . 53

4 An experimental proposal to study spontaneous collapse of the wave function using two travelling-wave parametric amplifiers 57
4.1 Introduction . . . 58
4.2 Model – lossless case . . . 59
4.3 Interference visibility . . . 61
4.4 The effect of losses . . . 62
4.5 Observing spontaneous collapse . . . 65
4.5.1 Collapse onto a number state . . . 65
4.5.2 Collapse onto a coherent state . . . 66
4.6 Experimental realisation and feasibility . . . 67
4.7 Conclusions . . . 70
References . . . 71
Appendices . . . 73
A Experimental realisation using resonator-based parametric amplifiers . . . 73
B Non-degenerate vs. degenerate amplifiers . . . 73
C Analytical model . . . 74
D Output of numerical calculations . . . 77
E Definition of interference visibility . . . 77
F Comparison of full and reduced Hilbert space . . . 77
G Interference visibility with losses . . . 78
H Interference visibility with collapse onto coherent states 81

5 Developing a travelling-wave parametric amplifier with low insertion loss 85
5.1 Introduction . . . 86
5.2 Designing the TWPA . . . 86
5.2.1 Design considerations . . . 86
5.2.2 From coplanar waveguide to TWPA . . . 87
5.2.3 Sonnet calculations . . . 87
5.2.4 Analytical approximation . . . 88

5.3 Elements of fabrication 89
5.3.1 Josephson junctions 91
5.3.2 Low air bridges 98
5.4 TWPA813 99
5.4.1 Design and fabrication 100
5.4.2 Measurement set-up 102
5.4.3 Results – single-tone excitation 102
5.4.4 Results – double-tone excitation 117
5.5 Conclusions 119
References 121

Acknowledgements **125**

Samenvatting **127**

Curriculum vitae **133**

List of publications **135**

Chapter 1

Introduction

1.1 Setting the stage: the measurement problem and the photodetector

Upon measurement a quantum system collapses onto one of the eigenstates of the measurement operator. The measurement outcome is then given by the eigenvalue corresponding to this eigenstate.
This is one of the postulates of the Copenhagen interpretation of quantum mechanics. It divides the world into two realms – the microscopic realm of quantum systems governed by quantum mechanics and the macroscopic realm of classical systems (measurement apparatuses) governed by classical mechanics.

Quantum mechanics and classical mechanics contain intrinsically different views of the world around us. Classical mechanics is deterministic: in principle, if we know the positions and momenta of all particles in the universe, we can – with certainty – determine the state of the universe at any other time by Newton's laws. Contrarily, from our classical point of view, quantum mechanics is probabilistic: a quantum system can only be described in terms of a quantum state, from which we can theoretically determine averages, standard deviations etc. of physical properties. Practically, we can only determine these variables using a large set of identically-prepared quantum systems, as "follows" from the measurement postulate stated above. Moreover, for a single system we cannot even measure all its properties as dictated by Heisenberg's uncertainty relation. Yet, within the realm of quantum mechanics, a quantum system is perfectly deterministic. Its time-evolution is described by Schrödinger's equation, implying that we can, in principle, determine the quantum state of the universe at any time, if only we had access to its quantum state at a certain time and the Hamiltonian of the universe.

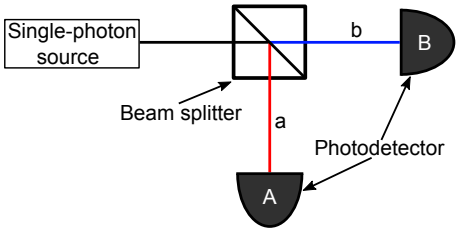


Figure 1.1: *Illustration of the quantum measurement problem. If a superposition of* 0 *and* 1 *photon is created using a single-photon source and a beam splitter, photodetectors A and B placed in the beam splitter's output arms a and b will either "click" or "not-click", whereas they should attain a superposition of clicking and not-clicking according to Schrödinger's equation that describes the unitary evolution of quantum states.*

Let us illustrate this by an example. Consider the set-up depicted in figure 1.1. A single photon, the archetype of a quantum system, is emitted by a single-photon source. The photon encounters a beam splitter, which "splits"

the single photon into a superposition of 0 and 1 photon in each of the outputs of the beam splitter. In this case, the photon state after the beam splitter can be deterministically described by the state vector

$$|\psi\rangle = \alpha\,|1\rangle_{\mathrm{a}}\,|0\rangle_{\mathrm{b}} + \beta\,|0\rangle_{\mathrm{a}}\,|1\rangle_{\mathrm{b}}\,, \tag{1.1}$$

where $|\alpha|^2$ and $|\beta|^2$ are the probabilities of finding the corresponding states upon measurement.
If this state is absorbed by the photodetectors connected to the outputs of the beam splitter, one of the detectors "clicks" to indicate it has detected the photon. That is, once one of the detectors has clicked, the state can be described by

$$|\psi\rangle_{\mathrm{d}} = |1\rangle_{\mathrm{A}}\,|0\rangle_{\mathrm{B}} \vee |\psi\rangle_{\mathrm{d}} = |0\rangle_{\mathrm{A}}\,|1\rangle_{\mathrm{B}}\,. \tag{1.2}$$

Hence, only one of the detectors, A or B, clicks, which is in contradiction with the deterministic quantum evolution of the system that implies that the detectors should be in a superposition of clicking and not-clicking. The latter behaviour, however, is never observed in experiments and it is precisely this observation that leads to the formulation of the measurement postulate, which is also known as the measurement problem.

The mystery of state collapse has been a much-debated issue since the conceivement of quantum mechanics in the 1920s. Some of the view points on this issue will be presented in section 1.2. However, with the advancement of technology, we envision that the time has come to address this matter in an experimental setting. One may wonder whether it is really the measurement apparatus that induces state collapse. To this end we will consider undressing the photodetector to a quantum device, a parametric amplifier, in section 1.3. An overview of the remainder of this thesis is presented in section 1.4.

1.2 Interpretations of quantum state collapse

Ever since the formulation of quantum mechanics, interpretations of the theory have been put forward. These interpretations often include a view on the process of quantum state collapse. In this section we will shortly discuss the phenomenology of some common views, including remarks about problems raised by the interpretations. For an extended review and literature overview, see [1].

1.2.1 The Copenhagen interpretation

The first interpretation of quantum theory was developed in the years 1925 to 1927 in Copenhagen and is therefore known as the Copenhagen interpretation [2]. It says that a measurement apparatus collapses a quantum state irreducibly and probabilistically to an eigenstate of the observed quantity. Moreover, after

a measurement, a state can be described in classical terms.
Although the Copenhagen interpretation does not provide an explanation for state collapse, it does introduce the notion of a measurement apparatus (without defining what it is) and that there is a clear distinction between the quantum realm and the classical realm.

1.2.2 Bohmian Mechanics

As a solution to the measurement problem, Bohm proposed an extension of quantum mechanics by a guiding equation [3, 4]. This equation determines the real position and momentum of a corpuscle, which is guided by the quantum wave function and is the source of this wave at the same instance. Then, within the example given in previous section, when the single-photon quantum state encounters the beam splitter and splits, the corpuscle, which makes a detector click, is situated only in one of the branches of the superposition. This would explain why only one of the detectors clicks and the other does not-click. Moreover, one of the detectors will click deterministically as the path followed by the corpuscle only depends on its initial conditions.
This approach to quantum state collapse has its merits as it removes the uncertainty from the quantum measurement. As a matter of fact, experiments have been conducted that have been claimed to support this interpretation [5, 6]. However, we find three objections. First, the corpuscle cannot be related to the particle it describes, since it has no properties except for a position and velocity [7–9]. This makes the theory unfalsifiable as, in absence of any corpuscle properties, there is no means of verifying the existence of such a corpuscle. Furthermore, we doubt that such a corpuscle can exist, because to all known particles at least an energy can be associated. Thirdly, we note that this interpretation merely replaces the problem by a different problem, because in order to predict the measurement outcomes, the corpuscles must have the right initial conditions. This implies that the measurement problem is replaced one-to-one by the quantum source problem.

1.2.3 Many-worlds interpretation

The many-worlds interpretation of quantum mechanics is due to Everett [10]. This interpretation postulates that also during and after the process of measurement the unitary evolution described by the Schrödinger equation determines the evolution of a quantum state. However, after measurement, the measurement outcomes live in different orthogonal "branches" of the universe, such that they will never interact again. If a measurement can attain two experimental outcomes, such as a detector clicking or not-clicking, this can be seen as the single photon encountering a beam splitter: in the many world interpretation the beam splitter plays the role of a measurement and the two output channels of the beam splitter can be thought of as the different branches of the universe. This interpretation might have difficulties with falsification, if one considers the

branching of universe as the fundamental aspect of the interpretation. Since the branches of the universe are orthogonal, we cannot detect the existence of a branched-off universe. That is to say, in analogy to the single photon and beam splitter, we cannot perform a measurement that acts as a second beam splitter which overlaps the two created universe branches again. However, this difficulty is erased if the unitary evolution described by Schrödinger's equation is considered as the core aspect of the theory. In that case the many-worlds interpretation would be falsified by either Bohmian mechanics (discussed above) or spontaneous collapse theories (discussed below), as these two interpretations require an extra ingredient to quantum evolution apart from the Schrödinger equation.

1.2.4 Environmental decoherence

Environmental decoherence describes the loss of quantum interference by interactions with the environment [11–13]. Consider the state matrix of the pure state described in equation (1.1) given by

$$\hat{\rho}_{\mathrm{p}} = |\psi\rangle\langle\psi| = \begin{bmatrix} |\alpha|^2 & \alpha\beta^* \\ \alpha^*\beta & |\beta|^2 \end{bmatrix}. \tag{1.3}$$

Due to coupling with the environment the off-diagonal terms in the state matrix exponentially tend to 0, leaving the mixed state $\hat{\rho}_{\mathrm{m}} = \mathrm{diag}(|\alpha|^2, |\beta|^2)$. Such processes have been observed in an experimental setting [14, 15].
The diagonal matrix $\hat{\rho}_{\mathrm{m}}$ is indistinguishable from a classical mixture and therefore it has been argued that it describes a collapsed state. However, strictly this is not the case: environmental decoherence only accounts for the destruction of quantum interference effects. It does not destroy the superposition of classical alternatives, as we will argue now.
Consider a set of marbles, let them be red and blue. If we draw a classical marble blindly (which is either red or blue) there is some probability of finding either colour. However, we know – since they are classical marbles – that the marble possessed that colour already before looking at it. However, in the case of quantum marbles, which are in a superposition of red and blue, the marble will decohere in our hand (the environment) before looking. Assuming the decoherence process lasts long enough to reduce the quantum marble's initial pure state $\hat{\rho}_{\mathrm{p}}$ to a final mixed state $\hat{\rho}_{\mathrm{m}}$, the state matrices of the classical and quantum marbles are the same before looking. However, although the classical and decohered state matrix are identical, for the quantum marble the colour is not necessarily determined before looking. In other words, although decoherence destroys the quantum mechanical interference phenomena of the system, it does not destroy the superposition of classical alternatives. This implies that environmental decoherence cannot account for the measurement problem.

1.2.5 Spontaneous collapse

As a last interpretation, we will discuss the idea of spontaneous collapse. Spontaneous collapse theories consider the option that the Schrödinger equation is incomplete and extend the evolution of a quantum state by a phenomenological collapse rate. The main idea is that every particle has an intrinsic collapse rate, which increases with particle mass. As such, the collapse rate of a single nucleon is small, such that it will behave according to the Schrödinger equation within the time frame of an experiment. Macroscopic particles, however, have such large collapse rates that the signatures of quantum mechanics are never observed in an experiment, because the quantum behaviour is too short-lived. In this view, the measurement problem can be thought of as a quantum system (with a small collapse rate) coupling to a measurement apparatus (with a large collapse rate). Thus the quantum system collapses due to the collapse rate that increases upon coupling.
The main disadvantage of this approach is that it is only phenomenological. There have been hypotheses developed as to what determines the collapse rate, mainly in the direction of trace dynamics [16] and gravity [17–19]. Proposals for the collapse rate (per nucleon) are orders of magnitude apart – the theory of Continuous Spontaneous Localisation (CSL) sets it at 10^{-17} Hz [20], whereas Adler estimates the collapse rate per nucleon at $10^{-8\pm2}$ Hz [21]. It is an area of active research to set bounds to the collapse rate [22–24].

1.3 Undressing the photodetector: the parametric amplifier

The interpretations presented in previous section are distinctly dissimilar in their view of quantum state collapse. However, they all agree that *large* systems appear to be classical, whereas microscopic systems behave quantum mechanically. From this notion an important question arises

What is large?

This question is currently approached by performing experiments on larger and larger physical systems to verify whether these systems behave according to quantum mechanics (see [25] for a review). At the moment of writing, systems of the size of small viruses have shown quantum mechanical behaviour [26] and an experiment testing the quantum behaviour of micrometre sized mirrors is being prepared [27].
Yet, in view of measurement apparatuses the question *What is large?* can be reformulated as

What is a measurement apparatus?

To illustrate, consider once more the experiment described in section 1.1. Now, suppose the photodetector is a photomultiplier tube (PMT), see figure 1.2. In PMTs an incoming photon causes a (primary) electron to emit from a cathode by the photoelectric effect. This electron is accelerated towards a dynode by an electric field. Due to the impact of the electron on the dynode, several (secondary) electrons are emitted. These, in turn, are accelerated towards a second dynode in which the process of electron multiplication is repeated. In the end, this results in a measurable current pulse of electrons arriving at the anode of the device.
Suppose now that a superposition of 0 and 1 photon, as described by equation (1.1) enters the PMT. Based on the postulate that measurements are responsible for quantum state collapse, one may wonder *where* during the amplification process within the PMT the state collapse happens, if it happens within the PMT at all. That is, at what point between the emission of the primary electron and the current pulse leaving the PMT the detector "decides" to click or not-click. Equivalently, one may wonder how many electrons are in superposition of remaining in and being emitted by a dynode when state collapse happens.

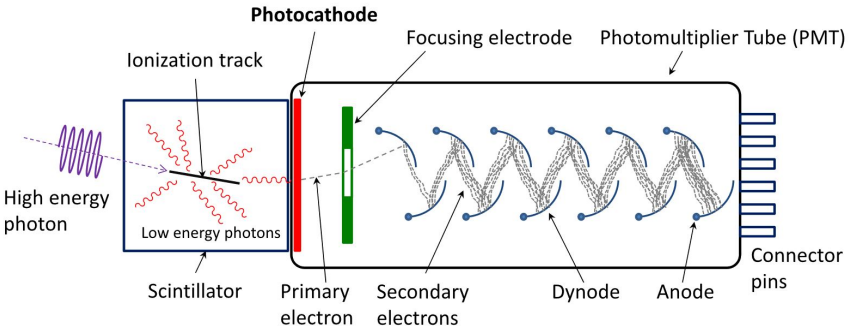


Figure 1.2: *Schematic overview of a photomultiplier tube (PMT). An incoming photon causes emission of an electron in the photocathode. This primary electron is accelerated by an electric field towards a dynode, where it causes the emission of several secondary electrons. This process is repeated to yield a measurable current pulse at the PMT's anode. A scintilator in front of the PMT may be used to decrease the effective energy of the incoming photon. Figure taken from [28].*

In this thesis we investigate an experiment addressing these questions. In principle, we could take the experimental set-up depicted in figure 1.1 and try to interfere the outputs of the two photodetectors. However, photodetectors are devices which are hard to describe within a quantum mechanical framework due to coupling to the environment and interfering their outputs is not at all trivial. However, the main characteristic of the photodetector – producing a click in the form of a detectable current by means of amplification when a photon enters

the device – can be mimicked by means of an electronic amplifier.
A certain class of electronic amplifiers, the so-called parametric amplifiers, is especially suited for this experiment. They produce gain due to non-linear wave mixing resulting from the variation of an amplifier parameter while the signal-to-be-amplified traverses the device. A parametric amplifier is tuneable in gain, can be quantum limited in noise figure and, most importantly, it can be described in quantum mechanical terms. Within an interferometer set-up we can interfere the outputs of two of such amplifiers which are entangled by feeding the interferometer with single photons. Building the whole set-up by use of superconducting devices, one can hope to achieve a sufficiently small coupling to the environment and add mass to the problem simultaneously. The latter occurs via the interaction of the electromagnetic waves transmitting through the set-up which are caused by the massive Cooper pairs in the superconducting transmission lines. By increasing the gain of the amplifiers, more and more Cooper pairs will partake in the quantum mechanical superposition, which can be seen as analogous to the increase in emitted electrons from the PMT dynodes.

1.4 Overview of the thesis

In this thesis we will take the first steps towards such an experiment. Chapter 2 presents a minimum background in microwave engineering as a basis for the rest of the thesis.
In chapter 3, a mesoscopic theory is developed that describes the process of non-linear wave mixing and the resulting gain in a transmission line embedded with Josephson junctions. Such a theory will be necessary to model the parametric amplifiers within a quantum mechanical framework correctly for the final experiment.
In chapter 4, we will present a prediction on the interference visibility that can be expected from an interferometer that has a parametric amplifier added to each of the interferometer arms. In this chapter we will also discuss the influence of losses in the interferometer on this visibility. This allows to estimate how small the coupling to the environment must be in order for the proposed experiment to work. Furthermore, we will argue how the interference visibility might change in case the quantum state collapses within the interferometer.
In the final chapter of this thesis, chapter 5, we present our findings on our attempts to develop a low-loss travelling-wave parametric amplifier. We present the design, fabrication procedure and findings from a transmitting device. The latter is used to validate the theory presented in chapter 3.

References

[1] A. Bassi, K. Lochan, S. Satin, T. P. Singh, and H. Ulbricht. Models of wave-function collapse, underlying theories, and experimental tests. *Rev. Mod. Phys.*, 85:471–527, 2013.

[2] N. Bohr. The quantum postulate and the recent development of atomic theory. *Nature*, 121:580–590, 1928.

[3] D. Bohm. A suggested interpretation of the quantum theory in terms of "hidden" variables. I. *Phys. Rev.*, 85:166–179, 1952.

[4] D. Bohm. A suggested interpretation of the quantum theory in terms of "hidden" variables. II. *Phys. Rev.*, 85:180–193, 1952.

[5] D. H. Mahler, L. Rozema, K. Fisher, L. Vermeyden, K. J. Resch, and A. Wiseman, H. M. Steinberg. Experimental non-local and surreal bohmian trajectories. *Sci. Adv.*, 2:e1501466, 2016.

[6] Y. Xiao, Y. Kedem, J.-S. Xu, C.-F. Li, and G.-C. Guo. Experimental nonlocal steering of bohmian trajectories. *Opt. Express*, 25:14463–14472, 2017.

[7] H. R. Brown, C. Dewdney, and G. Horton. Bohm particles and their detection in the light of neutron interferometry. *Found. Phys.*, 25:329–347, 1995.

[8] J. Anandan. The quantum measurement problem and the possible role of the gravitational field. *Found. Phys.*, 29:333–348, 1999.

[9] M. Esfeld, D. Lazarovici, V. Lam, and M. Hubert. The physics and metaphysics of primitive stuff. *Br. J. Philos. Sci.*, 68:133–161, 2017.

[10] H. Everett. "Relative state" formulation of quantum mechanics. *Rev. Mod. Phys.*, 29:454–462, 1957.

[11] H. D. Zeh. On the interpretation of measurement in quantum theory. *Found. of Phys.*, 1:69–76, 1970.

[12] A. O. Caldeira and A. J. Leggett. Influence of dissipation on quantum tunneling in macroscopic systems. *Phys. Rev. Lett.*, 46:211–214, 1981.

[13] E. Joos and H. D. Zeh. The emergence of classical properties through interaction with the environment. *Z. Phys. B*, 59:223–243, 1985.

[14] M. Brune, E. Hagley, J. Dreyer, X. Maître, A. Maali, C. Wunderlich, J. M. Raimond, and S. Haroche. Observing the progressive decoherence of the "meter" in a quantum measurement. *Phys. Rev. Lett.*, 77:4887–4890, 1996.

[15] S. Gerlich, L. Hackermüller, K. Hornberger, A. Stibor, H. Ulbricht, M. Gring, F. Goldfarb, T. Savas, M. Müri, M. Mayor, and M. Arndt.

A Kapitza—Dirac—Talbot—Lau interferometer for highly polarizable molecules. *Nat. Phys.*, 3:711–715, 2007.

[16] S. L. Adler. Generalized quantum dynamics. *Nucl. Phys. B*, 415:195 – 242, 1994.

[17] F. Karolyhazy. Gravitation and quantum mechanics of macroscopic objects. *Nuovo Cimento A*, 42:390–402, 1966.

[18] L. Diósi. A universal master equation for the gravitational violation of quantum mechanics. *Phys. Lett. A*, 120:377 – 381, 1987.

[19] R. Penrose. On gravity's role in quantum state reduction. *Gen. Rel. Gravit.*, 28:581–600, 1996.

[20] G. C. Ghirardi, P. Pearle, and A. Rimini. Markov processes in Hilbert space and continuous spontaneous localization of systems of identical particles. *Phys. Rev. A*, 42:78–89, 1990.

[21] S. L. Adler. Lower and upper bounds on CSL parameters from latent image formation and IGM heating. *J. Phys. A: Math. Theor.*, 40:2935–2957, 2007.

[22] S. Nimmrichter, K. Hornberger, and K. Hammerer. Optomechanical sensing of spontaneous wave-function collapse. *Phys. Rev. Lett.*, 113:020405, 2014.

[23] A. Vinante, M. Bahrami, A. Bassi, O. Usenko, G. Wijts, and T. H. Oosterkamp. Upper bounds on spontaneous wave-function collapse models using milliKelvin-cooled nanocantilevers. *Phys. Rev. Lett.*, 116:090402, 2016.

[24] A. Vinante, R. Mezzena, P. Falferi, M. Carlesso, and A. Bassi. Improved noninterferometric test of collapse models using ultracold cantilevers. *Phys. Rev. Lett.*, 119:110401, 2017.

[25] M. Arndt and K. Hornberger. Testing the limits of quantum mechanical superpositions. *Nat. Phys.*, 10:271–277, 2014.

[26] S. Gerlich, S. Eibenberger, M. Tomandl, S. Nimmrichter, K. Hornberger, P.J. Fagan, J. Tüxen, M. Mayor, and M. Arndt. Quantum interference of large organic molecules. *Nat. Commun.*, 2:263, 2011.

[27] W. Marshall, C. Simon, R. Penrose, and D. Bouwmeester. Towards quantum superpositions of a mirror. *Phys. Rev. Lett.*, 91:130401, 2003.

[28] Qwerty123uiop/CC-BY-SA-3.0. Schematic view of a photomultiplier coupled to a scintillator, illustrating detection of gamma rays. https://commons.wikimedia.org/wiki/File:PhotoMultiplierTubeAndScintillator.svg. Accessed: Dec. 17, 2018.

Chapter 2

Elements of microwave technology

2.1 Introduction

This thesis concerns the field of microwaves. Within the electromagnetic (EM) spectrum, microwaves are those waves for which the wavelength λ is approximately equal to the size of components used for transmission. Indeed, as microwaves have a frequency of 3 to 300 GHz [1], their typical wavelength is approximately $\lambda = c/f = 10\,\text{cm}$ to $1\,\text{mm}$, where c is the speed of light. Therefore, circuit analysis in terms of lumped elements fails as the phase of the voltage and current over the element cannot be approximated as constant. On the other hand, the methods of geometrical optics fail, which assume that the wavelength is much shorter than the size of a component. This implies that microwave circuits must be described in terms of distributed elements.
In this chapter we cover the basics of microwave technology relevant for this thesis. We review microwave transmission lines, microwave reflections, the coplanar waveguide (CPW) and microwave CPW resonators.

2.2 Microwave transmission line theory

In microwave engineering, transmission lines are generally modelled as distributed-element circuits as depicted in figure 2.1. In this figure $\mathcal{L}$, $\mathcal{R}$, $\mathcal{C}$ and $\mathcal{G}$ are the inductance, resistance, capacitance and conductance of the line per unit length. $\mathcal{L}$ and $\mathcal{R}$ arise due to the self-inductance and finite conductivity of the line, whereas $\mathcal{C}$ and $\mathcal{G}$ are due to the proximity of the centre conductor and the ground that might induce dielectric losses. Here, we follow [1].

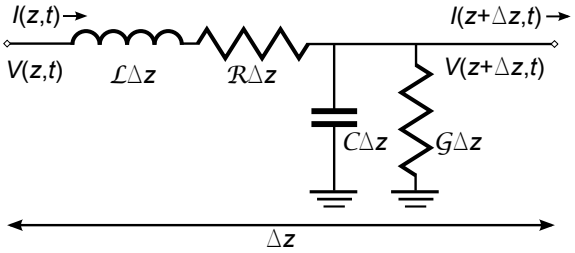


Figure 2.1: *Lumped-element circuit representation of an incremental length of a microwave transmission line.*

Applying Kirchhoff's law for voltage, V, to the circuit in figure 2.1 we find

$$V(z,t) - \mathcal{R}\Delta z I(z,t) - \mathcal{L}\Delta z \frac{\mathrm{d}I(z,t)}{\mathrm{d}t} - V(z+\Delta z,t) = 0. \tag{2.1}$$

where $I(z,t)$ is the current in the line.
Similarly, Kirchhoff's law for current gives

$$I(z,t) - \mathcal{G}\Delta z V(z+\Delta z,t) - \mathcal{C}\Delta z \frac{\mathrm{d}V(z+\Delta z,t)}{\mathrm{d}t} - I(z+\Delta z,t) = 0. \tag{2.2}$$

Taking the limit $\Delta z \to 0$ yields the so-called telegrapher's equations

$$\frac{\mathrm{d}V(z,t)}{\mathrm{d}z} = -\mathcal{R}I(z,t) - \mathcal{L}\frac{\mathrm{d}I(z,t)}{\mathrm{d}t}, \tag{2.3}$$

$$\frac{\mathrm{d}I(z,t)}{\mathrm{d}z} = -\mathcal{G}V(z,t) - \mathcal{C}\frac{\mathrm{d}V(z,t)}{\mathrm{d}t} \tag{2.4}$$

In case the propagating modes have an $\exp(-i\omega t)$-dependence on time, where ω is the angular frequency, equations (2.3) and (2.4) simplify to

$$\frac{\mathrm{d}V(z)}{\mathrm{d}z} = -(\mathcal{R} - i\omega\mathcal{L})I(z), \tag{2.5}$$

$$\frac{\mathrm{d}I(z)}{\mathrm{d}z} = -(\mathcal{G} - i\omega\mathcal{C})V(z) \tag{2.6}$$

from which the wave equations for voltage and current are easily derived as

$$\frac{\mathrm{d}^2V(z)}{\mathrm{d}z^2} = \gamma^2 V(z), \tag{2.7}$$

$$\frac{\mathrm{d}^2I(z)}{\mathrm{d}z^2} = \gamma^2 I(z). \tag{2.8}$$

Here, $\gamma \equiv ((\mathcal{R} - i\omega\mathcal{L})(\mathcal{G} - i\omega\mathcal{C}))^{1/2}$ is the wave's propagation constant. The wave number of the mode is given by $k = \mathrm{Im}(\gamma)$ and is related to the wavelength as $\lambda = 2\pi/k$. The mode's phase velocity is $v_{\mathrm{ph}} = \omega/k$ and its damping coefficient is given by $r = -\mathrm{Re}(\gamma)$.
Solving equations (2.7) and (2.8) yields

$$V = V_0^+ e^{\gamma z} + V_0^- e^{-\gamma z}, \tag{2.9}$$

$$I = I_0^+ e^{\gamma z} + I_0^- e^{-\gamma z},, \tag{2.10}$$

where the amplitudes $V_0^{+,-}$ and $I_0^{+,-}$ are determined by the boundary values of the transmission line. When inserting equation (2.9) into equation (2.5), we find

$$I = \frac{\gamma}{\mathcal{R} - i\omega\mathcal{L}}\left(V_0^+ e^{\gamma z} - V_0^- e^{-\gamma z}\right). \tag{2.11}$$

Comparing this result to equation (2.10) we are led, by Ohm's law, to the concept of a characteristic impedance. This quantity is conceptually the same as the index of refraction in optical systems. From the comparison, we find

$$Z_{\mathrm{c}} \equiv \sqrt{\frac{\mathcal{R} - i\omega\mathcal{L}}{\mathcal{G} - i\omega\mathcal{C}}} \tag{2.12}$$

allowing us to rewrite equations (2.10) and (2.11) as

$$I = \frac{V_0^+}{Z_{\mathrm{c}}} e^{\gamma z} - \frac{V_0^-}{Z_{\mathrm{c}}} e^{-\gamma z}. \tag{2.13}$$

In particular, if we have a lossless transmission line, $\mathcal{R}$ and $\mathcal{G}$ equal 0. This implies $Z_{\mathrm{c}} = \sqrt{\mathcal{L}/\mathcal{C}}$ and $k = \omega\sqrt{\mathcal{L}\mathcal{C}}$. The phase velocity equals $v_{\mathrm{ph}} = 1/\sqrt{\mathcal{L}\mathcal{C}}$.

2.3 Microwave reflection

Although generally one wants to avoid reflections in the system, in practise every component or transmission line will reflect some power. In the following, we will discuss two cases in which we can use these reflections to characterise a set-up.

2.3.1 Non-impedance matched, dispersion-less transmission lines

As mentioned, in microwave technology the characteristic impedance plays the role of the optical index of refraction. This implies that a sudden change in characteristic impedance will, analogously, cause partial wave reflection in the transmission line. In case a dispersionless transmission line is not impedance-matched to its environment, we can determine its characteristics from these reflections.
Suppose we have a change in characteristic impedance as sketched in figure 2.2. Then, if a wave traverses the line from region 1 to region 2, the transmission and reflection coefficients are given by [1]

$$\tau_{\vec{1}\to\vec{2}} = \frac{2Z_{c,2}}{Z_{c,1}+Z_{c,2}}, \tag{2.14}$$

$$\rho_{\vec{1}\to\vec{1}} = \frac{Z_{c,2}-Z_{c,1}}{Z_{c,1}+Z_{c,2}} \tag{2.15}$$

where the arrows over the regions indicate the direction of the incoming and outgoing wave.

Now consider the full network in figure 2.2. It consists of two leads with characteristic impedance $Z_{c,1}$, the characteristic impedance of the environment. In between the leads is a transmission line of unknown impedance $Z_{c,2}$ with a length l. Due to reflections on the $Z_{c,1}, Z_{c,2}$-boundaries this network will behave as a Fabry-Pérot interferometer showing typical peaks and troughs (wiggles) in its transmission as function of frequency.

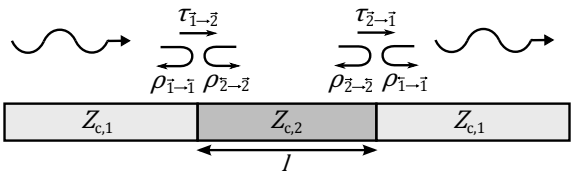


Figure 2.2: *An arbitrary transmission line with characteristic impedance $Z_{c,2}$ is coupled to an environment with impedance $Z_{c,1}$. From the wiggles in the transmission spectrum we can infer the inductance and capacitance per unit length of the transmission line.*

In case losses are small ($\omega\mathcal{L} \gg \mathcal{R}$ and $\omega\mathcal{C} \gg \mathcal{G}$) the inductance and capacitance per unit length, $\mathcal{L}_2$ and $\mathcal{C}_2$ respectively, can be estimated using three parameters

from the transmission spectrum. First one needs the period of the wiggles (the free spectral range), f_w, which is linked to the phase velocity of the wave propagating in the transmission line as

$$\frac{l}{\lambda} = \frac{l}{v_{\mathrm{ph},2}} f_\mathrm{w} = \frac{1}{2} \rightarrow v_{\mathrm{ph},2} = 2l f_\mathrm{w}. \tag{2.16}$$

Secondly the difference in transmission between the wiggle peaks and troughs is required

$$\Delta\tau \equiv \frac{|T|_\mathrm{max}}{|T|_\mathrm{min}} = 10^{\Delta T_{[\mathrm{dB(m)}]}/20}. \tag{2.17}$$

Here, $\Delta T_{[\mathrm{dB(m)}]}$ is the difference between the minimum and maximum of the wiggles in the frequency spectrum expressed in dB(m). Finally one needs the loss-coefficient r, which can be estimated from the spectrum as

$$r = \frac{-IL}{20l \log_{10} \mathrm{e}} \approx \frac{-\Delta T_\mathrm{p-b}}{20l \ {}^{10}\log \mathrm{e}} \tag{2.18}$$

with IL the insertion loss in dB, which is approximately equal to the difference in transmission between a transmission peak of the device and a by-pass line, $\Delta T_\mathrm{p-b}$. In fact, since the loss diminishes the amplitude of the wiggles, this approximation yields a slight overestimation of r, hence it is beneficial to estimate the loss and wiggle amplitude at a frequency (range), in which the losses are small. All these values can be obtained from the transmission spectrum.

The transmission spectrum of the Fabry-Pérot interferometer is well-known to be

$$T = \frac{\tau_{\vec{1}\vec{2}}\tau_{\vec{2}\vec{3}}\mathrm{e}^{(\mathrm{i}k-r)l}}{1-\rho_{\vec{2}\vec{2}}\rho_{\vec{2}\vec{2}}\mathrm{e}^{2(\mathrm{i}k-r)l}}, \tag{2.19}$$

omitting the arrows from equations (2.14) and (2.15). Taking the absolute value of this equation one arrives at

$$|T|^2 = \frac{\left|\tau_{\vec{1}\vec{2}}\right|^2 \left|\tau_{\vec{2}\vec{3}}\right|^2 e^{-2rl}}{1+\left|\rho_{\vec{2}\vec{2}}\right|^2 \left|\rho_{\vec{2}\vec{2}}\right|^2 e^{-4rl} - 2\rho_{\vec{2}\vec{2}}\rho_{\vec{2}\vec{2}}e^{-2rl}\cos(2kl)}. \tag{2.20}$$

Neglecting the $\mathcal{R}$- and $\mathcal{G}$-contributions to the characteristic impedance (equation (2.12)), $\tau_{\vec{n}\vec{m}} \in \mathbb{R}$ and $\rho = \pm\rho_{\vec{2}\vec{2}} = \pm\rho_{\vec{2}\vec{2}} \in \mathbb{R}$, where the $\pm$-signs arise as we do not know whether $Z_{\mathrm{c},1} > Z_{\mathrm{c},2}$ or $Z_{\mathrm{c},1} < Z_{\mathrm{c},2}$ one finds from equation (2.20)

$$\Delta\tau \equiv \frac{|T|_\mathrm{max}}{|T|_\mathrm{min}} = \frac{1+\rho^2 e^{-2rl}}{1-\rho^2 e^{-2rl}}. \tag{2.21}$$

Solving for ρ yields

$$\rho = e^{rl}\sqrt{\frac{\Delta\tau - 1}{\Delta\tau + 1}}. \tag{2.22}$$

Finally, from equation (2.15)

$$\rho = \pm \frac{Z_{c,2} - Z_{c,1}}{Z_{c,1} + Z_{c,2}} \tag{2.23}$$

and one can solve for the unknown impedance as

$$Z_{c,2} = \frac{\mp 1 - \rho}{\rho \mp 1} Z_{c,1}. \tag{2.24}$$

To obtain $\mathcal{L}_2$ and $\mathcal{C}_2$ one can apply

$$Z_{c,2} = \sqrt{\frac{\mathcal{L}_2}{\mathcal{C}_2}}, \quad v_{ph,2} = \frac{1}{\sqrt{\mathcal{L}_2 \mathcal{C}_2}} \tag{2.25}$$

which holds for lossless networks. Whence

$$\mathcal{L}_2 = \frac{Z_{c,2}}{v_{ph,2}}, \mathcal{C}_2 = \frac{1}{Z_{c,2} v_{ph,2}}, \tag{2.26}$$

or, taking the results from equations (2.16), (2.22) and (2.24) together

$$\mathcal{L}_2 = \frac{-Z_{c,1}}{2 l f_w} \frac{e^{rl}\sqrt{(\Delta\tau - 1)/(\Delta\tau + 1)} \pm 1}{e^{rl}\sqrt{(\Delta\tau - 1)/(\Delta\tau + 1)} \mp 1} \tag{2.27}$$

$$\mathcal{C}_2 = \frac{-1}{2 Z_{c,1} l f_w} \frac{e^{rl}\sqrt{(\Delta\tau - 1)/(\Delta\tau + 1)} \mp 1}{e^{rl}\sqrt{(\Delta\tau - 1)/(\Delta\tau + 1)} \pm 1} \tag{2.28}$$

It should be noted that this calculation always yields two separate values for $\mathcal{L}_2$ and $\mathcal{C}_2$, corresponding to the high-impedance and low-impedance solution to the problem. If the line is really mismatched, it is possible to rule out one of the solutions on physical grounds. However, if the line impedance is close to the impedance of the environment, this is no longer possible.

As an example, consider the (theoretical) case in which we put a 80 Ω-line with a length of 10 cm in a 50 Ω-environment. Within the line the phase velocity equals 1×10^8 m/s and the line has a frequency-dependent loss coefficient $r = 0.2 f/[\mathrm{GHz}]\mathrm{m}^{-1}$. If we were given such a line and only know its length, we can use the theory presented in this section to estimate the line parameters using a measured frequency spectrum. The frequency spectrum as obtained from equation (2.19) is depicted in figure 2.3. From this figure, we estimate $f_w \approx 500$ MHz and $\Delta T_{[\mathrm{dB}]} = 0.790$ dB and $IL \approx 0.86$ dB at $f = 4.5$ GHz (the first transmission peak). This yields, using equations (2.18), (2.17), (2.27) and (2.28), $r = 0.99\,\mathrm{m}^{-1}$ (input $0.90\,\mathrm{m}^{-1}$), $\mathcal{L}_2 = 0.808$ or $0.309\,\mu$H/m and correspondingly $\mathcal{C}_2 = 124$ or 232 pF/m. From the obtained $\mathcal{L}$s and $\mathcal{C}$s we estimate $Z_{c,2} = 80.8$ or $30.9\,\Omega$ and $v_{ph} = 1 \times 10^8$ m/s.
From our initial input we know that we would have to choose the first solution, which is indeed close to $Z_{c,2} = 80\,\Omega$. However, in practice we should make a decision based on the design of our device as this will constrain $\mathcal{L}$ and $\mathcal{C}$.

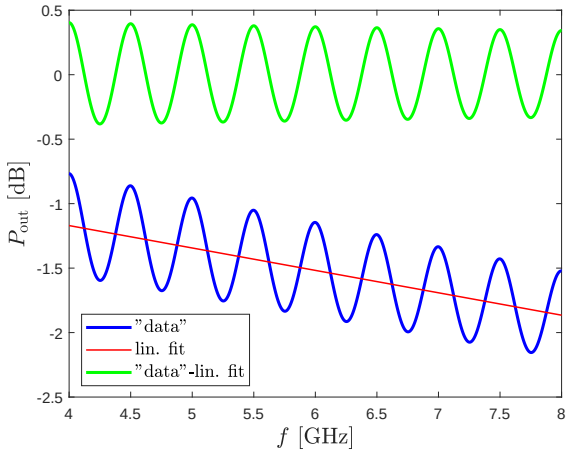


Figure 2.3: *Theoretical frequency spectrum of a* 10 cm*-long,* 80 Ω*-transmission line. To obtain estimations of the necessarry parameters for estimating the line characteristics of this transmission line, we can make a linear fit of the spectrum and subtract it from the data.*

2.3.2 Reflection planes

Each connection in a microwave set-up reflects some power creating reflection planes. If one is interested from what part of the set-up reflections arise the following method can be used. First the transmission needs to be measured as a function of frequency. Although this spectrum might seem flat, each pair of reflection planes will, as in the last section, create a Fabry-Pérot cavity. From the specifications of the different components, we know the characteristic impedance (usually 50 Ω) and the phase velocity (usually $2c/3$, where c is the speed of light). In order to find the periodicity of the Fabry-Pérot interference pattern, one takes the Fourier transform of the appropriately windowed spectrum. This yields f_{w} as in last section, from which we can easily obtain the line length between the reflection planes as

$$l_{\text{culp}} = \frac{v_{\text{ph}}}{2f_{\text{w}}} \tag{2.29}$$

where "culp" refers to the culprits of the reflection.
Due to the scalloping loss of the window function and the loss in the transmission line(s) connecting the culprits, the wiggle amplitude resulting from the Fourier transform does not correspond to the actual wiggle amplitude. Therefore, this method does not provide a means to estimate the reflection coefficients of the reflection planes. Moreover, care should be taken that the calibration of the measurement apparatus is off during the measurement, as this will yield spurious results. An example is depicted in figure 2.4, where we have placed a NbTiN-transmission line of 15 cm in between two 1.5 m-long VNA cables using

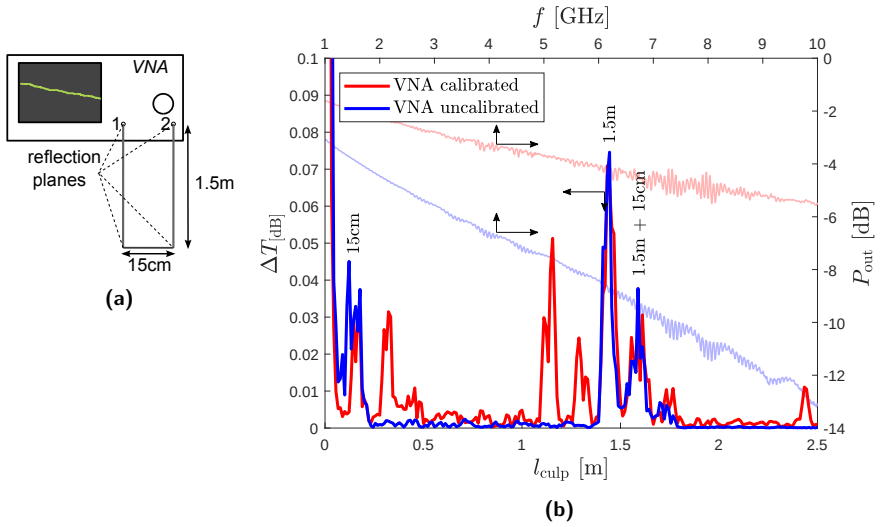


Figure 2.4: *Reflection planes in a* 50 Ω*-set-up. (a) A* 15 cm*-long NbTiN-transmission line was put in between two* 1.5 m*-long Vector Network Analyser (VNA) cables. (b) Although the frequency spectrum is flat (light red/blue, axes top/right), we still find reflections from the line transitions in the Fourier transform of the spectrum (red/blue, axes bottom/left). The calibration of the VNA produces spurious reflections (red).*

female-female adapters. In the Fourier transform resulting from the frequency spectrum we can discern a peak at 15 cm, 1.5 m and 1.65 m corresponding to the line lengths in the set-up.

2.4 Coplanar waveguides

As a basic structure for the travelling-wave parametric amplifier (TWPA) discussed in chapter 5, we will use a superconducting coplanar waveguide (CPW), which is schematically depicted in figure 2.5. These transmission lines support quasi-transverse electromagnetic (TEM) modes. Their relevant characteristics are discussed in, among others, [2] and references therein, which we will review shortly.

Assuming the CPW has a low loss, the impedance is well-described by $Z_\mathrm{c} = \sqrt{\mathcal{L}/\mathcal{C}}$. In ordinary CPWs, the inductance has a geometric and a kinetic contribution summing to the total inductance. The geometric inductance is given by

$$\mathcal{L}_\mathrm{g} = \frac{\mu_0}{4}\frac{E\left(\tilde{w}\right)}{E\left(\tilde{w}'\right)}, \tag{2.30}$$

where μ_0 is the permeability of free space and E is the elliptic function of the first kind with arguments $\tilde{w} = w_\mathrm{c}/\left(w_\mathrm{c} + 2w_\mathrm{g}\right)$ and $\tilde{w}' = \sqrt{1-\tilde{w}^2}$. w_c is the width

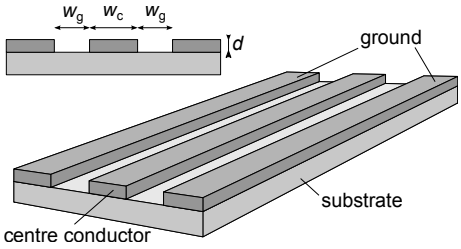


Figure 2.5: *Schematic representation of a coplanar waveguide. The CPW consists of a centre conductor in between two conducting ground planes on an isolating substrate. It supports quasi-TEM modes of EM-radiation.*

of the CPWs centre conductor and w_g is the width of the gaps, see figure 2.5. This holds as long as the material around the CPW has a relative permeability $\mu_r \approx 1$. The kinetic contribution, due to the inertia of the Cooper pairs carrying the modes through the transmission line, is found from multiplying the sheet inductance

$$L_S = \mu_0 \lambda \coth\left(\frac{d}{\lambda_m}\right) \tag{2.31}$$

with a geometric factor g with unit m^{-1}. Here, d is the thickness of the material. $\lambda_m = \sqrt{\hbar\sigma/\pi\mu_0\Delta_{sc}(0)}$ is the magnetic penetration depth, where σ is the material's normal state sheet resistivity and $\Delta_{sc}(0) = 1.76 k_B T_c$ is the superconducting gap energy, assuming $T \ll T_c$. The geometric factor contains two terms, one due to the contribution of the centre conductor and the other due to the contribution of the ground planes to the kinetic inductance. These contributions are given by

$$g_c = \frac{1}{4w_c\tilde{w}'^2 E^2(\tilde{w})}\left(\pi + \ln\left(\frac{4\pi w_c}{d}\right) - \tilde{w}\ln\left(\frac{1+\tilde{w}}{1-\tilde{w}}\right)\right), \tag{2.32}$$

$$g_g = \frac{\tilde{w}}{4w_c\tilde{w}'^2 E^2(\tilde{w})}\left(\pi + \ln\left(\frac{4\pi\,(w_c + 2w_g)}{d}\right) - \frac{1}{\tilde{w}}\ln\left(\frac{1+\tilde{w}}{1-\tilde{w}}\right)\right), \tag{2.33}$$

yielding a kinetic inductance of

$$\mathcal{L}_k = (g_c + g_g)\, L_S \tag{2.34}$$

which is accurate to within 10% for $d < 0.05 w_c$ and $\tilde{w} < 0.8$. This yields a total inductance of $\mathcal{L} = \mathcal{L}_g + \mathcal{L}_k$.

The capacitance of the CPW is given by

$$\mathcal{C}_g = 4\epsilon_0\epsilon_{eff}\frac{E\,(\tilde{w}')}{E\,(\tilde{w})} \tag{2.35}$$

where ϵ_0 is the vacuum permittivity and ϵ_{eff} is the effective relative permittivity of the CPW given by the average relative permittivity of the material below

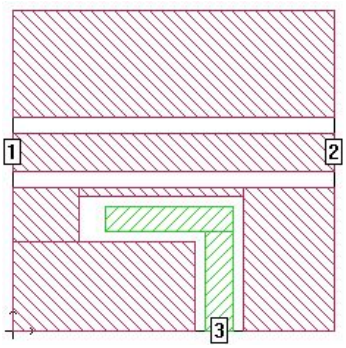


Figure 2.6: Sonnet-*implementation for calculating the resonator coupling. The resonator (in green) is coupled to a feedline (in purple) between ports* 1 *and* 2*. In order to calculate the coupling strength we need the magnitude of the scattering parameter* S_{13} *at the resonator's frequency.*

and on top of the conducting material. In case one of these is vacuum, $\epsilon_{\text{eff}} = (1 + \epsilon_{\text{r}})/2$, where ϵ_{r} is the relative permittivity of the substrate.

For a CPW that has a centre conductor width of $12\,\mu$m, gaps of $5\,\mu$m, made out of 200 nm-thick NbTiN ($T_{\text{c}} = 15.1\,\text{K}$, $\sigma = 1.06\,\mu\Omega\text{m}$) on a silicon substrate ($\epsilon_{\text{r}} = 11.45$) at mK-temperatures, $\mathcal{L} = 470\,\text{nH/m}$ and $\mathcal{C} = 177\,\text{pF/m}$ indeed yielding $Z_{\text{c}} \approx 50\,\Omega$.

2.5 Microwave resonators (CPW)

To obtain a high-gain, large-bandwidth TWPA, some form of dispersion engineering is necessary in order to reach the phase-matching condition. Therefore, as a last section of this chapter, we will review CPW microwave resonators that can be used for this purpose. Here we follow [2, 3] and references therein.

CPW resonators come in two types. Either both ends are open or closed, in which case we have a $\lambda/2$-resonator or one of the ends is closed yielding a $\lambda/4$-resonator. The advantage of the latter is that they are shorter than $\lambda/2$-resonators The resonant frequencies of such resonators are given by

$$f^0_{\text{r},n} = \frac{m}{n l_{\text{r}} \sqrt{\mathcal{L}_{\text{r}} \mathcal{C}_{\text{r}}}}. \tag{2.36}$$

Here, n determines the resonator type, $n = 2$ for a $\lambda/2$-resonator and $n = 4$ for a $\lambda/4$-resonator. m is the order of the resonance. For $\lambda/2$-resonators, $m \in \{1, 2, 3, 4, ...\}$ and for $\lambda/4$-resonators $m \in \{1, 3, 5, 7, ...\}$.
Upon coupling a resonator to a transmission line the resonator is loaded and as

a result the resonance frequency shifts. This shift is given by

$$\delta f_{\mathrm{r},n} = -\sqrt{\frac{2}{\pi Q_{\mathrm{c}}}} f^0_{\mathrm{r},n} \tag{2.37}$$

such that the resonance frequency of a loaded resonator is $f^l_{\mathrm{r},n} = f^0_{\mathrm{r},n} + \delta f_{\mathrm{r},n}$. In equation (2.37), Q_{c} is the coupling quality factor, which depends mainly on the magnitude of the coupling capacitance and the frequency. It can be determined as

$$Q_{\mathrm{c}} = \frac{2\pi n}{m\left|S_{13}\right|^2} \tag{2.38}$$

where S_{13} is the scattering parameter from port 3 to port 1 at $f = f^0_{\mathrm{r},n}$, see figure 2.6. It can be obtained from Sonnet-simulations.

The width of the resonance, Δf^l_{r}, is determined by the loaded quality factor, which can be calculated from

$$\frac{1}{Q_{\mathrm{l}}} = \frac{\Delta f^l_{\mathrm{r}}}{f^l_{\mathrm{r}}} = \frac{1}{Q_{\mathrm{c}}} + \frac{1}{Q_{\mathrm{i}}}. \tag{2.39}$$

Here, Q_{i} is the internal quality factor of the resonator, which can be calculated as $Q_{\mathrm{i}} = k/2r$.

References

[1] D.M. Pozar. *Microwave engineering.* Wiley, 4th edition, 2012.

[2] R. Barends. *Photon-detecting superconducting resonators.* PhD thesis, Delft university of technology, 2009.

[3] P.C.J.J. Coumou. *Electrodynamics of strongly disordered superconductors.* PhD thesis, Delft university of technology, 2015.

Chapter 3

A mesoscopic Hamiltonian for Josephson travelling-wave parametric amplifiers

We present a theory describing parametric amplification in a Josephson junction embedded transmission line. We will focus on the process of four-wave mixing under the assumption of an undepleted pump. However, the approach taken is quite general, such that a different parametric process or the process under different assumptions is easily derived. First the classical theory of the coupled-mode equations as presented by O'Brien *et al.* [*Phys. Rev. Lett.* **113** : 157001] is shortly reviewed. Then a derivation of the full quantum theory is given using mesoscopic quantisation techniques in terms of discrete mode operators. This results in a Hamiltonian that describes the process of parametric amplification. We show that the coupled-mode equations can be derived from this Hamiltonian in the classical limit and elaborate on the validity of the theory.

This chapter has been submitted for publication.

3.1 Introduction

Parametric amplification arises as a result of non-linear optics. In case a non-linear medium is traversed by a (weak) signal and a strong pump, a wave-mixing interaction causes the signal to be amplified. The main advantage of such amplifiers is their low added noise. In comparison: a conventional low-noise microwave amplifier has a noise temperature T_n of several Kelvins, which translates into $k_\mathrm{B}T_\mathrm{n}/\hbar\omega \approx 10$ photons of added noise for $T_\mathrm{n} = 2\,\mathrm{K}$ at a frequency of $\omega/2\pi = 4\,\mathrm{GHz}$ [1–3]. This number can be reduced to 1/2 or even 0 in a parametric amplifier, depending on its configuration [4]. This makes parametric amplifiers ideal to amplify signals that are on single-photon level.
In the past decade, many microwave parametric amplifiers have been developed to read out quantum bits in quantum information experiments (see e.g. [5] for a review). In most of the designs [6–10] the amplifier is embedded in a resonator to increase the interaction time of pump and signal, thus to increase the amplifier's gain. Due to such a design these amplifiers, however, are inherently limited in their bandwidth, giving rise to scalability issues now that the number of quantum bits in a single experiment increases. For this reason travelling-wave parametric amplifiers (TWPAs) have been developed [11–16]. As these are not based on resonance, they do not suffer from the intrinsic bandwidth limitation. However, to achieve a large gain the amplifiers need to be long.
Currently, two sources of non-linearity have been considered for TWPAs. Firstly, one can base the amplifier design on the intrinsic non-linear kinetic inductance of superconductors [11, 14–16]. Secondly, one can embed Josephson junctions in the transmission line, which have a non-linear inductance [12, 13]. Both versions of the TWPA have been described theoretically using classical coupled-mode equations [11, 12, 17, 18]. However, a Hamiltonian-description is necessary to describe the TWPA as a quantum device, which is needed for a recently proposed experiment testing the limits of quantum mechanics by entangling two TWPAs within a single-photon interferometer [19]. Some authors consider such a description impossible due to difficulties of quantum mechanics in describing dispersion [20] (and references therein) – an important characteristic in TWPAs. However, in case of a TWPA based on Josephson junctions such a description appears to be possible. The Josephson TWPA has already been described using a Hamiltonian based on continuous mode operators [21]. This description was used to calculate average gain and squeezing effects. In this work we use discrete mode operators for our analysis and use the resulting Hamiltonian to calculate photon number distributions, apart from gain effects.

We will first put the concept of parametric amplification on solid ground by introducing the necessary terminology. Then, a review is given of O'Brien *et al.* [18] where the coupled-mode equations were derived, which can be used for predicting the classical response of a Josephson TWPA in case the non-linearity in the transmission line is weak. In section 3.4 we proceed in deriving the Hamiltonian of the Josephson junction embedded transmission line in the limit

of a weak non-linearity, which we apply to the specific case of a non-degenerate parametric amplifier with undepleted degenerate pump in section 3.5. In this section we will also discuss other implementations of the Hamiltonian shortly. Then we will derive the classical coupled-mode equations once more, but now from the quantum Hamiltonian. Thus we show that the classical and quantum theories converge in the classical limit. The chapter is concluded by a discussion of the validity of the theories in terms of the strength of the non-linearity, i.e. to which value of the non-linearity it can be considered weak, in section 3.8.

3.2 Terminology

For parametric amplifiers a specific terminology is used that can be confusing at times. Here an overview of the terminology is presented and it is discussed under which circumstances the terms play a role. These circumstances are fully determined by the Hamiltonian that describes the process.
Basically, parametric amplifiers work by the principle of wave mixing. This mixing process occurs due to a non-linear response of the device to a transmitting electromagnetic field and causes energy transfer between the different transmitting modes. Suppose that the non-linearity occurs as a result of a non-linear polarisation of the material,

$$\mathbf{P} = \left(\chi_{\mathrm{e}}^{(1)} + \chi_{\mathrm{e}}^{(2)}\mathbf{E} + \chi_{\mathrm{e}}^{(3)}\mathbf{E}^2 + \dots\right)\mathbf{E}, \tag{3.1}$$

then the Hamiltonian contains a term

$$H_{\mathrm{EP}} \propto \mathbf{E}\cdot\mathbf{P} = \chi_{\mathrm{e}}^{(1)}\mathbf{E}^2 + \chi_{\mathrm{e}}^{(2)}\mathbf{E}^3 + \chi_{\mathrm{e}}^{(3)}\mathbf{E}^4 + \dots. \tag{3.2}$$

In case the material has a strong $\chi_{\mathrm{e}}^{(2)}$-contribution, the $\mathbf{E}^3$-term in the Hamiltonian leads to a three-wave mixing process (3WM) and consequently to a mixing term in the Hamiltonian of the form

$$\hat{H}_{\mathrm{3WM}} = \hbar\chi\hat{a}_{\mathrm{p}}\hat{a}_{\mathrm{s}}^{\dagger}\hat{a}_{\mathrm{i}}^{\dagger}\mathrm{e}^{i(-\Delta\Omega t+\Delta\phi)} + \mathrm{H.c.}. \tag{3.3}$$

This Hamiltonian enables a photon in the pump mode (p) to be scattered into a photon in the signal mode (s) that is to be amplified and some rest energy, which is generally referred to as the idler mode (i). As the Hamiltonian conserves energy, $\omega_{\mathrm{i}} = \omega_{\mathrm{p}} - \omega_{\mathrm{s}}$. Here, $\Delta\Omega$ is a phase mismatching term resulting from dispersion and modulation in the device, to be discussed in section 3.3 (equation (3.16)) and section 3.6 (equations (3.79) and (3.81)). $\Delta\phi = \phi_{\mathrm{p}} - \phi_{\mathrm{s}} - \phi_{\mathrm{i}}$ is the phase difference between the pump, signal and idler that enter the device.
Contrarily, if the material has a dominant $\chi_{\mathrm{e}}^{(3)}$-contribution, the Hamiltonian contains a term

$$\hat{H}_{\mathrm{4WM}} = \hbar\chi\hat{a}_{\mathrm{p}}\hat{a}_{\mathrm{p'}}\hat{a}_{\mathrm{s}}^{\dagger}\hat{a}_{\mathrm{i}}^{\dagger}\mathrm{e}^{i(-\Delta\Omega t+\Delta\phi)} + \mathrm{H.c.} \tag{3.4}$$

and a four-wave mixing (4WM) process takes place, where $\Delta\phi = \phi_{\mathrm{p}}+\phi_{\mathrm{p'}}-\phi_{\mathrm{s}}-\phi_{\mathrm{i}}$. In this case two pump photons are scattered into a signal and an idler photon

and $\omega_\mathrm{i} = \omega_\mathrm{p} + \omega_\mathrm{p'} - \omega_\mathrm{s}$. In case $\hat{a}_\mathrm{p} \neq \hat{a}_\mathrm{p'}$ the pump is said to be non-degenerate, whereas it is degenerate if $\hat{a}_\mathrm{p} = \hat{a}_\mathrm{p'}$.
Generally, the pump(s) in equations (3.3) and (3.4) are treated as classical modes, which are undepleted. This implies that the corresponding operators are replaced by a constant amplitude and can be absorbed in the coupling constant. This results in a contribution to the Hamiltonian that is identical for 3WM and 4WM

$$\hat{H}_{3/4\mathrm{WM}} = \hbar\tilde{\chi}\hat{a}_\mathrm{s}^\dagger\hat{a}_\mathrm{i}^\dagger \mathrm{e}^{i(-\Delta\Omega t + \Delta\phi)} + \mathrm{H.c.} \tag{3.5}$$

in which $\tilde{\chi} = \chi\,|A_\mathrm{p}|$ for 3WM and $\tilde{\chi} = \chi\,|A_\mathrm{p}|\,|A_\mathrm{p'}|$ for 4WM respectively.

Apart from a distinction in 3WM- and 4WM-devices, parametric amplifiers can be phase-preserving and phase-sensitive. Phase-preserving amplification occurs if the signal and idler are in two distinct modes ($\hat{a}_\mathrm{s} \neq \hat{a}_\mathrm{i}$ as in equations (3.3) and (3.4)). For this reason such amplifiers are also referred to as non-degenerate. The amplification is independent of $\Delta\phi$ and a minimum of half a photon of noise per unit bandwidth is added to the signal [4]. The process is illustrated in figure 3.1.

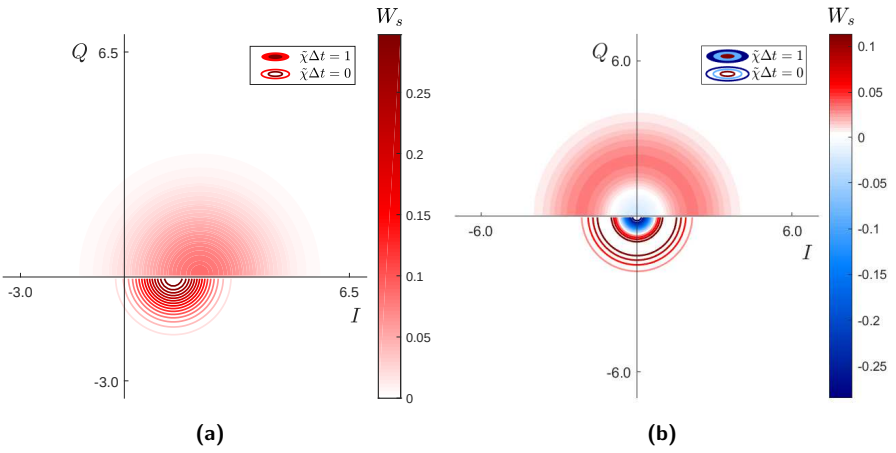


Figure 3.1: *Effect of non-degenerate (or phase-preserving) amplification with an undepleted, degenerate pump on (a) a coherent state ($\alpha = 1$) and (b) a single photon number state in the I, Q-quadrature plane. The lower half plane depicts (half of the) Wigner function of the unamplified state using contours, whereas the upper half plane shows the Wigner function of the state after amplification with filled contours. The increased width of the latter indicates the increase of noise in the amplified state. The Wigner functions are calculated using* Qutip *[22].*

If signal and idler are in non-distinct modes ($\hat{a}_\mathrm{s} = \hat{a}_\mathrm{i}$ in equations (3.3) and (3.4)), however, the amplifier is said to be degenerate and works in a phase-sensitive mode. The latter term results from a critical dependence of the amplification

process on $\Delta\phi$, which causes one quadrature of the signal to be amplified, whereas the other is de-amplified, see figure 3.2. This implies that for input signal states with an explicit phase, such as coherent states, the amplifier's power gain depends on the phase difference between signal and pump. The gain is maximised for $\Delta\phi = \pi/2$, whereas for $\Delta\phi = 3\pi/2$ the gain is less than unity, thus attenuating the signal. For input states that do not have such an explicit phase, e.g. number states and thermal states, the amplifier power gain is phase independent. In this process, amplification is possible without adding noise to the signal [4].

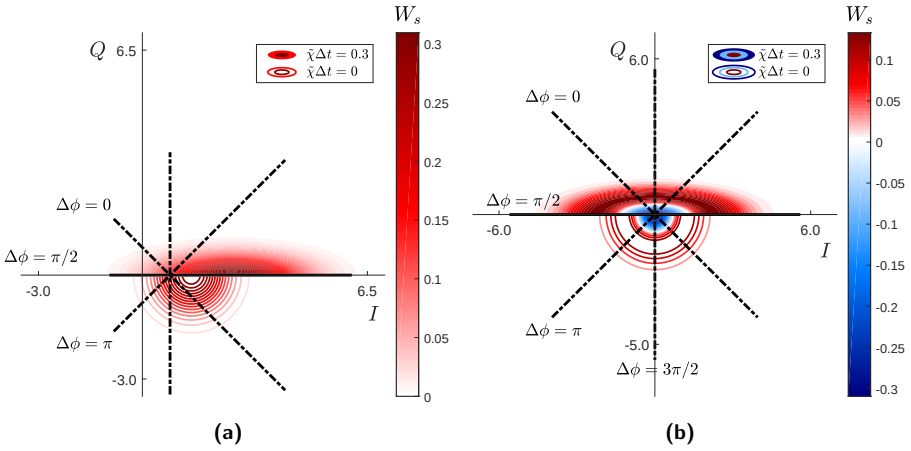


Figure 3.2: *Effect of degenerate (or phase-sensitive) amplification with an undepleted pump on (a) a coherent state ($\alpha = 1$) and (b) a single photon number state in the I, Q-quadrature plane. In the lower half plane (half of the) the Wigner functions of the unamplified states are depicted using contours. The upper half plane depicts the Wigner functions of the amplified states for $\Delta\phi = \pi/2$ with filled contours, whereas the long symmetry axis of the Wigner functions for some different $\Delta\phi$s are indictated by dashed lines. One quadrature is amplified, whereas the other is de-amplified, such that the added noise is 0. If the input state is a coherent state, the power gain varies with $\Delta\phi$. The Wigner functions are calculated using* Qutip *[22].*

In both 3WM- and 4WM-devices the amplification process is most efficient if the phase mismatch $\Delta\Omega = 0$, as is illustrated in figure 3.3. A non-zero $\Delta\Omega$ arises from dispersion and modulation effects, which are therefore beneficial to be cancelled.

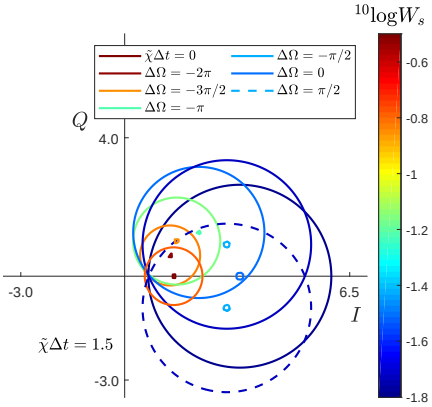


Figure 3.3: *Effect of phase mismatch on the phase-preserving amplification of a coherent state for an undepleted pump. Depicted are the full-width-half-maximum and the maximum of the Wigner function of the initial state $\tilde{\chi}\Delta t = 0$ and the final states $\tilde{\chi}\Delta t = 1.5$ with various amounts of phase mismatch $\Delta\Omega$ ($\Delta t = 1$) in the I, Q-quadrature plane. The legend refers to the maximum of the Wigner functions. Increasing the phase mismatch reduces the power gain of the amplifier. The Wigner functions are calculated using* Qutip *[22].*

3.3 The non-degenerate parametric amplifier with undepleted degenerate pump – classical theory

The classical theory for Josephson junction embedded transmission lines is worked out in detail in [17, 18]. In [17] such a line, as schematically depicted in figure 3.4, is considered and as a result a non-linear wave equation

$$C_{\mathrm{g}}\frac{\partial^2\Phi}{\partial t^2} - \frac{a^2}{L_{\mathrm{J},0}}\frac{\partial^2\Phi}{\partial z^2} - C_{\mathrm{J}}a^2\frac{\partial^4\Phi}{\partial z^2\partial t^2} = -\frac{a^4}{2I_{\mathrm{c}}^2L_{\mathrm{J},0}^3}\frac{\partial^2\Phi}{\partial z^2}\left(\frac{\partial\Phi}{\partial z}\right)^2 \tag{3.6}$$

is derived that describes the evolution of the flux $\Phi = \Phi(z,t)$ through the line. Here C_{g} is the capacitance to ground, a the length of a unit cell of the transmission line, $L_{\mathrm{J},0}$ is the Josephson inductance of the junctions at 0-flux, C_{J} is the capacitance of the Josephson junction and I_{c} its critical current. $L_{\mathrm{J},0}$ and I_{c} are related by $L_{\mathrm{J},0} = \varphi_0/I_{\mathrm{c}}$ with $\varphi_0 = \hbar/2e$ the reduced magnetic flux quantum, see section 3.4.4. In deriving this equation it is assumed that $a \ll \lambda$, the wavelength of the propagating modes, and that the non-linearity provided by the Josephson junctions is weak, such that only the first order non-linear term (right hand side of equation (3.6)) resulting from the presence of the Josephson junction needs to be taken into account.

Starting from this equation, [18] derives the coupled-mode equations. This is a set of coupled non-linear differential equations that describe the evolution

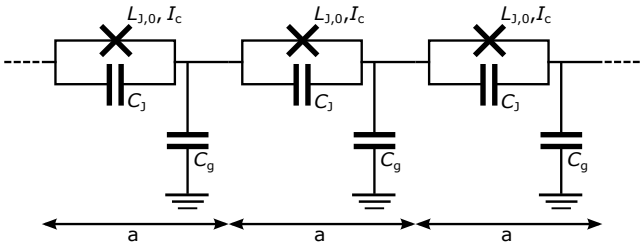


Figure 3.4: *Schematic overview of a Josephson junction embedded transmission line. The junctions are modelled as a parallel LC-circuit with a non-linear inductor L_J.*

of the considered modes of the flux through the parametric amplifier. For the non-degenerate 4WM parametric amplifier with degenerate pump it is assumed that only three modes of the field play a role. These are generally referred to as the pump, the signal and the idler. The pump is the mode that delivers the energy for the amplification of the small amplitude signal. As a result of energy conservation, an idler mode is created which also has a small amplitude.
[18] suggests a trial solution for equation (3.6) in the form of

$$\Phi = \sum_{n=\mathrm{p,s,i}} \mathrm{Re}\left\{A_n\left(z\right)\mathrm{e}^{i(k_n z-\omega_n t)}\right\} = \frac{1}{2}\sum_n A_n\left(z\right)\mathrm{e}^{i(k_n z-\omega_n t)} + c.c. \quad (3.7)$$

which describes a superposition of waves that may have varying amplitudes A_n while propagating through the line.
Furthermore, the slowly varying amplitude approximation is invoked, i.e., it is assumed that $\left|\mathrm{d}^2A_n/\mathrm{d}z^2\right| \ll |k_n \mathrm{d}A_n/\mathrm{d}z|$, and that the change in amplitude within a wavelength of transmission line is small, $|\mathrm{d}A_n/\mathrm{d}z| \ll |k_n A_n|$, such that the first order derivatives at the right hand side of equation (3.6) can be neglected. Furthermore, terms of order $|A_\mathrm{s}|^2$ and $|A_\mathrm{i}|^2$ are neglected, as these are assumed to be small. Then, the amplitudes of the various modes are described by the following differential equations, upon substituting the trial solution into equation (3.6),

$$\frac{\partial A_\mathrm{p}}{\partial z} = i\Xi_\mathrm{p}\left|A_\mathrm{p}\right|^2 A_\mathrm{p} + 2iX_\mathrm{p}A_\mathrm{p}^* A_\mathrm{s}A_\mathrm{i}\mathrm{e}^{i\Delta kz} \quad (3.8)$$

$$\frac{\partial A_\mathrm{s(i)}}{\partial z} = i\Xi_\mathrm{s(i)}\left|A_\mathrm{p}\right|^2 A_\mathrm{s(i)} + iX_\mathrm{s(i)}A_\mathrm{p}^2 A_\mathrm{i(s)}^*\mathrm{e}^{i\Delta kz} \quad (3.9)$$

where $\Delta k = 2k_\mathrm{p} - k_\mathrm{s} - k_\mathrm{i}$ and[1]

$$k_n = \frac{\omega_n\sqrt{L_{\mathrm{J},0}C_\mathrm{g}}}{a\sqrt{1-L_{\mathrm{J},0}C_\mathrm{J}\omega_n^2}}. \quad (3.10)$$

[1]Note that this is just the familiar form of k_n, $k_n = \omega_n\sqrt{LC}/a$, where $L \mapsto L/\left(1-LC_{/\!/L}\omega^2\right)$ as a result of the impedance $Z_\mathrm{J} = Z_{L_\mathrm{J}} /\!/ Z_{C_\mathrm{J}}$.

The coupling constants Ξ_n and X_n follow to be

$$\Xi_n = \frac{a^4 k_\mathrm{p}^2 k_n^3 \left(2 - \delta_{\mathrm{p}n}\right)}{16 C_\mathrm{g} I_c^2 L_{\mathrm{J},0}^3 \omega_n^2} \tag{3.11}$$

$$X_n = \frac{a^4 k_\mathrm{p}^2 k_\mathrm{s} k_\mathrm{i} \left(k_n - \varepsilon_n \Delta k\right)}{16 C_\mathrm{g} I_c^2 L_{\mathrm{J},0}^3 \omega_n^2} \tag{3.12}$$

with $\varepsilon_\mathrm{p} = 1$ and $\varepsilon_{\mathrm{s,i}} = -1$. As can be noted, the Ξ_ns modulate the wave number of the modes in case the pump amplitude is large. Ξ_p is therefore referred to as the self-modulation of the pump, while $\Xi_{\mathrm{s,i}}$ are the cross-modulation terms between the pump and the signal or idler.
Under the undepleted-pump approximation and assuming $A_{\mathrm{s,i}} \ll A_\mathrm{p}$, we can drop the interaction term in equation (3.8) and treat $|A_\mathrm{p}|^2$ as a constant. As a result, the equation can be solved analytically as

$$A_\mathrm{p} = |A_{\mathrm{p},0}|\, \mathrm{e}^{i\left(\Xi_\mathrm{p} |A_{\mathrm{p},0}|^2 z + \phi_\mathrm{p}\right)}. \tag{3.13}$$

Since we describe 4WM, which is phase preserving, we can assume $\phi_\mathrm{p} = 0$ with no loss of generality.

Substituting this result into equation (3.9), it can be rewritten as

$$\frac{\partial A_{\mathrm{s(i)}}}{\partial z} = i\Xi_{\mathrm{s(i)}} \left|A_{\mathrm{p},0}\right|^2 A_{\mathrm{s(i)}} + iX_{\mathrm{s(i)}} \left|A_{\mathrm{p},0}\right|^2 A_{\mathrm{i(s)}}^* \mathrm{e}^{i\left(\Delta k + 2\Xi_\mathrm{p} |A_{\mathrm{p},0}|^2\right) z} \tag{3.14}$$

Furthermore, switching to a co-rotating frame such that $A_{\mathrm{s(i)}} \mapsto A_{\mathrm{s(i)}} e^{i\Xi_{\mathrm{s(i)}} |A_{\mathrm{p},0}|^2 z}$, we can cast the equation in the form

$$\frac{\partial A_{\mathrm{s(i)}}}{\partial z} = iX_{\mathrm{s(i)}} \left|A_{\mathrm{p},0}\right|^2 A_{\mathrm{i(s)}}^* \mathrm{e}^{i\left(\Delta k + \Delta\Xi |A_{\mathrm{p},0}|^2\right) z} \tag{3.15}$$

where $\Delta\Xi = 2\Xi_\mathrm{p} - \Xi_\mathrm{s} - \Xi_\mathrm{i}$. This set of coupled differential equations can be solved analytically as [23]

$$\begin{aligned} A_{\mathrm{s(i)}} = \Bigg[& A_{\mathrm{(s,i)},0} \left(\cosh g_\mathrm{z} z - \frac{i\Delta K}{2 g_\mathrm{z}} \sinh g_\mathrm{z} z \right) + \\ & + \frac{i X_{\mathrm{s(i)}} \left|A_{\mathrm{p},0}\right|^2}{g_\mathrm{z}} A_{\mathrm{i(s)},0}^* \sinh g_\mathrm{z} z \Bigg] \mathrm{e}^{i\Delta K z/2} \end{aligned} \tag{3.16}$$

with $\Delta K = \left(\Delta k + \Delta\Xi |A_{\mathrm{p},0}|^2\right)$, which is related to $\Delta\Omega$ in equation (3.4) through $k_n + \Xi_n |A_{\mathrm{p},0}|^2 \mapsto (k_n + \Xi_n)\omega_n |A_{\mathrm{p},0}|^2 / k_n$, see section 3.7. $g_\mathrm{z} = \sqrt{X_\mathrm{s} X_\mathrm{i}^* |A_{\mathrm{p},0}|^4 - \left(\Delta K/2\right)^2}$ from which the power gain of the signal for a TWPA

of length l_T can be determined as

$$\begin{aligned} G_\mathrm{s} &\equiv \left|\frac{A_\mathrm{s}}{A_{\mathrm{s},0}}\right|^2 = \\ &= \left|\cosh g_\mathrm{z} l_\mathrm{T} - \frac{i\Delta K}{2g_\mathrm{z}}\sinh g_\mathrm{z} l_\mathrm{T}\right|^2 + \frac{|A_{\mathrm{i},0}|^2}{|A_{\mathrm{s},0}|^2}\left|\frac{X_\mathrm{s}\,|A_{\mathrm{p},0}|^2}{g_\mathrm{z}}\sinh g_\mathrm{z} l_\mathrm{T}\right|^2 - \\ &\quad - \left(iA_{\mathrm{s},0}A_{\mathrm{i},0}\left(\cosh g_\mathrm{z} l_\mathrm{T} - \frac{i\Delta K}{2g_\mathrm{z}}\sinh g_\mathrm{z} l_\mathrm{T}\right)\frac{X_\mathrm{s}^*\,|A_{\mathrm{p},0}|^2}{g_\mathrm{z}^*\,|A_{\mathrm{s},0}|^2}\sinh g_\mathrm{z}^* l_\mathrm{T} + c.c.\right). \end{aligned} \tag{3.17}$$

3.3.1 Effect of phase matching

As noted in section 3.2, the amplification process is most efficient if $\Delta\Omega = 0$. As will become clear from the quantum mechanical treatment of the problem in due course, $\Delta\Omega$ corresponds to ΔK in equation (3.16). However, due to dispersion (equation (3.10)) and cross modulation (equation (3.11)) this term cannot be 0 in a transmission line embedded with Josephson junctions. In order to bring it closer to 0, we need dispersion engineering. In [18], dispersion engineering is

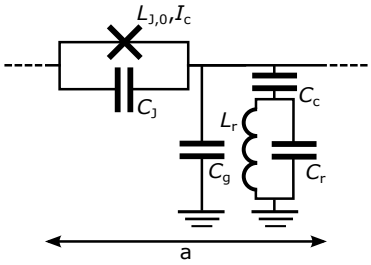


Figure 3.5: *Unit cell of a Josephson junction embedded transmission line with a resonator for achieving phase matching between the pump, signal and idler mode in a TWPA.*

achieved by embedding resonators in each unit cell in figure 3.4, as depicted in figure 3.5. If the pump tone is chosen at a frequency close to the resonance frequency of the resonators, the result is that every resonator gives the tone a small phase kick (without diminishing the tone's amplitude too much) and $\Delta K \approx 0$ may be accomplished. The phase kick required per resonator depends on the density of resonators. [18] puts a resonator in every unit cell, such that the phase kick per resonator only needs to be very small. This implies that only a little of the pump amplitude will be reflected. Contrarily, [12] puts a resonator after 17 unit cells each containing three Josephson junctions, such that the required amount of phase shift per resonator is larger, resulting in a larger reflected pump amplitude accordingly.

In case every unit cell contains a resonator, taking its effect on the theory into account is straightforward: we replace the capacitance C_g by an impedance

$$Z_{C_\mathrm{eff},n} = Z_{C_\mathrm{g},n} /\!\!/ Z_{\mathrm{r},n} = \frac{1}{i\omega_n C_\mathrm{g}} + \frac{1 - L_\mathrm{r}\left(C_\mathrm{r} + C_\mathrm{c}\right)\omega_n^2}{i\omega_n C_\mathrm{c}\left(1 - L_\mathrm{r} C_\mathrm{r}\omega_n^2\right)} \tag{3.18}$$

in which L_r and C_r are the inductance and capacitance of the resonator with a resonance at $\omega_\mathrm{r} = 1/\sqrt{L_\mathrm{r} C_\mathrm{r}}$. C_c is the coupling capacitance between the resonator and the transmission line. Subsequently, we substitute $1/i\omega_n Z_{C_\mathrm{eff},n}$ for C_g in the coupling constants Ξ_n and X_n in equations (3.11) and (3.12), such that

$$\Xi_n^\mathrm{PM} = \frac{i a^4 k_\mathrm{p}^2 k_n^3 \omega_n Z_{C_\mathrm{eff},n}}{16 I_\mathrm{c}^2 L_{\mathrm{J},0}^3 \omega_n^2}\left(2 - \delta_{\mathrm{p}n}\right) \tag{3.19}$$

$$X_n^\mathrm{PM} = \frac{i a^4 k_\mathrm{p}^2 k_\mathrm{s} k_\mathrm{i} \omega_n Z_{C_\mathrm{eff},n}}{16 I_\mathrm{c}^2 L_{\mathrm{J},0}^3 \omega_n^2}\left(k_n - \varepsilon_n \Delta k\right). \tag{3.20}$$

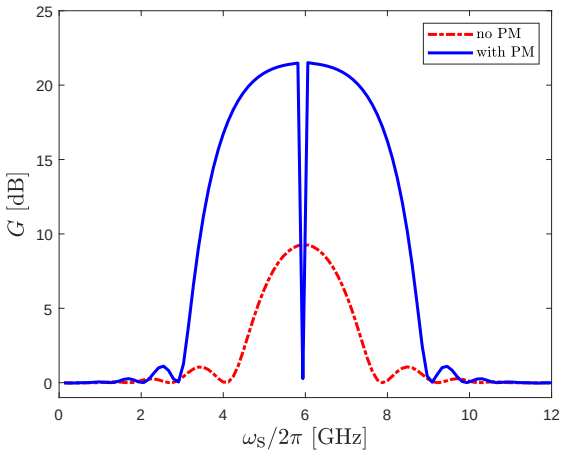


Figure 3.6: *Predicted power gain as function of signal frequency without and with phase matching with parameters taken from [18]. The pump frequency and current are* 5.97 GHz *and* $0.5 I_c$ *and the initial idler current is* 0. *The transmission line parameters are* $L_{J,0} = 100\,\mathrm{pH}$ *(*$I_c = 3.29\,\mu\mathrm{A}$*),* $C_J = 329\,\mathrm{fF}$ *and* $C_g = 39\,\mathrm{fF}$ *and the resonator parameters* $C_c = 10\,\mathrm{fF}$, $L_r = 100\,\mathrm{pH}$ *and* $C_r = 7.036\,\mathrm{pF}$. *The calculations have been performed taking into account* 2000 *unit cells of* $10\,\mu\mathrm{m}$ *length. The dip in the plot for a TWPA with phase matching actually contains two dips on closer inspection. They result from the signal and idler being on resonance with the phase matching resonators respectively.*

The effect of phase matching on the performance of the TWPA is depicted in figure 3.6. The red dash-dotted curve results from equation (3.17) without

phase matching with $L_{J,0} = 100\,\text{pH}$ ($I_c = 3.29\,\mu\text{A}$), $C_J = 329\,\text{fF}$ and $C_g = 39\,\text{fF}$ with 2000 unit cells of $10\,\mu\text{m}$. The blue continuous curve results from adding resonators to the unit cells and evaluating equation (3.17). For the resonators $C_c = 10\,\text{fF}$, $L_r = 100\,\text{pH}$ and $C_r = 7.036\,\text{pF}$. In both calculations the pump current, which is linked to the mode amplitude via the characteristic impedance of the TWPA as $I_p = -A_{p,0}\omega_p/Z_c$, is set to $0.5I_c$ at $\omega_p = 2\pi \times 5.97\,\text{GHz}$. The initial idler current is set to 0.

In the case that one only adds resonators at specific points in the structure, these can be taken into account by evaluating the amplifier in parts. The resonators divide the structure in sections. Within each section, the evolution of the mode amplitudes follows equation (3.16) with the coupling constants as given by equations (3.11) and (3.12). Then, between two sections, one evaluates the transmission coefficient due to the presence of the resonator, updates the mode amplitudes accordingly and uses those amplitudes as input for the next section.

3.4 Quantum theory of parametric amplification (4WM)

In this section we derive the quantum Hamiltonian for the TWPA. In quantum theory the evolution of the state vector, $|\psi\rangle$, describing the system is determined by the Schrödinger equation,

$$i\hbar\frac{\partial\,|\psi\rangle}{\partial t} = \hat{H}\,|\psi\rangle\,. \tag{3.21}$$

where $\hbar$ is the reduced Planck constant $h/2\pi$. Hence, in order to understand the quantum behaviour of a parametric amplifier, we need to derive its Hamiltonian. In this section the Hamiltonian for a 4WM parametric amplifier, where the non-linearity is provided by Josephson junctions, is derived within Fock space for discrete modes. Although this may sound quite limiting, it should be noted that the same method can be easily applied to 3WM devices or devices with another source of the non-linearity.
We derive the Hamiltonian in three steps. After covering the concept of energy in transmission lines, a concept which the rest of the derivation relies on, first a dispersionless LC-transmission line is quantised. As a second step, dispersion is added to this transmission line by adding an additional capacitance parallel to the inductance. As a final step the inductance is replaced by a Josephson junction.

3.4.1 Energy in transmission lines

Typically, non-dissipative transmission lines are quantised as electromagnetic circuits using currents (I), fluxes (Φ), voltages (V) and charges (Q) as quantum

fields [24]. These give rise to a Hamiltonian via the inductors and capacitors that characterise the line. The energy stored in these elements is given by

$$U(t) = \int_{t_0}^{t} P \, \mathrm{d}t' = \int_{t_0}^{t} V I \, \mathrm{d}t' \tag{3.22}$$

– the energy is given by the time-integrated power, P, through the element, which equals the product of voltage and current. Now the only task is to calculate the voltage over and current through the element, integrate and sum over all the elements in the circuit. Specifically, for inductors

$$U = \begin{cases} \int_{I(t_0)}^{I(t)} LI \, \mathrm{d}I' = \frac{1}{2} L I^2 \\ \int_{\Phi(t_0)}^{\Phi(t)} \frac{1}{L} \Phi \, \mathrm{d}\Phi' = \frac{1}{2L} \Phi^2 \end{cases} \tag{3.23}$$

using the current-voltage relation for inductors $V = L\partial I/\partial t$ in the first line and Faraday's induction law $V = \partial \Phi/\partial t$ along with $\Phi = LI$ in the second. Note that it is implicitly assumed that the current and flux are 0 at $t = t_0$. This proves to be a critical assumption of utmost importance as will be shown in section 3.4.3. For the energy stored in capacitors, the same form of the energy arises if we interchange current with voltage, flux with charge and inductance with capacitance in equation (3.23).

3.4.2 Quantisation of a non-dispersive transmission line

Consider once more the transmission line in figure 3.4. For the moment we neglect the non-linearity of the Josephon junction and the Josephson capacitance C_J, in which case the line is just an ordinary LC-transmission line without dispersion, as depicted in figure 3.7.

As suggested by the previous section, we postulate the following mesoscopic

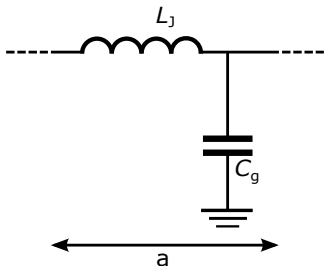


Figure 3.7: *Unit cell of a dispersionless LC-transmission line.*

Hamiltonian for an electromagnetic (EM) field transmitting through the transmission line

$$\hat{H} = \int_{l_\mathrm{q}} \frac{1}{2} \mathcal{L}_\mathrm{J} \hat{I}_{L_\mathrm{J}}{}^2 + \frac{1}{2} \mathcal{C}_\mathrm{g} \hat{V}_{C_\mathrm{g}}{}^2 \, \mathrm{d}z. \tag{3.24}$$

Here, $\mathcal{L}_\mathrm{J} = L_\mathrm{J}/a$ is the inductance per unit length and $\mathcal{C}_\mathrm{g} = C_\mathrm{g}/a$ the capacitance per unit length. $\hat{I}_{L_\mathrm{J}}$ is the current through the inductor L_J and $\hat{V}_{C_\mathrm{g}}$ is the voltage over the capacitor C_g. l_q is the quantisation length [25].
As in the classical theory, we assume sinusoidal waves passing through the line. In this case

$$\hat{V}_{C_\mathrm{g}} = \sum_n \hat{V}_{C_\mathrm{g},\,n} = \sum_n \sqrt{\frac{\hbar\omega_n}{2\mathcal{C}_\mathrm{g} l_\mathrm{q}}} \left(\hat{a}_n e^{i(k_n z - \omega_n t)} + \mathrm{H.c.}\right), \tag{3.25}$$

as suggested by [24], adapted for discrete mode operators [25]. For waves travelling in positive z-direction, the wave number k_n is positive and will be labelled by a positive n. Waves travelling in negative z-direction have a negative wave number and will therefore be labelled by a negative n. In general, $k_{-n} = -k_n$. For frequencies we have $\omega_{-n} = \omega_n$. The characteristic impedance of this line is given by $Z_\mathrm{c} = \sqrt{\mathcal{L}_\mathrm{J}/\mathcal{C}_\mathrm{g}}$ and the phase velocity of the travelling waves equals $v_\mathrm{ph} = \omega_n/|k_n| = 1/\sqrt{\mathcal{L}_\mathrm{J}\mathcal{C}_\mathrm{g}}$.
From this voltage we determine the current through the inductor by the telegrapher's equations. Specifically

$$\frac{\partial V_n}{\partial z} = -\mathcal{L}\frac{\partial I_n}{\partial t}. \tag{3.26}$$

Thus,

$$\hat{I}_{L_\mathrm{J}} = \sum_n \hat{I}_{L_\mathrm{J},\,n} = \sum_n \mathrm{sgn}(n) \sqrt{\frac{\hbar\omega_n}{2\mathcal{L}_\mathrm{J} l_\mathrm{q}}} \left(\hat{a}_n e^{i(k_n z - \omega_n t)} + \mathrm{H.c.}\right). \tag{3.27}$$

Substituting relations (3.27) and (3.25) into equation (3.24) and using that

$$\begin{aligned}\int_{l_\mathrm{q}} \mathrm{e}^{i(\Delta k_{nm})z}\,\mathrm{d}z &= \begin{cases} l_\mathrm{q}\,\mathrm{sinc}\left(\Delta k_{nm} l_\mathrm{q}/2\right) & \text{if } -l_\mathrm{q}/2 \le z \le l_\mathrm{q}/2 \\ & \text{(symmetric bounds)} \\ -i\left(\mathrm{e}^{i\Delta k_{nm} l_\mathrm{q}} - 1\right)/\Delta k_{nm} & \text{if } 0 \le z \le l_\mathrm{q} \\ & \text{(asymmetric bounds)} \end{cases} \\ &\approx l_\mathrm{q}\delta_{\Delta k_{nm}}\end{aligned} \tag{3.28}$$

with $\Delta k_{nm} \equiv \pm k_n \pm k_m$. Here, the plus (minus) sign should be chosen if the wave number is associated to an annihilation (creation) operator. The approximation holds if $\Delta k_{nm} l_\mathrm{q} \ll 1$, for which

$$\delta_{\Delta k_{nm}} = \begin{cases} 1 & \text{if } \Delta k_{nm} l_\mathrm{q} = 0 \\ 0 & \text{else,} \end{cases} \tag{3.29}$$

such that we arrive at

$$\hat{H}_0 = \sum_n \frac{1}{2}\hbar\omega_n \left(\hat{a}_n^\dagger \hat{a}_n + \hat{a}_n \hat{a}_n^\dagger\right) = \sum_n \hbar\omega_n \left(\hat{a}_n^\dagger \hat{a}_n + \frac{1}{2}\right), \tag{3.30}$$

taking into account the commutation relation $\left[\hat{a}_n, \hat{a}_m^\dagger\right] = \hat{\delta}_{nm}$ (See [25] for details).

3.4.3 The influence of the Josephson capacitance: quantisation of a dispersive transmission line

So far we have been neglecting the influence of the parallel capacitor C_J in the transmission line under consideration. Taking this capacitance into account leads to alterations to the theory presented so far, because we now have a capacitor C_J parallel to the inductor L_J, as shown in figure 3.8. For frequencies

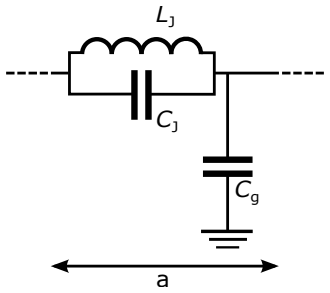


Figure 3.8: *Unit cell of an LC-transmission line in which dispersion is added due to the capacitor C_J parallel to the inductor L_J.*

$\omega_n < 1/\sqrt{L_\mathrm{J} C_\mathrm{J}}$ this can be taken into account by a frequency-dependent inductance,

$$L_\mathrm{eff} = \frac{L_\mathrm{J}}{1 - L_\mathrm{J} C_\mathrm{J} \omega_n^2} \equiv L_\mathrm{J} \Lambda_n, \tag{3.31}$$

and as a result, first

$$Z_{\mathrm{c},n} = \sqrt{\frac{\mathcal{L}_\mathrm{J} \Lambda_n}{\mathcal{C}_\mathrm{g}}}, \quad v_{\mathrm{ph},n} = \frac{1}{\sqrt{\mathcal{L}_\mathrm{J} \Lambda_n \mathcal{C}_\mathrm{g}}} = \frac{\omega_n}{|k_n|}, \tag{3.32}$$

implying dispersion is added to the problem, since the phase velocity is now frequency dependent. Secondly, we have to add an additional capacitive energy to the Hamiltonian.

For didactic reasons we now give two derivations of the Hamiltonian in which we take the parallel capacitor into account. In equations (3.33) to (3.36) we present an erroneous approach, after which the correct manner is presented.

Intuitively, the energy contribution of C_J can be added to the Hamiltonian in the same way as the energy stored in C_g. That is,

$$\hat{H} = \int_l \frac{1}{2} \mathcal{L}_\mathrm{J} \hat{I}_{L_\mathrm{J}}{}^2 + \frac{1}{2} \mathcal{C}_\mathrm{J} \Delta \hat{V}_{C_\mathrm{J}}{}^2 + \frac{1}{2} \mathcal{C}_\mathrm{g} \hat{V}_{C_\mathrm{g}}{}^2 \, \mathrm{d}z. \tag{3.33}$$

Realising that $\Delta\hat{V}_{C_\mathrm{J}} = \Delta\hat{V}_{L_\mathrm{J}} = \Delta\hat{V}_{L_\mathrm{eff}}$, it can be calculated by the current-voltage relationship for inductors. The current through L_eff equals the current in equation (3.27) with $L_\mathrm{J} \mapsto L_\mathrm{eff}$. Thus,

$$\begin{aligned}\Delta\hat{V}_{L_\mathrm{eff}} = \sum_n \Delta\hat{V}_{L_\mathrm{eff},\,n} = L\sum_n \Lambda_n \frac{\partial \hat{I}_{L_\mathrm{eff},\,n}}{\partial t} \\ = \sum_n k_n a \sqrt{\frac{\hbar\omega_n}{2\mathcal{C}_\mathrm{g} l_\mathrm{q}}} \left(-i\hat{a}_n e^{i(k_n z - \omega_n t)} + \mathrm{H.c.}\right).\end{aligned} \tag{3.34}$$

Using the same relationship, we can calculate $\hat{I}_{L_\mathrm{J}}$ as

$$\hat{I}_{L_\mathrm{J}} = \frac{1}{L_\mathrm{J}} \int \Delta\hat{V}_{L_\mathrm{J}}\,\mathrm{d}t = \sum_n \frac{k_n}{\mathcal{L}_\mathrm{J}\omega_n} \sqrt{\frac{\hbar\omega_n}{2\mathcal{C}_\mathrm{g} l_\mathrm{q}}} \left(\hat{a}_n e^{i(k_n z - \omega_n t)} + \mathrm{H.c.}\right) \tag{3.35}$$

and we can use the methods of the last section to find (Wrong!)

$$\hat{H}_0 = \sum_n \frac{1}{2}\hbar\omega_n \left(\hat{a}_n^\dagger \hat{a}_n + \frac{1}{2}\right)(\Lambda_n + (\Lambda_n - 1) + 1) = \sum_n \hbar\omega_n \Lambda_n \left(\hat{a}_n^\dagger \hat{a}_n + \frac{1}{2}\right). \tag{3.36}$$

This is an odd result: in the transmission line fed by a mode oscillating at a frequency ω_n the mode seems to oscillate at $\omega_n\Lambda_n$. Indeed, the result is simply wrong by the exact reason pointed out in section 3.4.1. The voltage in equation (3.25) is "cosine-like", whereas $\Delta\hat{V}_{C_\mathrm{J}}$ is "sine-like"[2]. This implies that the energy cannot be 0 in all elements at the same time, as we assumed in equation (3.23). Although the sine-like operator $\Delta\hat{V}_{C_\mathrm{J}}$ is unsuitable to be used for the purpose of the derivation of the Hamiltonian, it should be noted that $\Delta\hat{V}_{C_\mathrm{J}}$ is a "valid" operator in itself and thus it is suitable for calculating expectation values from some quantum state $|\psi\rangle$.

To solve this problem, consider once more the energy stored in C_J,

$$U_{C_\mathrm{J}} = \int_{t_0}^{t} V_{C_\mathrm{J}} I_{C_\mathrm{J}}\,\mathrm{d}t' = \frac{1}{2} C_\mathrm{J} V_{C_\mathrm{J}}^2 \tag{3.37}$$

However, we can also cast this energy in terms of the flux, given by Faraday's induction law as

$$\Phi = \int V\,\mathrm{d}t. \tag{3.38}$$

[2] In the sense that the expectation value of the operator on a coherent state $|\alpha\rangle$ with $\alpha \in \mathbb{R}$ scales as either a cosine or a sine.

Since the flux is the time-integrated voltage, it will be cosine-like, whenever the voltage is sine-like and vice versa. From the definition

$$U_{C_\mathrm{J}} = \int_{t_0}^{t} V_{C_\mathrm{J}} I_{C_\mathrm{J}} \,\mathrm{d}t' = \int_{t_0}^{t} C_\mathrm{J} \frac{\mathrm{d}\,\Phi_{C_\mathrm{J}}}{\mathrm{d}t'} \frac{\mathrm{d}^2\,\Phi_{C_\mathrm{J}}}{\mathrm{d}t'^2} \,\mathrm{d}t' = -\omega^2 C_\mathrm{J}\, \Phi_{C_\mathrm{J}}^2, \tag{3.39}$$

using the current-voltage relation for capacitors $I = C\partial V/\partial t$ and that $\partial^2 \Phi/\partial t^2 = -\omega^2 \Phi$. This suggests that a more fruitful approach is to start out with

$$\hat{H} = \frac{1}{2a^2} \int_{l_\mathrm{q}} \frac{1}{\mathcal{L}_\mathrm{J}} \Delta\hat{\Phi}_{L_\mathrm{J}}{}^2 + \mathcal{C}_\mathrm{J} a^2 \Delta\hat{\Phi}_{C_\mathrm{J}} \frac{\partial^2 \Delta\hat{\Phi}_{C_\mathrm{J}}}{\partial t^2} + \frac{1}{\mathcal{C}_\mathrm{g}} \hat{Q}_{C_\mathrm{g}}{}^2 \,\mathrm{d}z. \tag{3.40}$$

In the above equation we switched to flux and charge variables in all terms for aesthetic reasons. For the first and third term we might use the current and voltage variable just as well. The fluxes can be computed from either equation (3.34) or (3.35), and it follows

$$\Delta\hat{\Phi}_{L_\mathrm{J}} = \Delta\hat{\Phi}_{C_\mathrm{J}} = \Delta\hat{\Phi}_{L_\mathrm{eff}} = \sum_n \frac{k_n a}{\omega_n} \sqrt{\frac{\hbar\omega_n}{2\mathcal{C}_\mathrm{g} l_\mathrm{q}}} \left(\hat{a}_n e^{i(k_n z - \omega_n t)} + \mathrm{H.c.}\right). \tag{3.41}$$

Substituting, the Hamiltonian (3.40) yields

$$\hat{H}_0 = \sum_n \hbar\omega_n \left(\hat{a}_n^\dagger \hat{a}_n + \frac{1}{2}\right) \tag{3.42}$$

as expected.

This result can be generalised for any lossless, linear transmission line. From equation (3.40) we can infer that we can describe the same problem with just two terms in the Hamiltonian. Rewriting equation (3.40) we find

$$\begin{aligned} \hat{H} &= \frac{1}{2a} \int_{l_\mathrm{q}} \left(\frac{1}{L_\mathrm{J}} \Delta\hat{\Phi}_{L_\mathrm{J}} + C_\mathrm{J} \frac{\partial \Delta\hat{V}_{C_\mathrm{J}}}{\partial t}\right) \Delta\hat{\Phi}_{C_\mathrm{J}} + C_\mathrm{g} \hat{V}_{C_\mathrm{g}}{}^2 \,\mathrm{d}z = \\ &= \frac{1}{2a} \int_{l_\mathrm{q}} \hat{I}_{L_\mathrm{eff}} \Delta\hat{\Phi}_{L_\mathrm{eff}} + C_\mathrm{g} \hat{V}_{C_\mathrm{g}}{}^2 \,\mathrm{d}z \end{aligned} \tag{3.43}$$

as $I_{L_\mathrm{eff}} = I_{L_\mathrm{J}} + I_{C_\mathrm{J}}$. The same argument holds if C_g is replaced by a frequency-dependent effective capacitance C_eff, such that we may write

$$\hat{H} = \frac{1}{2a} \int_{l_\mathrm{q}} \hat{I}_{L_\mathrm{eff}} \Delta\hat{\Phi}_{L_\mathrm{eff}} + \hat{V}_{C_\mathrm{eff}} \hat{Q}_{C_\mathrm{eff}} \,\mathrm{d}z \tag{3.44}$$

for any lossless linear transmission line. This yields equation (3.42) after substitution of the quantum fields.

3.4.4 Adding the non-linearity: quantisation of a non-linear transmission line

As a last step we replace the inductor L_J, which we considered as an inductor with a fixed value up to this point, by a Josephson junction. The unit cell for such a transmission line is depicted in figure 3.9.

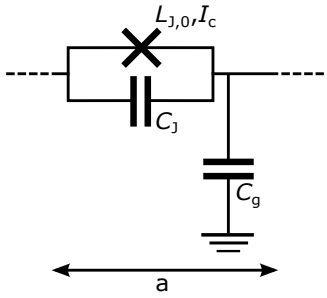


Figure 3.9: *Unit cell of a Josephson junction embedded transmission line in which the Josephson junction is modelled as a non-linear inductor, L_J, with a parallel capacitor C_J.*

The current through a Josephson junction is

$$I_\mathrm{J} = I_\mathrm{c} \sin\left(\frac{\Delta\Phi_\mathrm{J}}{\varphi_0}\right) \tag{3.45}$$

with $\varphi_0 = \hbar/2e$ the reduced magnetic flux quantum, $\Phi_0/2\pi$, and e the elementary charge. From the current, we can calculate the Josephson energy in the usual fashion

$$U_\mathrm{J} = \int_{t_0}^{t} VI \,\mathrm{d}t' = \int_{t_0}^{t} \frac{\mathrm{d}\Delta\Phi_\mathrm{J}}{\mathrm{d}t'} I_\mathrm{c} \sin\left(\frac{\Delta\Phi_\mathrm{J}}{\varphi_0}\right) \,\mathrm{d}t' = I_\mathrm{c}\varphi_0 \left(1 - \cos\left(\frac{\Delta\Phi_\mathrm{J}}{\varphi_0}\right)\right). \tag{3.46}$$

Substituting this energy for the inductive energy in equation (3.40) yields

$$\begin{aligned}\hat{H} &= \frac{1}{2a^2}\int_{l_\mathrm{q}} 2aI_\mathrm{c}\varphi_0 \left(1 - \cos\left(\frac{\Delta\hat{\Phi}_\mathrm{J}}{\varphi_0}\right)\right) + \mathcal{C}_\mathrm{J} a^2 \Delta\hat{\Phi}_\mathrm{J} \frac{\partial^2 \Delta\hat{\Phi}_\mathrm{J}}{\partial t^2} + \frac{1}{\mathcal{C}_\mathrm{g}} \hat{Q}_{C_\mathrm{g}}{}^2 \,\mathrm{d}z \\ &= \frac{1}{2a^2}\int_{l_\mathrm{q}} \left(\frac{1}{\mathcal{L}_{\mathrm{J},0}}\Delta\hat{\Phi}_\mathrm{J} - \frac{1}{12\mathcal{L}_{\mathrm{J},0}\varphi_0^2}\Delta\hat{\Phi}_\mathrm{J}{}^3 + \mathcal{O}\left(\Delta\hat{\Phi}_\mathrm{J}{}^5\right) + \right. \\ &\qquad \left. + \mathcal{C}_\mathrm{J} a^2 \frac{\partial^2 \Delta\hat{\Phi}_\mathrm{J}}{\partial t^2}\right)\Delta\hat{\Phi}_\mathrm{J} + \frac{1}{\mathcal{C}_\mathrm{g}} \hat{Q}_{C_\mathrm{g}}{}^2 \,\mathrm{d}z.\end{aligned} \tag{3.47}$$

in which we have Taylor-expanded the cosine-term and defined the Josephson inductance as $L_{\mathrm{J},0} = \varphi_0/I_\mathrm{c}$. From this equation it is clear immediately that the generalised Hamiltonian of equation (3.44) does not capture the non-linear behaviour.

To address the non-linearity of the transmission line we also calculate the non-linear flux operator derived from equation (3.41). The dependence of L_J and thus Λ_n in the non-linear flux operator on $\Delta\Phi_\mathrm{J}$ is found from the Josephson current and the flux $\Delta\Phi_\mathrm{J} = L_\mathrm{J} I_\mathrm{J}$,

$$L_\mathrm{J}(\Delta\Phi_\mathrm{J}) = \frac{\varphi_0}{I_\mathrm{c}} \frac{\Delta\Phi_\mathrm{J}/\varphi_0}{\sin\left(\Delta\Phi_\mathrm{J}/\varphi_0\right)} \equiv L_{\mathrm{J},0} \frac{\Delta\Phi_\mathrm{J}/\varphi_0}{\sin\left(\Delta\Phi_\mathrm{J}/\varphi_0\right)} \tag{3.48}$$

Furthermore, as in the classical theory, we give an explicit time and spatial dependence to the creation and annihilation operators, $\hat{a}_n{}^{(\dagger)} \mapsto \hat{a}_n{}^{(\dagger)}(z,t)$, in the voltage operator of equation (3.25). Invoking the slowly varying amplitude approximation, the time and spatial dependence of these operators is neglected in deriving the other field operators. Hence, from equation (3.41), we find for the non-linear Josephson junction flux operator

$$\begin{aligned}\Delta\hat{\Phi}_\mathrm{J} =& \sum_n a \sqrt{\frac{\hbar\omega_n}{2l_\mathrm{q}} \frac{\mathcal{L}_{\mathrm{J},0}\Delta\hat{\Phi}_\mathrm{J}/\varphi_0}{\sin\left(\Delta\hat{\Phi}_\mathrm{J}/\varphi_0\right) - \omega_n^2 L_\mathrm{J} C_\mathrm{J} \Delta\hat{\Phi}_\mathrm{J}/\varphi_0}} \left(\hat{a}_n e^{i(k_n z - \omega_n t)} + \mathrm{H.c.}\right) \\ =& \sum_n \sqrt{\frac{1}{1 - \Lambda_n \sum_{m,l} \Delta\hat{\Phi}_{\mathrm{J},m}\Delta\hat{\Phi}_{\mathrm{J},l}/6\varphi_0^2 + \mathcal{O}\left(\Delta\hat{\Phi}_\mathrm{J}{}^4\right)}} \Delta\hat{\Phi}_{\mathrm{J},n}{}^{(0)}\end{aligned} \tag{3.49}$$

with $\Delta\hat{\Phi}_{\mathrm{J},n}{}^{(0)}$ given by equation (3.41). In the second line of this equation, we have written explicitly that $\Delta\hat{\Phi}_\mathrm{J}{}^2 = \sum_{n,m} \Delta\hat{\Phi}_{\mathrm{J},n}\Delta\hat{\Phi}_{\mathrm{J},m}$. This recurrent relation can be solved iteratively resulting in

$$\Delta\hat{\Phi}_\mathrm{J} = \sum_n \left(1 + \frac{\Lambda_n}{12}\left(\frac{\Delta\hat{\Phi}_\mathrm{J}{}^{(0)}}{\varphi_0}\right)^2 + \mathcal{O}\left(\left(\frac{\Delta\hat{\Phi}_\mathrm{J}{}^{(0)}}{\varphi_0}\right)^4\right)\right) \Delta\hat{\Phi}_{\mathrm{J},n}{}^{(0)} \tag{3.50}$$

Substitution of this expression in the Hamiltonian of equation (3.47) yields the Hamiltonian for a 4WM parametric amplifier where the non-linearity is due to Josephson junctions. Up to first non-linear order (or fourth order in $\Delta\hat{\Phi}_\mathrm{J}$) we

find

$$\begin{aligned}\hat{H}_{\mathrm{TWPA}} = &\sum_n \hbar\omega_n \left(\hat{a}_n^\dagger \hat{a}_n + \frac{1}{2}\right) + \\ &+ \sum_{n,m,l,k} \frac{-i\hbar^2 \mathrm{e}^{-i\Delta\omega_{nmlk}t}}{96\mathcal{L}_{\mathrm{J},0} I_{\mathrm{c}}^2 l_{\mathrm{q}}^2 \Delta k_{nmlk}} \left(\mathrm{e}^{i\Delta k_{nmlk} l_{\mathrm{q}}} - 1\right) \cdot \\ &\cdot \Bigg[\left(1 - 4L_{\mathrm{J},0}\Lambda_n C_{\mathrm{J}} \omega_k^2\right) \left\{\hat{\tilde{a}} + \mathrm{H.c.}\right\}_{n\cdot m\cdot l\cdot k} + \\ &+ 4L_{\mathrm{J},0}\Lambda_n C_{\mathrm{J}} \Bigg(2 \left\{\omega\left(-i\hat{\tilde{a}} + \mathrm{H.c.}\right)\right\}_{n\cdot m} \left\{\hat{\tilde{a}} + \mathrm{H.c.}\right\}_{l\cdot k} + \\ &+ \left\{\hat{\tilde{a}} + \mathrm{H.c.}\right\}_{n\cdot m} \left\{\omega\left(-i\hat{\tilde{a}} + \mathrm{H.c.}\right)\right\}_{l\cdot k} \Bigg) \Bigg],\end{aligned} \tag{3.51}$$

where $\hat{\tilde{a}}_n \equiv \mathrm{sgn}\,(n)\sqrt{\Lambda_n\omega_n}\hat{a}_n$ and we have chosen the asymmetric integral bounds of equation (3.28). The subscript $n\cdot m\cdot l\cdot k$ below the braces indicates multiplication, e.g. $\{\Lambda\omega\}_{n\cdot m} = \Lambda_n\omega_n\Lambda_m\omega_m$. $\Delta k_{nmlk} \equiv \pm k_n \pm k_m \pm k_l \pm k_k$ for the different terms resulting from expansion of the brackets. A plus (minus) sign refers to a corresponding annihilation (creation) operator, e.g. the term $\hat{a}_n\hat{a}_m^\dagger\hat{a}_l^\dagger\hat{a}_k$ corresponds to $\Delta k_{nmlk} = k_n - k_m - k_l + k_k$. Similarly, $\Delta\omega_{nmkl} \equiv \pm\omega_n \pm \omega_m \pm \omega_l \pm \omega_k$.

This is the main result of this chapter. This Hamiltonian describes the full quantum behaviour of Josephson TWPAs up to first non-linear order. However, we will point out two remaining issues and how they may be dealt with. Firstly, this Hamiltonian does not conserve energy a priori. For energy conservation $\Delta\omega_{nmlk}$ must equal 0, which does not follow necessarily from the equation. At this point we can demand energy conservation by considering only interactions between modes for which $\Delta\omega_{nmlk} = 0$. However, one could also reason that $\Delta\omega_{nmlk} \neq 0$ adds to the phase mismatching term $\Delta\Omega$ in equation (3.4), which at small magnitudes (compared to ω_n) already greatly reduces the gain of the amplifier. From this argument it follows that $\Delta\omega_{nmlk} \approx 0$. If the latter is the case, and $\Delta\omega_{nmlk}$ is not strictly 0 this might lead to line broadening of the modes. For now we will assume strict energy conservation and demand $\Delta\omega_{nmlk} = 0$.

A second problem in the expression above is the explicit dependence of the mixing term on the quantisation length. This dependence arises both as a consequence of the dispersion in the line as well as an intrinsic dependence of the mixing term that scales as l_{q}^{-2}. Due to dispersion, Δk_{nmlk} and $\Delta\omega_{nmlk}$ cannot equal 0 simultaneously, which introduces an l_{q}-dependence if we demand $\Delta\omega_{nmlk} = 0$ for the interacting modes.
Partly, the two contributions to the quantisation length dependence of the

mixing term cancel each other as

$$\frac{-i\left(\mathrm{e}^{i\Delta k_{nmlk} l_\mathrm{q}}-1\right)}{\Delta k_{nmlk}} = l_\mathrm{q}\left(1-\frac{i}{2}\Delta k_{nmlk} l_\mathrm{q}+\mathcal{O}\left(\left(\Delta k_{nmlk} l_\mathrm{q}\right)^2\right)\right). \tag{3.52}$$

The intrinsic dependence of the mixing term on l_q can be further resolved by introducing a classical pump – see section 3.5. To deal with the remaining l_q-dependence due to dispersion, we can assume that the dispersion effects are small enough such that $\Delta k_{nmlk} \approx 0$, while $\Delta\omega_{nmlk} = 0$. We will make this assumption in the following sections. The problem is also resolved considering a transmission line of length l_q for quantisation, of which just a part contains Josephson junctions and using continuous mode quantisation [21].

3.5 Implementations

Using equation (3.51) one can analyse the different implementations of an amplifier. In this section, we will study the non-degenerate amplifier with degenerate pump in detail, the same amplifier implementation that was studied classically in section (3.3). Treating the pump as a classical mode, we will solve the problem of the explicit appearance of the quantisation length in the mixing coupling constants in section 3.5.1. The section ends with a short discussion of other implementations of 4WM amplifiers in section 3.5.2.

3.5.1 The non-degenerate parametric amplifier with undepleted degenerate classical pump – quantum theory

As noted in section 3.3, for the non-degenerate parametric amplifier with degenerate pump, it is assumed that only three modes, the pump, signal and idler, play a role. Then, from equation (3.51) we can determine the interaction Hamiltonian of the amplifier as

$$\begin{aligned}\hat{H}_\mathrm{int} = &\sum_{n,m=\mathrm{p,s,i}} \hbar\xi_{nm}\left(\hat{a}_n^\dagger\hat{a}_n\hat{a}_m^\dagger\hat{a}_m+\frac{c_m}{2}\hat{a}_n^\dagger\hat{a}_n+\frac{c_n}{2}\hat{a}_m^\dagger\hat{a}_m\right)+\\ &+\hbar\left(\chi\hat{a}_\mathrm{p}\hat{a}_\mathrm{p}\hat{a}_\mathrm{s}^\dagger\hat{a}_\mathrm{i}^\dagger+\mathrm{H.c.}\right)+\\ &+\sum_{n,m=\mathrm{p,s,i}}\frac{c_n c_m\hbar\xi_{nm}}{2\left(2-\delta_{nm}\right)}-\frac{c_n c_m\hbar\,\xi_{nm}|_{\Lambda=0}\left(8-2\delta_{nm}\right)}{3}\cdot\\ &\cdot\left(\frac{\omega_n}{\omega_m}\left(\Lambda_m-1\right)+\frac{\omega_m}{\omega_n}\left(\Lambda_n-1\right)\right),\end{aligned} \tag{3.53}$$

taking into account the commutation relations explicitly as $c_n \equiv \left[\hat{a}_n, \hat{a}_n^\dagger\right] = \hat{1}$. The first two lines in this equation determine the dynamics of the amplifier,

whereas the last two lines represent the added zero-point energy. The coupling constants are found to be

$$\xi_{nm} = \frac{\hbar\Lambda_n\omega_n\Lambda_m\omega_m}{16I_c^2\mathcal{L}_{\mathrm{J},0}l_\mathrm{q}}\left(2-\delta_{nm}\right)\left(1+\Lambda_{\xi_{nm}}\right) \tag{3.54}$$

$$\chi = \frac{\hbar\Lambda_\mathrm{p}\omega_\mathrm{p}\sqrt{\Lambda_\mathrm{s}\omega_\mathrm{s}\Lambda_\mathrm{i}\omega_\mathrm{i}}}{8I_c^2\mathcal{L}_{\mathrm{J},0}l_\mathrm{q}}\left(1+\Lambda_\chi\right) \tag{3.55}$$

where

$$\Lambda_{\xi_{nm}} \equiv \frac{2}{3}\left(\frac{\Lambda_n}{\Lambda_m}+\frac{\Lambda_m}{\Lambda_n}-2\right) \tag{3.56}$$

$$\begin{aligned}\Lambda_\chi \equiv \frac{L_{\mathrm{J},0}C_\mathrm{J}}{6}\Big(&\omega_\mathrm{p}\omega_\mathrm{s}\big(-2\Lambda_\mathrm{p}+5\Lambda_\mathrm{s}-3\Lambda_\mathrm{i}\big)+\omega_\mathrm{p}\omega_\mathrm{i}\big(-2\Lambda_\mathrm{p}-3\Lambda_\mathrm{s}+5\Lambda_\mathrm{i}\big)+\\&+\omega_\mathrm{s}\omega_\mathrm{i}\big(4\Lambda_\mathrm{p}-2\Lambda_\mathrm{s}-2\Lambda_\mathrm{i}\big)\Big)\end{aligned} \tag{3.57}$$

and $\xi_{nm}|_{\Lambda=0}$ implies that ξ_{nm} should be used without the contribution of $\Lambda_{\xi_{nm}}$.

In equation (3.53), the $\xi_{n=m}$-term represents the self modulation and the $\xi_{n\neq m}$-terms represent the cross modulation. The term in the equation with coupling constant χ is where the magic happens. This term represents the real amplification process in which two pump photons are scattered into a signal and an idler photon.

For a parametric amplifier to work effectively, the device must be driven into its non-linear regime, which is generally achieved by applying a pump current close to the critical current of the device in addition to the much weaker signal current. In this case we can approximate the Hamiltonian to second order in $\hat{a}_{\mathrm{s,i}}{}^{(\dagger)}$. Moreover, as $\hbar\xi_{nn} \ll \hbar\omega_n$, we can neglect the terms resulting from the commutation relations as well. Hence, to a good approximation,

$$\hat{H}_\mathrm{TWPA} \approx \sum_{n=\mathrm{p,s,i}}\hbar\omega_n\hat{a}_n^\dagger\hat{a}_n + \sum_{n=\mathrm{p,s,i}}\hbar\xi_{\mathrm{p}n}\hat{a}_\mathrm{p}^\dagger\hat{a}_\mathrm{p}\hat{a}_n^\dagger\hat{a}_n + \hbar\left(\chi\hat{a}_\mathrm{p}\hat{a}_\mathrm{p}\hat{a}_\mathrm{s}^\dagger\hat{a}_\mathrm{i}^\dagger + \mathrm{H.c.}\right), \tag{3.58}$$

where we have neglected the constant zero-point energy, which does not influence the dynamics of the amplifier, and we introduced

$$\xi_{\mathrm{p}n} = \frac{\hbar\Lambda_\mathrm{p}\omega_\mathrm{p}\Lambda_n\omega_n}{16I_c^2\mathcal{L}_{\mathrm{J},0}l_\mathrm{q}}\left(4-3\delta_{\mathrm{p}n}\right)\left(1+\Lambda_{\xi_{\mathrm{p}n}}\right). \tag{3.59}$$

Here, the factor $4-3\delta_{nm}$ (instead of $2-\delta_{nm}$) arises from converting the double sum into a single sum. Notably, the coupling constants corresponding to the self- and cross-modulation differ by a numerical factor of 4. In [21] this factor was found to be 2. However, as discussed below, both this work and [21] find

identical operator equations of motion. In equation (3.58), χ is still given by equation (3.55).

Furthermore, we can make the approximation that the pump can be treated as a classical mode and we can replace the corresponding operators with amplitudes. In accordance to the classical treatment of the problem in section 3.3, we will choose the flux, $\hat{\Phi}_{C_\mathrm{g}} = \int \hat{V}_{C_\mathrm{g}}\, \mathrm{d}t$, for the amplitude. Upon comparing this expression with its classical analogue (cf. [25]), equation (3.7), we find

$$\hat{a}_\mathrm{p} \mapsto -i\sqrt{\frac{\omega_\mathrm{p}\mathcal{C}_\mathrm{g} l_\mathrm{q}}{2\hbar}} A_\mathrm{p}. \tag{3.60}$$

Then, for the signal and idler mode, which are still treated quantum mechanically, we find the classical-pump Hamiltonian

$$\hat{H}_{\mathrm{TWPA}}{}^{(\mathrm{CP})} \approx \sum_{n=\mathrm{s,i}} \hbar\left(\omega_n + \xi'_n \left|A_\mathrm{p}\right|^2\right) \hat{a}_n^\dagger \hat{a}_n - \hbar\left(\chi' A_\mathrm{p}^2 \hat{a}_\mathrm{s}^\dagger \hat{a}_\mathrm{i}^\dagger + \mathrm{H.c.}\right) \tag{3.61}$$

with

$$\begin{aligned} \xi'_n &= \frac{\Lambda_\mathrm{p}\omega_\mathrm{p}^2 \Lambda_n \omega_n}{32 I_\mathrm{c}^2 \mathcal{L}_{\mathrm{J},0} Z_{\mathrm{c},p} v_{\mathrm{ph},p}} \left(4 - 3\delta_{\mathrm{p}n}\right)\left(1 + \Lambda_{\xi_{\mathrm{p}n}}\right) = \\ &= \frac{k_\mathrm{p}^2 \Lambda_n \omega_n}{32 I_\mathrm{c}^2 \mathcal{L}_{\mathrm{J},0}^2} \left(4 - 3\delta_{\mathrm{p}n}\right)\left(1 + \Lambda_{\xi_{\mathrm{p}n}}\right) \end{aligned} \tag{3.62}$$

$$\begin{aligned} \chi' &= \frac{\Lambda_\mathrm{p}\omega_\mathrm{p}^2 \sqrt{\Lambda_\mathrm{s}\omega_\mathrm{s}\Lambda_\mathrm{i}\omega_\mathrm{i}}}{16 I_\mathrm{c}^2 \mathcal{L}_{\mathrm{J},0} Z_{\mathrm{c},p} v_{\mathrm{ph},p}} \left(1 + \Lambda_\chi\right) = \\ &= \frac{k_\mathrm{p}^2 \sqrt{\Lambda_\mathrm{s}\omega_\mathrm{s}\Lambda_\mathrm{i}\omega_\mathrm{i}}}{16 I_\mathrm{c}^2 \mathcal{L}_{\mathrm{J},0}^2} \left(1 + \Lambda_\chi\right). \end{aligned} \tag{3.63}$$

Although ξ'_p does not appear in the classical-pump Hamiltonian, it is still defined here for future reference.

Generalising these equations to the case in which resonators are added for dispersion engineering is straightforward. Due to our results in section 3.4.3 this is as easy as making the substitution $C_\mathrm{g} \mapsto 1/i\omega_n Z_{C_\mathrm{eff}}$ (implicit in $Z_{\mathrm{c},n}$, $v_{\mathrm{ph},n}$, k_n and Λ_n) as discussed in section 3.3.1.

To calculate the gain predicted by a parametric amplifier from the quantum theory, we calculate the Heisenberg equations of motion of the operators. By substituting equation (3.58) as the Hamiltonian and approximating the pump as a classical mode, this yields

$$\frac{\partial A_\mathrm{p}}{\partial t} = -i\left(\omega_\mathrm{p} + 2\xi'_\mathrm{p}|A_\mathrm{p}|^2 + c_\mathrm{p}\xi_{\mathrm{pp}}\right) A_\mathrm{p} + 2i\chi'^{*} A_\mathrm{p}^* \hat{a}_\mathrm{s}\hat{a}_\mathrm{i} \tag{3.64}$$

$$\frac{\partial \hat{a}_{\mathrm{s(i)}}}{\partial t} = -i\left(\omega_{\mathrm{s(i)}} + \xi'_{\mathrm{s(i)}}|A_\mathrm{p}|^2\right) \hat{a}_{\mathrm{s(i)}} + i\chi' A_\mathrm{p}^2 \hat{a}_{\mathrm{i(s)}}^\dagger, \tag{3.65}$$

where again we showed the effect of the commutation relations explicitly. However, again we can neglect ξ_{pp}, since $\xi_{\mathrm{pp}} \ll \xi'_{\mathrm{p}}|A_{\mathrm{p}}|^2$. Under the undepleted pump approximation we can neglect the last term in equation (3.64) as well and solve for the pump amplitude directly, as in the classical case. Hence, in the co-rotating frame introduced in section 3.3,

$$\frac{\partial \hat{a}_{\mathrm{s(i)}}}{\partial t} = i\chi' \left|A_{\mathrm{p},0}\right|^2 \hat{a}^\dagger_{\mathrm{i(s)}} \mathrm{e}^{-i\Delta\Omega t}. \tag{3.66}$$

Thus we find, similar to the classical theory

$$\hat{a}_{\mathrm{s(i)}} = \left[\hat{a}_{\mathrm{s(i)},0}\left(\cosh g_{\mathrm{t}} t + \frac{i\Delta\Omega}{2g_{\mathrm{t}}}\sinh g_{\mathrm{t}} t\right) + \right. \\ \left. + \frac{i\chi' \left|A_{\mathrm{p},0}\right|^2}{g_{\mathrm{t}}} \hat{a}^\dagger_{\mathrm{i(s)},0} \sinh g_{\mathrm{t}} t\right] \mathrm{e}^{-i\Delta\Omega t/2} \tag{3.67}$$

with

$$\Delta\Omega = 2\left(\omega_{\mathrm{p}} + 2\xi'_{\mathrm{p}}\left|A_{\mathrm{p},0}\right|^2\right) - \left(\omega_{\mathrm{s}} + \xi'_{\mathrm{s}}\left|A_{\mathrm{p},0}\right|^2\right) - \left(\omega_{\mathrm{i}} + \xi'_{\mathrm{i}}\left|A_{\mathrm{p},0}\right|^2\right) = \\ = \left(4\xi'_{\mathrm{p}} - \xi'_{\mathrm{s}} - \xi'_{\mathrm{i}}\right)\left|A_{\mathrm{p},0}\right|^2 \tag{3.68}$$

$$g_{\mathrm{t}} = \sqrt{\left|\chi'\right|^2 \left|A_{\mathrm{p},0}\right|^4 - \left(\Delta\Omega/2\right)^2}. \tag{3.69}$$

Then, if the state spends a time t_{T} in the TWPA,

$$G_{\mathrm{s,q}} \equiv \frac{\left\langle \hat{a}^\dagger_{\mathrm{s}} \hat{a}_{\mathrm{s}} \right\rangle}{\left\langle \hat{a}^\dagger_{\mathrm{s},0} \hat{a}_{\mathrm{s},0} \right\rangle} = \\ = \left|\cosh g_{\mathrm{t}} t_{\mathrm{T}} + \frac{i\Delta\Omega}{2g_{\mathrm{t}}}\sinh g_{\mathrm{t}} t_{\mathrm{T}}\right|^2 + \frac{\left\langle \hat{a}^\dagger_{\mathrm{i},0}\hat{a}_{\mathrm{i},0}\right\rangle + 1}{\left\langle \hat{a}^\dagger_{\mathrm{s},0}\hat{a}_{\mathrm{s},0}\right\rangle}\left|\frac{\chi'\left|A_{\mathrm{p},0}\right|^2}{g_{\mathrm{t}}}\sinh g_{\mathrm{t}} t_{\mathrm{T}}\right|^2 - \\ - \left(\frac{i\left\langle \hat{a}_{\mathrm{s},0}\hat{a}_{\mathrm{i},0}\right\rangle}{\left\langle \hat{a}^\dagger_{\mathrm{s},0}\hat{a}_{\mathrm{s},0}\right\rangle}\left(\cosh g_{\mathrm{t}} t_{\mathrm{T}} + \frac{i\Delta\Omega}{2g_{\mathrm{t}}}\sinh g_{\mathrm{t}} t_{\mathrm{T}}\right)\frac{\chi'^*\left|A_{\mathrm{p},0}\right|^2}{g^*_{\mathrm{t}}}\sinh g^*_{\mathrm{t}} t_{\mathrm{T}} + c.c.\right) \tag{3.70}$$

in which the term on the second line yields 0 in case the signal or the idler is initially in a number state.

One can also calculate the photon number distribution in the output of a parametric amplifier from the theory in the limit of a classical undepleted pump. To this end we calculate the evolution of the state vector from equation (3.21) in the interaction picture,

$$\left|\psi_{\mathrm{I}}(t)\right\rangle = \mathrm{e}^{-i\hat{H}_{\mathrm{TWPA}}^{(\mathrm{CP,rot})} t/\hbar}\left|\psi_{\mathrm{I}}(0)\right\rangle \tag{3.71}$$

where

$$\hat{H}_{\mathrm{TWPA}}{}^{(\mathrm{CP,rot})} = -\hbar\left(\chi'\left|A_{\mathrm{p}}\right|^2\hat{a}_{\mathrm{s}}^{\dagger}\hat{a}_{\mathrm{i}}^{\dagger}\mathrm{e}^{-i\Delta\Omega t} + \mathrm{H.c.}\right) \tag{3.72}$$

is the classical pump Hamiltonian rewritten in the co-rotating frame. Assuming $\Delta\Omega = 0$ and $\chi' \in \mathrm{Re}$, we can rewrite the propagator in equation (3.71) using an ordering theorem [26]

$$\mathrm{e}^{-i\,\hat{H}_{\mathrm{TWPA}}{}^{(\mathrm{CP,rot})}t/\hbar}\big|_{\Delta\Omega=0} = \mathrm{e}^{i\tanh(\kappa)\hat{a}_{\mathrm{s}}^{\dagger}\hat{a}_{\mathrm{i}}^{\dagger}}\mathrm{e}^{-\ln(\cosh(\kappa))\left(1+\hat{a}_{\mathrm{s}}^{\dagger}\hat{a}_{\mathrm{s}}+\hat{a}_{\mathrm{i}}^{\dagger}\hat{a}_{\mathrm{i}}\right)}\mathrm{e}^{i\tanh(\kappa)\hat{a}_{\mathrm{s}}\hat{a}_{\mathrm{i}}} \tag{3.73}$$

where the amplification $\kappa \equiv \chi'\left|A_{\mathrm{p}}\right|^2 t$.
For a single-photon input state $\left|1\right\rangle_{\mathrm{s}}\left|0\right\rangle_{\mathrm{i}}$, we calculate the output state as

$$\left|\psi_{\mathrm{I}}\left(t\right)\right\rangle = \sum_{n=0}^{\infty}\frac{\left(i\tanh\left(\kappa\right)\right)^n}{\cosh^2\left(\kappa\right)}\sqrt{n+1}\left|n+1\right\rangle_{\mathrm{s}}\left|n\right\rangle_{\mathrm{i}} \tag{3.74}$$

from which we easily compute that the probability of finding N signal photons in the output state equals

$$Pr\left(n_{\mathrm{s}}=N\right) = \left|\left\langle N|\psi_{\mathrm{I}}\left(t\right)\right\rangle\right|^2 = \frac{\tanh\left(\kappa\right)^{2(N-1)}}{\cosh^4\left(\kappa\right)}N. \tag{3.75}$$

For a coherent state $\left|\alpha\right\rangle_{\mathrm{s}}\left|0\right\rangle_{\mathrm{i}}$ we find

$$\left|\psi_{\mathrm{I}}\left(t\right)\right\rangle = e^{-|\alpha|^2/2}\sum_{n,m=0}^{\infty}\frac{\left(i\tanh\left(\kappa\right)\right)^m}{\left(\cosh\left(\kappa\right)\right)^{1+n}}\frac{\alpha^n}{\sqrt{n!}}\sqrt{\binom{n+m}{n}}\left|n+m\right\rangle_{\mathrm{s}}\left|m\right\rangle_{\mathrm{i}} \tag{3.76}$$

and

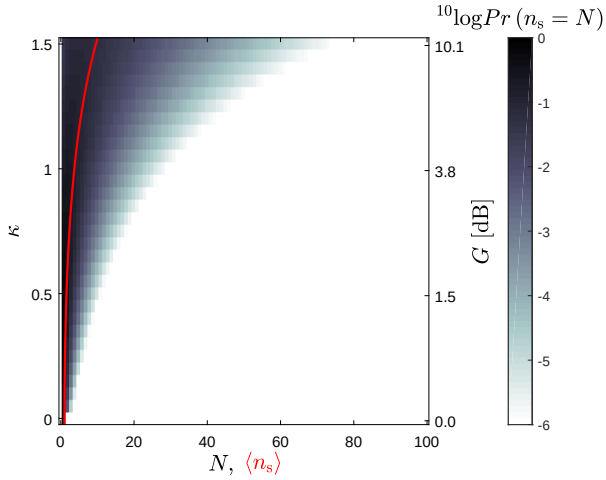
$$Pr\left(n_{\mathrm{s}}=N\right) = e^{-|\alpha|^2}\sum_{n=0}^{N}\frac{\left(\tanh\left(\kappa\right)\right)^{2(N-n)}}{\left(\cosh\left(\kappa\right)\right)^{2(1+n)}}\frac{\left|\alpha\right|^{2n}}{n!}\binom{N}{n}. \tag{3.77}$$

These probabilities are visualised in figure 3.10, in which can be observed how the photon number distribution spreads out as a function of the TWPA gain.

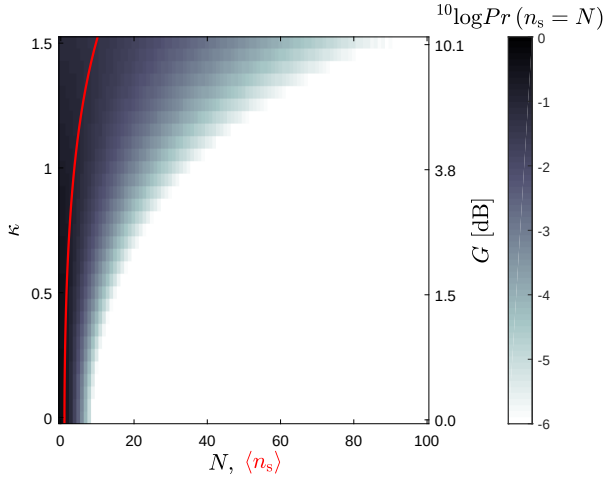
3.5.2 Other implementations

Although it is most trivial to use the TWPA based on Josephson junctions as a non-degenerate amplifier with degenerate pump, there are other implementation schemes, which will be discussed shortly in this section. As in the last section we assume that only the pump(s) is (are) a source of amplification.

- Non-degenerate pump, signal and idler: Instead of feeding the TWPA with a single pump tone, we can apply two pump tones at different frequencies.



(a)



(b)

Figure 3.10: *Photon number distribution in the output state of a TWPA for (a) a single-photon state and (b) a coherent state $\alpha = 1$ as a function of amplification $\kappa = \chi' |A_p|^2 t$ (left axis) or, equivalently, gain G (right axis), assuming $\Delta\Omega = 0$. The colourbar, which is cut off at $Pr < 10^{-6}$, indicates the probability of finding N photons in the output state. The average number of photons in the output state is indicated in red.*

In this case we will find, in first order, three (primary) idler tones, one of which will arise as a result of mixing with the two different pump tones $\omega_{\mathrm{i}} = \omega_{\mathrm{p1}} + \omega_{\mathrm{p2}} - \omega_{\mathrm{s}}$, which has been considered theoretically in [18]. Two other idler tones result from each pump working in a degenerate regime, for which $\omega_{\mathrm{i}(1,2)} = 2\omega_{\mathrm{p}(1,2)} - \omega_{\mathrm{s}}$. However, in turn, each of these idler tones will be the source of (secondary) idler tones at yet different frequencies, such that we end up with a whole spectrum of idlers. A manner to prevent this from happening is to engineer stop bands into the transmission line, such that only specific modes will transmit. However, the generation of many idler tones complicates the analysis for such devices. Still, in general it can be said that such a device will work in the phase-preserving regime.

- Non-degenerate pump, signal only: In case we apply two pump tones at different frequencies, we can engineer a quasi phase-sensitive amplifier, if the signal frequency is chosen at $2\omega_{\mathrm{s}} = \omega_{\mathrm{p1}} + \omega_{\mathrm{p2}}$. It will work only in a quasi phase-sensitive regime, because each pump will also cause a primary idler tone to arise from a phase-preserving interaction with the signal. In turn this gives again rise to a whole set of secondary idler tones. If the transmission line is engineered such, that the primary idlers at $\omega_{\mathrm{i}(1/2)} = 2\omega_{\mathrm{p}(1/2)} - \omega_{\mathrm{s}}$ fall into stop bands, the device will work as a real phase-sensitive device.

- Pump, signal and idler with DC current: If we put the TWPA in between two bias-Ts we can add a DC current to the device. In this manner we can use the device as quasi 3WM, as has been demonstrated in [14]. Adding the current, we should insert $\Phi_{\mathrm{J}} \mapsto \Phi_{\mathrm{J}} + \Phi_{\mathrm{DC}}$ into the Hamiltonian in equation (3.47) which yields, among others, a term proportional to $\hat{\Phi}_{\mathrm{J},0}{}^{3}\Phi_{\mathrm{DC}}$. Continuing the analysis, this yields a term proportional to $\Phi_{\mathrm{DC}}\left(\hat{a}_{\mathrm{p}}\hat{a}_{\mathrm{s}}^{\dagger}\hat{a}_{\mathrm{i}}^{\dagger} + \mathrm{H.c.}\right)$ in the Hamiltonian, which is a 3WM-term. Of course the full Hamiltonian will contain 4WM-terms, since the pump acts as a separate source as well. However, choosing the amplitude of the DC current large with respect to the amplitude of the pump tone, the latter terms can be made small. This implementation of the amplifier is phase-preserving in general, however, it can be used as a phase-sensitive device as well by choosing $\omega_{\mathrm{p}} = 2\omega_{\mathrm{s}}$.

3.6 Paramp terminology – revisited

This chapter started out with an introduction on TWPA terminology. After our extensive excursion into 4WM paramp theory, we have reached the point that we can understand the Hamiltonian in equation (3.4) fully. The only difference between that Hamiltonian and our result in equation (3.58) is that the former uses a co-rotating frame, whereas the latter does not. If we cast equation (3.58)

in a co-rotating frame, we can identify

$$\chi|_{\text{eq.(3.4)}} = \chi|_{\text{eq.(3.55)}} \tag{3.78}$$

$$\Delta\Omega|_{\text{eq.(3.4)}} = (4\xi_{\text{pp}} - \xi_{\text{ps}} - \xi_{\text{pi}})\,\hat{a}_{\text{p}}^{\dagger}\hat{a}_{\text{p}} \tag{3.79}$$

or, in case we absorb a classical pump into the coupling constants

$$\tilde{\chi}|_{\text{eq.(3.5)}} = -\,\chi'|_{\text{eq.(3.63)}}\,|A_{\text{p}}|^2 \tag{3.80}$$

$$\Delta\Omega|_{\text{eq.(3.5)}} = \left(4\xi'_{\text{p}} - \xi'_{\text{s}} - \xi'_{\text{i}}\right)|A_{\text{p}}|^2\,. \tag{3.81}$$

3.7 Marrying the quantum and classical theories

Although the classical theory of the non-linear wave equation and the quantum evolution described by Schrödinger's equation seem to be a world apart, in fact the two descriptions can be mapped onto one another. This will be done in this section.

The marriage between the two theories runs via the Heisenberg equations of motion of the operators and the connection between the classical mode amplitudes on the one hand and creation and annihilation operators on the other. Starting from the Heisenberg equations of motion with a classical undepleted pump and neglecting small terms (cf. equations (3.64) and (3.65))

$$\frac{\partial A_{\text{p}}}{\partial t} = -i\left(\omega_{\text{p}} + 2\xi'_{\text{p}}|A_{\text{p}}|^2\right)A_{\text{p}} \tag{3.82}$$

$$\frac{\partial \hat{a}_{\text{s(i)}}}{\partial t} = -i\left(\omega_{\text{s(i)}} + \xi'_{\text{s(i)}}|A_{\text{p}}|^2\right)\hat{a}_{\text{s(i)}} + i\chi' A_{\text{p}}^2\hat{a}_{\text{i(s)}}^{\dagger}. \tag{3.83}$$

As the classical coupled-mode equations are defined in space, whereas the Heisenberg equations of motion are equations in time, the first step is to change coordinates from time to space, yielding the spatial Heisenberg equations of motion. From equation (3.25) we can infer that $-\omega_n\partial t = k_n\partial z$ by taking both the derivative to time and to space. Therefore,

$$\frac{\partial A_{\text{p}}}{\partial z} = i\left(k_{\text{p}} + 2\frac{k_{\text{p}}\xi'_{\text{p}}}{\omega_{\text{p}}}|A_{\text{p}}|^2\right)A_{\text{p}} \tag{3.84}$$

$$\frac{\partial \hat{a}_{\text{s(i)}}}{\partial z} = i\left(k_{\text{s(i)}} + \frac{k_{\text{s(i)}}\xi'_{\text{s(i)}}}{\omega_{\text{s(i)}}}|A_{\text{p}}|^2\right)\hat{a}_{\text{s(i)}} - i\frac{k_{\text{s(i)}}\chi'}{\omega_{\text{s(i)}}}A_{\text{p}}^2\hat{a}_{\text{i(s)}}^{\dagger}. \tag{3.85}$$

As a last step we change the operators back into the classical amplitudes of the modes by virtue of equation (3.60). By substitution, we arrive at the

classicalised spatial Heisenberg equations of motion

$$\frac{\partial A_{\mathrm{p}}}{\partial z} = i\left(k_{\mathrm{p}} + \Xi^{\mathrm{q}}_{\mathrm{p}}|A_{\mathrm{p}}|^2\right) A_{\mathrm{p}} \tag{3.86}$$

$$\frac{\partial A_{\mathrm{s(i)}}}{\partial z} = i\left(k_{\mathrm{s(i)}} + \Xi^{\mathrm{q}}_{\mathrm{s(i)}}|A_{\mathrm{p}}|^2\right) A_{\mathrm{s(i)}} + iX^{\mathrm{q}}_{\mathrm{s(i)}} A^2_{\mathrm{p}} A^*_{\mathrm{i(s)}}, \tag{3.87}$$

where

$$\Xi^{\mathrm{q}}_n = \frac{k_n \xi'_n}{\omega_n}\left(2 - \delta_{\mathrm{p}n}\right) = \frac{a^4 k^2_{\mathrm{p}} k^3_n \left(2 - \delta_{\mathrm{p}n}\right)}{16 C_{\mathrm{g}} I^2_c L^3_{\mathrm{J},0} \omega^2_n}\left(1 + \Lambda_{\xi_{\mathrm{p}n}}\right) \tag{3.88}$$

$$X^{\mathrm{q}}_{\mathrm{s(i)}} = \frac{k_{\mathrm{s(i)}}\chi'}{\omega_{\mathrm{s(i)}}}\sqrt{\frac{\omega_{\mathrm{i(s)}}}{\omega_{\mathrm{s(i)}}}} = \frac{a^4 k^2_{\mathrm{p}} k_{\mathrm{s}} k_{\mathrm{i}}}{16 C_{\mathrm{g}} I^2_{\mathrm{c}} L^3_{\mathrm{J},0} \omega^2_{\mathrm{s(i)}}}\left(1 + \Lambda_\chi\right). \tag{3.89}$$

This set of equations is identical to equations (3.8) and (3.9) after mapping $A_n \mapsto A_n \mathrm{e}^{ik_n z}$ and removing small terms up to some details: Ξ^{q}_n contains a factor $\left(1 + \Lambda_{\xi_{\mathrm{p}n}}\right)$ which Ξ_n does not. Additionally, the factor $(1 - \Delta k/k_{\mathrm{s(i)}})$ in $X_{\mathrm{s(i)}}$ has been replaced by $(1 + \Lambda_\chi)$ in $X^{\mathrm{q}}_{\mathrm{s(i)}}$. The factor with X_n, however, cannot arise from the quantum theory, since it would need to arise from a coupling constant χ in the Hamiltonian which is somehow different for the signal and idler mode. Such a difference is not permitted by the quantum theory. However, if we would not have neglected the contribution to χ, χ' and thus X^{q}_n due to dispersion, those coupling constants would have been multiplied, up to first order in Δk, by $(1 - i\Delta k l_{\mathrm{q}}/2)$, see equation (3.52). This term resembles the factor $(1 - \Delta k/k_{\mathrm{s(i)}})$ from the classical theory, although it depends on the unphysical quantisation length. Still, the prediction of gain of both the classical coupled-mode equations and the classicalised spatial Heisenberg equations of motion agree well. As can be observed in figure 3.11, in case we do not add dispersion engineering there is hardly a difference in predicted gain, whereas only the maximum gain differs in both approaches in case we add dispersion engineering. This is solely due to the factor $\Delta k/k_{\mathrm{s(i)}}$ in $X_{\mathrm{s(i)}}$.

3.8 Validity

In the presented theory we made several assumptions. Firstly, we only took the first non-linear contribution of the Josephson energy into account and, secondly, it was assumed that the pump can be treated as a classical mode which is undepleted. In this section, the implications of these assumptions will be presented.

The theory presented above is derived from a first-order Taylor expansion of the Josephson energy. This implies that at a certain magnitude of the flux through the junction the theory becomes invalid as higher order terms need to be taken into account. To estimate this flux, we inspect once more the Josephson energy,

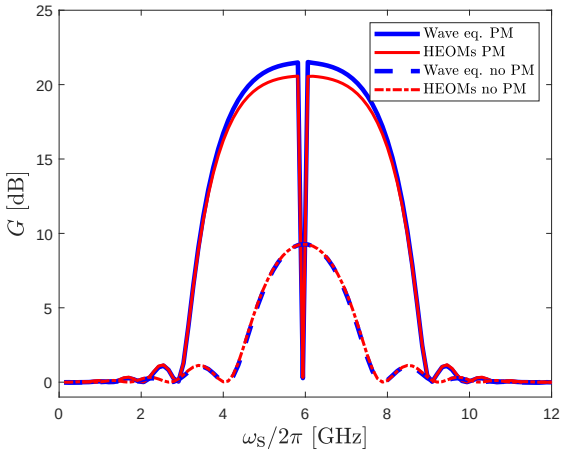


Figure 3.11: *Comparison of the predicted power gain from the coupled-mode equations derived from the classical non-linear wave equation and the classicalised spatial Heisenberg equations of motion from the quantum theory. The comparison is made for the case with and without phase matching using the same parameters as in figure 3.6. The difference in gain with phase matching is due to the $\Delta k/k$-term present in the classical coupled-mode equation coupling constant X_n, but absent in the classicalised spatial Heisenberg equation of motion coupling constant X_n^q.*

$$U_J = I_c\varphi_0\left(1-\cos\left(\frac{\Delta\Phi_J}{\varphi_0}\right)\right) = I_c\varphi_0\sum_{n=1}^{\infty}\frac{(-1)^{n-1}}{(2n)!}\left(\frac{\Delta\Phi_J}{\varphi_0}\right)^{2n}. \tag{3.90}$$

Thus, we find that the second-order ($n=3$) non-linear effects are approximately $4!(\Delta\Phi_{J,p}/\varphi_0)^2/6!$ smaller than the lowest-order non-linear terms. Hence, if we require that the contribution to the energy of the second-order terms is less than 5% of the energy contribution of the first-order terms, we find that our theory breaks down at $\Delta\Phi_{J,p}/\varphi_0 \approx 1.2$ (or $I_p/I_c \approx 0.78$). The dominant second-order amplification term causes two secondary idler modes to appear at $\omega_{(i'),\{i''\}} = 4\omega_p - \omega_{(s),\{i\}}$ implying the general form of the Hamiltonian in equations (3.4) and (3.61) becomes invalid. Moreover, the second-order terms cause additional modulation effects. It is only in the third-order non-linear terms that $(\hat{a}_s^\dagger\hat{a}_i^\dagger)^2$-contributions start to play a role. Furthermore, additional secondary idlers are generated and the modulation effects are further increased. The former terms have an energy contribution approximately $4!(\Delta\Phi_{J,p}/\varphi_0)^2/8! \approx 6\times10^{-4}$ smaller than the first-order non-linear terms at the critical flux ($\Delta\Phi_{J,p}/\varphi_0 = \pi/2$), whereas the latter have an energy contribution of approximately $4!(\Delta\Phi_{J,p}/\varphi_0)^4/8! \approx 4\times10^{-3}$ at the critical flux. Therefore these terms can be neglected for all practical purposes.

The undepleted pump approximation breaks down, if the flux of signal and idler photons in the amplifier becomes close to the flux of pump photons. Typically, this happens when $I_{s,0} \geq I_{p,0}/10$ [14, 18], in which the case the full coupled-mode equations of equations (3.8) and (3.9) need to be considered to calculate the output amplitudes. Alternatively, for the quantum case the full Hamiltonian of equation (3.53) is to be considered to evaluate the evolution of the quantum state.

3.9 Conclusions

After an introduction to the relevant terminology and the classical theory of the coupled-mode equations of Josephson travelling-wave parametric amplifiers, we derived the mesoscopic quantum Hamiltonian up to first non-linear order describing the process using discrete mode operators. We found that such a description is possible, even when taking into account dispersion effects in the transmission line and showed that the classical coupled-mode equations can be derived from this Hamiltonian.
In the derivation, however, there are a few remaining issues. Firstly, it was found that in the non-linear terms of the Hamiltonian, energy and momentum conservation could not be fulfilled simultaneously. Furthermore, the non physical quantisation length is inherent to the theory. The latter can be solved solely under the approximation of a classical undepleted pump. However, the matter can also be resolved in case one derives the Hamiltonian using continuous modes and a transmission line, of which only a part contains the non-linearity. For the concurrent conservation of energy and momentum, we have not been able to find a satisfactory solution.
We found that our Hamiltonian, and therefore the coupled-mode equations, are valid to pump currents up to approximately $0.78I_c$. For larger pump currents more non-linear orders have to be taken into account, for which the same recipe can be followed as shown in this chapter. The same recipe can also be followed to derive the Hamiltonian for TWPAs that have another source of non-linear behaviour, such as kinetic inductance.
To make the theories more applicable to experimental realisations of TWPAs, we suggest that the theories can be expanded by taking into account losses as well as reflections within the device and reflections at the boundaries of the device at which it is coupled to its environment.

Acknowledgements

We would like to thank G. Nienhuis and M.J.A. de Dood for valuable discussions and suggestions. We are grateful to T.H. Oosterkamp for carefully proofreading the manuscript. We also express our gratitude to the Frontiers of Nanoscience programme, supported by the Netherlands Organisation for Scientific Research (NWO/OCW), for financial support.

References

[1] E.W. Bryerton, M. Morgan, and M.W. Pospieszalski. Ultra low noise cryogenic amplifiers for radio astronomy. In *2013 IEEE Radio and Wireless Symposium*, pages 358–360, 2013.

[2] Low noise factory. https://www.lownoisefactory.com. Accessed: Oct. 4, 2018.

[3] Caltech Microwave low noise amplifiers. http://www.caltechmicrowave.org/amplifiers. Accessed: Oct. 4, 2018.

[4] C.M. Caves. Quantum limits on noise in linear amplifiers. *Phys. Rev. D*, 26:1817–1839, 1982.

[5] X. Gu, A.F. Kockum, A. Miranowicz, Y.X. Liu, and F. Nori. Microwave photonics with superconducting quantum circuits. *Phys. Rep.*, pages 1 – 102, 2017.

[6] M.A. Castellanos-Beltran and K.W. Lehnert. Widely tunable parametric amplifier based on a superconducting quantum interference device array resonator. *Appl. Phys. Lett.*, 91:083509, 2007.

[7] N. Bergeal, F. Schackert, M. Metcalfe, R. Vijay, V.E. Manucharyan, L. Frunzio, D.E. Prober, R.J. Schoelkopf, S.M. Girvin, and M.H. Devoret. Analog information processing at the quantum limit with a Josephson ring modulator. *Nature*, 465:64–68, 2010.

[8] N. Roch, E. Flurin, F. Nguyen, P. Morfin, P. Campagne-Ibarcq, M.H. Devoret, and B. Huard. Widely tunable, nondegenerate three-wave mixing microwave device operating near the quantum limit. *Phys. Rev. Lett.*, 108:147701, 2012.

[9] C. Eichler, Y. Salathe, J. Mlynek, S. Schmidt, and A. Wallraff. Quantum-limited amplification and entanglement in coupled nonlinear resonators. *Phys. Rev. Lett.*, 113:110502, 2014.

[10] T. Roy, S. Kundu, M. Chand, A.M. Vadiraj, A. Ranadive, N. Nehra, M.P. Patankar, J. Aumentado, A.A. Clerk, and R. Vijay. Broadband parametric amplification with impedance engineering: Beyond the gain-bandwidth product. *Appl. Phys. Lett.*, 107:262601, 2015.

[11] B. Ho Eom, P.K. Day, H.G. LeDuc, and J. Zmuidzinas. A wideband, low-noise superconducting amplifier with high dynamic range. *Nature Phys.*, 8:623–627, 2012.

[12] T.C. White, J.Y. Mutus, I.-C. Hoi, R. Barends, B. Campbell, Y. Chen, Z. Chen, B. Chiaro, A. Dunsworth, E. Jeffrey, J. Kelly, A. Megrant, C. Neill, P.J.J. O'Malley, P. Roushan, D. Sank, A. Vainsencher, J. Wenner, S. Chaudhuri, J. Gao, and J.M. Martinis. Traveling wave parametric

amplifier with Josephson junctions using minimal resonator phase matching. *Appl. Phys. Lett.*, 106:242601, 2015.

[13] C. Macklin, K. O'Brien, D. Hover, M.E. Schwartz, V. Bolkhovsky, X. Zhang, W.D. Oliver, and I. Siddiqi. A near–quantum-limited Josephson traveling-wave parametric amplifier. *Science*, 350:307–310, 2015.

[14] M.R. Vissers, R.P. Erickson, H.-S. Ku, L. Vale, X. Wu, G.C. Hilton, and D.P. Pappas. Low-noise kinetic inductance traveling-wave amplifier using three-wave mixing. *Appl. Phys. Lett.*, 108:012601, 2016.

[15] A.A. Adamyan, S.E. de Graaf, S.E. Kubatkin, and A.V. Danilov. Superconducting microwave parametric amplifier based on a quasi-fractal slow propagation line. *J. Appl. Phys.*, 119:083901, 2016.

[16] S. Chaudhuri, D. Li, K.D. Irwin, C. Bockstiegel, J. Hubmayr, J.N. Ullom, M.R. Vissers, and J. Gao. Broadband parametric amplifiers based on nonlinear kinetic inductance artificial transmission lines. *Appl. Phys. Lett.*, 110:152601, 2017.

[17] O. Yaakobi, L. Friedland, C. Macklin, and I. Siddiqi. Parametric amplification in Josephson junction embedded transmission lines. *Phys. Rev. B*, 87:144301, 2013.

[18] K. O'Brien, C. Macklin, I. Siddiqi, and X. Zhang. Resonant phase matching of Josephson junction traveling wave parametric amplifiers. *Phys. Rev. Lett.*, 113:157001, 2014.

[19] T.H.A. van der Reep, L. Rademaker, X.G.A. Le Large, R.H. Guis, and T.H. Oosterkamp. An experimental proposal to study spontaneous collapse of the wave function using two travelling-wave parametric amplifiers. *Arxiv*, 1811.01698, 2018.

[20] D. Barral Raña. *Spatial propagation and characterization of quantum states of light in integrated photonic devices.* PhD thesis, Universidade de Santiago de Compostela, 2015.

[21] A.L. Grimsmo and A. Blais. Squeezing and quantum state engineering with Josephson travelling-wave amplifiers. *npj Quantum Inf.*, 3:20, 2017.

[22] J.R. Johansson, P.D. Nation, and F. Nori. Qutip 2: A python framework for the dynamics of open quantum systems. *Comp. Phys. Comm.*, 184:1234–1240, 2013.

[23] J.A. Armstrong, N. Bloembergen, J. Ducuing, and P.S. Pershan. Interactions between light waves in a nonlinear dielectric. *Phys. Rev. A*, 127:1918–1939, 1962.

[24] U. Vool and M. Devoret. Introduction to quantum electromagnetic circuits. *Int. J. Circ. Theor. Appl.*, 45:897–934, 2017.

[25] R. Loudon. *The quantum theory of light.* Oxford University press, 3rd edition, 2000.

[26] S.M. Barnett and P.M. Radmore. *Methods in theoretical quantum optics.* Oxford University press, 1997.

Chapter 4

An experimental proposal to study spontaneous collapse of the wave function using two travelling-wave parametric amplifiers

According to one of the postulates of the Copenhagen interpretation of quantum mechanics, a measurement causes a wave function to collapse into an eigenstate of the measurement apparatus. To study whether such collapses occur spontaneously in an electronic amplifier, we propose an experiment consisting of a microwave interferometer that has a parametric amplifier added to each of its arms. Feeding the interferometer with single photons, we entangle the output of the amplifiers. We calculate the interference visibility as given by standard quantum mechanics as a function of gain, insertion loss and temperature and find a magnitude of 1/3 in the limit of large gain without taking into account losses. This number reduces to 0.26 in case the insertion loss of the amplifiers is 2.2 dB at a temperature of 50 mK. We argue, based on Born's rule that if the process of spontaneous collapse exists, we will measure a reduced visibility compared to the prediction from standard quantum mechanics once this collapse process sets in.

This chapter, authored by T.H.A. van der Reep, L. Rademaker, X.G.A. Le Large, R. Guis and T.H. Oosterkamp, has been submitted for publication.

4.1 Introduction

In the standard Copenhagen interpretation, a 'measurement' amounts to a collapse of the wave function onto one of the eigenstates of the relevant observable. There is, however, no consensus on a microscopic mechanism of such collapse, as it clearly violates the unitary nature of quantum mechanics itself, see e.g. [1] for a review. What all suggested theories of measurement have in common, is the observation that *large* objects are seldom seen in superposition, and that this near-impossibility of large superpositions causes the collapse of a small object (such as an electron, atom or photon) when coupled to a large measurement apparatus.

In other words, measurement can be seen as a process of *amplification*. Consider for example a photon hitting a single-photon detector. A chain of events is set in motion that would lead to an audible click or signal that can be processed by a classical observer. The tiny amount of information contained in that single photon is amplified to human proportions. The question now becomes: at what point of the amplification process did we 'measure' the photon?

In this chapter we propose an experiment to *quantify the amount of amplification required for a wavefunction collapse*. The traditional way of testing whether a superposition has collapsed or not is with an interferometer. The ingredients of our experiment are therefore a single-photon source, used as input to an interferometer, with tuneable amplifiers *inside* the interferometer. If collapse occurs, the visibility of the interference pattern diminishes.

In this chapter we will not argue for one or the other possible mechanisms of the collapse process. The variety of possible ideas is wide, see e.g. [1] for a review. Instead, our proposed experiment only relies on Born's rule. Hence, regardless of one's favourite mechanism, our experiment will provide experimental bounds on the possible size of a quantum object.

In this chapter we present a feasibility study to use such an interferometer to detect quantum collapse. We focus on an implementation of the interferometer using GHz-parametric amplifiers. Such amplifiers have the advantage that their quantum behaviour is well-understood and that they are able to provide large gain [2, 3]. We will cover the conventional quantum optics theory describing the visibility of the interference pattern in terms of quantum mechanical operators. Although this is a straightforward calculation it has not been performed explicitly to our knowledge. We show that the visibility remains measurable as the gain of the amplifiers in the interferometer is increased. Then we will discuss how low the dissipation and temperature of the parametric amplifier must be, such that they do not reduce the visibility to values so close to zero it becomes unmeasurable.

Based on Born's rule, we argue that wave function collapse within a parametric amplifier will alter the interference visibility calculated using the conventional

quantum optics. Therefore, we envision that this experiment may provide a pathway to discern the transition from the quantum to the classical realm, thereby opening the possibility of detecting the collapse of the wave function in a system that can in principle be modelled accurately on a microscopic scale.

In section 4.2 we calculate the Hamiltonian of the interferometer in the lossless case in the time domain. In section 4.3 we introduce a measure for the visibility of our interferometer and we discuss the theoretical predictions for this visibility as a function of the gain of the amplifiers. In section 4.4 we discuss the effect of losses followed by our ideas on observing spontaneous collapse in section 4.5. In the final section we conclude by elaborating on the realisation of the experiment and estimating the feasibility of the experiment with parametric amplifiers with a gain of 40 dB – a gain commonly used to read out quantum bits in quantum computation experiments. Some of the detailed calculations are deferred to the supplementary information.

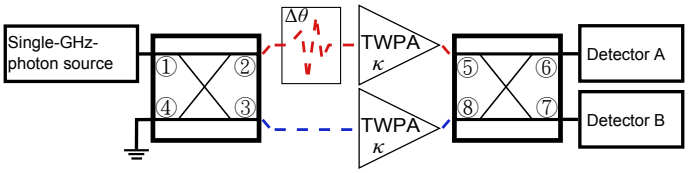


Figure 4.1: *Schematic overview of a balanced microwave amplifier set-up. Using a* $90°$*-hybrid (beam splitter), single photons are brought in a superposition, which is then amplified using two identical TWPAs, characterised by an amplification* κ*. Before entering the TWPAs, the excitation in the upper arm is phase shifted by* $\Delta\theta$*, which is assumed to account for all phase differences within the set-up. Using a second* $90°$*-hybrid, we can study the output radiation from arms* 6 *and* 7 *using detectors A and B.*

4.2 Model – lossless case

We consider the Mach-Zehnder type interferometer depicted in figure 4.1. The interferometer is fed by a single-photon source (signal) in input 1 and a travelling-wave parametric amplifier (TWPA) is added to each of its arms. Although other realisations of the experiment are conceivable, we argue in the supplementary material why we view this version as optimal (see appendices A and B). The signal enters a hybrid (the microwave analogue to a beam splitter), thereby creating a superposition of 0 and 1 photon in each of the arms. The excitation in the upper arm of the interferometer can be phase shifted, where we assume that the phase shift accounts for an intended phase shift as well as all unwanted phase shifts due to fabrication imperfections and the non-linear phase shift from the TWPA. After the TWPA, in which the actual amplification takes place, the excitations from the two arms are brought together using another hybrid and we can study the output radiation with detectors A and B.

In this section we ignore losses, the effect of which we will discuss in section 4.4. We disregard reflections in the set-up as well as a mismatch in amplifier gain. Throughout the chapter we use TWPAs working by a four-wave mixing (4WM) process in a mode which is phase preserving (i.e. the amplification is independent of the pump phase) and non-degenerate (i.e. the pump and the signal are at different frequencies ω_p and ω_s, respectively). We assume the pump to be degenerate (one signal photon is created by destroying two pump photons and by energy conservation this gives rise to an idler at frequency $\omega_\mathrm{i} = 2\omega_\mathrm{p} - \omega_\mathrm{s}$). We also assume that the pump is undepleted (we neglect the decrease of pump photons in the amplification process). Finally, we assume that the pump, signal and idler are phase-matched ($2K_\mathrm{p} = K_\mathrm{s} + K_\mathrm{i}$, where K_n is the wave number including self- and cross-modulation due to the non-linear wave mixing). Under these assumptions [2]

$$\hat{H}_\mathrm{TWPA} = -\hbar\chi \left(\hat{a}_\mathrm{s}^\dagger \hat{a}_\mathrm{i}^\dagger + \mathrm{H.c.}\right). \tag{4.1}$$

Here $\hbar$ is the reduced Planck constant $h/2\pi$ and χ is the non-linear coupling derived from the third-order susceptibility of the transmission line, which takes into account the pump intensity. $\hat{a}_n^\dagger$ is the creation operator of mode n. Using the Heisenberg equations of motion, one can solve for the evolution of the annihilation operators analytically. This yields [2]

$$\hat{a}_{\mathrm{s(i)}}(t) = \hat{a}_{\mathrm{s(i)}}(0)\cosh\kappa + i\hat{a}_{\mathrm{i(s)}}^\dagger(0)\sinh\kappa, \tag{4.2}$$

where $\kappa \equiv \chi\Delta t_\mathrm{TWPA}$ is the amplification if the state spends a time Δt_TWPA in the TWPA. Thus, we can determine the average number of photons in the signal (idler) mode as function of the amplification of the amplifier as

$$\langle\hat{n}_{\mathrm{s(i)}}\rangle_\mathrm{out} = \langle\hat{n}_{\mathrm{s(i)}}\rangle_\mathrm{in}\cosh^2\kappa + \left(\langle\hat{n}_{\mathrm{i(s)}}\rangle_\mathrm{in} + 1\right)\sinh^2\kappa \tag{4.3}$$

provided that the signal and/or idler are initially in a number state. $\langle\hat{n}\rangle_{\mathrm{out(in)}}$ is the average number of photons leaving (entering) the TWPA. From this relation we define the amplifier gain as $G_\mathrm{s} = \langle\hat{n}_\mathrm{s}\rangle_\mathrm{out} / \langle\hat{n}_\mathrm{s}\rangle_\mathrm{in}$.
Even though under these assumptions the calculation can be done analytically (see Appendix C) we present the numerical implementation here, because to such an implementation losses can be added straightforwardly at a later stage.

To numerically obtain the output state we use QuTiP [4]. We first split the Hilbert space of the interferometer into the upper arm and the lower arm. Each of the arm subspaces is additionally divided into a signal and idler subspace. Hence, our numerical Hilbert space has dimension N^4, where $N-1$ is the maximum amount of signal and idler photons taken into account in each of the arms. In this framework the input state is

$$|\psi\rangle = |1\rangle_\mathrm{up,s}|0\rangle_\mathrm{up,i}|0\rangle_\mathrm{low,s}|0\rangle_\mathrm{low,i}, \tag{4.4}$$

where the labels 'up' and 'low' refer to the upper and lower arm of the interferometer respectively. We evolve this state by the time evolution operator,

generated by the Hamiltonian $\hat{H}$ of the system. The first hybrid is described by the Hamiltonian

$$\hat{H}_{\mathrm{h1}} = -\frac{\hbar\pi}{4\Delta t_{\mathrm{h1}}}\left(\sum_{n=\mathrm{s,i}} \hat{a}^{\dagger}_{\mathrm{up},n}\hat{a}_{\mathrm{low},n} + \mathrm{H.c.}\right). \tag{4.5}$$

where Δt_{h1} is the time spent in the hybrid. Note that state evolution with the above Hamiltonian for a time Δt_{h1} corresponds to the transformation operator for an ordinary 90°-hybrid,

$$\hat{U}_{\mathrm{h1}} = \mathrm{e}^{i\hat{H}_{\mathrm{h1}}\Delta t_{\mathrm{h1}}/\hbar} = \mathrm{e}^{i\frac{\pi}{4}\left(\sum_{n=\mathrm{s,i}} \hat{a}^{\dagger}_{\mathrm{up},n}\hat{a}_{\mathrm{low},n} + \mathrm{H.c.}\right)}. \tag{4.6}$$

By the same reasoning, the Hamiltonian of the phase shifter can be written as

$$\hat{H}_{\mathrm{ps}} = \frac{\hbar\Delta\theta}{\Delta t_{\mathrm{ps}}}\left(\sum_{n=\mathrm{s,i}} \hat{a}^{\dagger}_{\mathrm{up},n}\hat{a}_{\mathrm{up},n} + \mathrm{H.c.}\right), \tag{4.7}$$

where $\Delta\theta$ is the applied phase shift. In our numerical calculations we use

$$\hat{H}_{\mathrm{TWPA}}{}^{(\mathrm{up/low})} = -\frac{\hbar\kappa_{(\mathrm{up/low})}}{\Delta t_{\mathrm{TWPA}}}\left(\hat{a}^{\dagger}_{(\mathrm{up/low}),\mathrm{s}}\hat{a}^{\dagger}_{(\mathrm{up/low}),\mathrm{i}} + \mathrm{H.c.}\right) \tag{4.8}$$

for the TWPAs. After the TWPAs, the excitations from the two arms are brought together using a second hybrid to create interference, which is measured with detectors A and B. The second hybrid is described by a Hamiltonian $\hat{H}_{\mathrm{h2}}$ similar to equation (4.5).

To summarise, the proposed theoretical model of the experiment in the absence of losses is as follows. We start with an initial single signal photon in the upper arm, described by equation (4.4). We evolve this state for a time Δt_{h1} with Hamiltonian $\hat{H}_{\mathrm{h1}}$, followed by $\hat{H}_{\mathrm{ps}}$ for a time Δt_{ps}, then for a time Δt_{TWPA} with $\hat{H}_{\mathrm{TWPA}}$ of equation (4.8) and finally for a time Δt_{h2} with Hamiltonian $\hat{H}_{\mathrm{h2}}$. Finally, we will measure the photon densities in detector A and B, which leads to a given visibility of the interference pattern. For the loss-less case the values of the various Δts can be chosen arbitrarily.

4.3 Interference visibility

From the state resulting from our calculations we get the probability distribution of number states in the detectors A and B, $P(\langle n\rangle_{\mathrm{A,s}} = i, \langle n\rangle_{\mathrm{A,i}} = j, \langle n\rangle_{\mathrm{B,s}} = k, \langle n\rangle_{\mathrm{B,i}} = l)$, from which we can calculate the photon number statistics and correlations by performing a partial trace (see appendix D). From the photon number statistics we can compute the visibility of the interference pattern. Although microwave photon counters have been developed in an experimental setting [5–7], we can also envision the measurement of the output radiation

using spectrum analysers. Such instruments measure the output power of the interferometer as a function of time and one can determine the number of photons arriving in the detectors as

$$n = \frac{1}{\hbar\omega}\int_{t_1}^{t_2} P(t)\,\mathrm{d}t'. \tag{4.9}$$

Measuring the average photon number at detectors A and B, we can define the interference visibility as (appendix E)

$$V_{\mathrm{s(i)}} \equiv \left.\frac{\langle n_{\mathrm{B,s(A,i)}}\rangle - \langle n_{\mathrm{A,s(B,i)}}\rangle}{\langle n_{\mathrm{B,s(A,i)}}\rangle + \langle n_{\mathrm{A,s(B,i)}}\rangle}\right|_{\Delta\theta=0}. \tag{4.10}$$

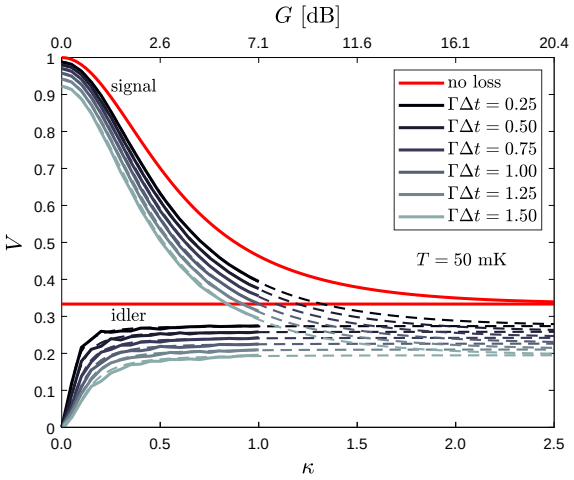
In case the amplifiers have an identical gain, the visibility can also be calculated using a smaller Hilbert space by the following observation: a single TWPA fed with a $|1\rangle_{\mathrm{s}}|0\rangle_{\mathrm{i}}$-input state yields the average number of signal (idler) photons in detector B (A) as calculated with equation (4.3). Contrarily, feeding this TWPA with a $|0\rangle_{\mathrm{s}}|0\rangle_{\mathrm{i}}$-state gives the average number of signal (idler) photons in detector A (B) (see appendix F). This provides a reduced Hilbert space that scales as $2N^2$ for calculating the average visibility. Moreover, this observation implies that the visibility can be computed directly by substitution of equation (4.3) into equation (4.10).
The result is shown in figure 4.2 (in red) and has been verified using our analytical results from Appendix C up to $\kappa = 0.8$ and our numerical results up to $\kappa = 1.7$. It shows that the signal interference visibility drops from 1 to 1/3 with increasing gain due to multiphoton interference, in accordance with [8]. The idler visibility, which can be measured as an additional check on the theoretical predictions made in this chapter and for verification of the interferometer losses (section 4.4), is found to be constant at 1/3 for $\kappa > 0$. For $\kappa = 0$ the idler visibility is undefined.

4.4 The effect of losses

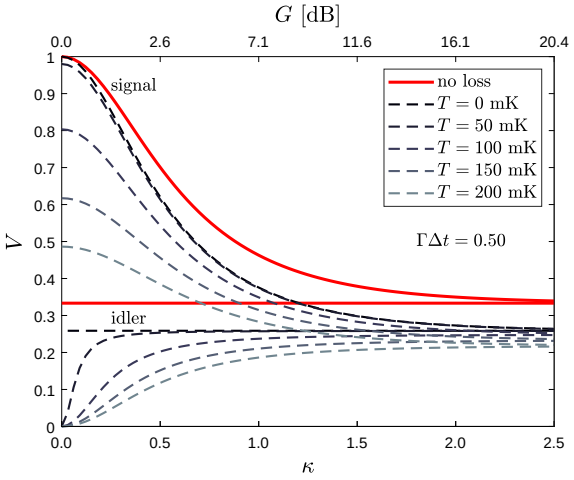
To take into account the effect of losses (dissipation/insertion loss) we use the Lindblad formalism, which provides the expression for the time evolution of the density matrix, $\hat{\rho}$ [9],

$$\frac{\mathrm{d}\hat{\rho}}{\mathrm{d}t} = -\frac{i}{\hbar}[\hat{H},\hat{\rho}] + \sum_{n=1}^{N^2-1}\left(\hat{J}_n\hat{\rho}\hat{J}_n^\dagger - \frac{1}{2}\left\{\hat{\rho},\hat{J}_n^\dagger\hat{J}_n\right\}\right) \tag{4.11}$$

where $\{\,,\}$ denotes the anticommutator and $\hat{J}_n$ are the jump operators. These operators describe transitions that the system may undergo due to interactions with the surrounding thermal bath. Losses can be described by the jump



(a)



(b)

Figure 4.2: *Expected visibility of the interference pattern of the interferometer as a function of amplification κ for signal and idler using the reduced Hilbert space (see text). The gain in dB on the upper axis is only indicative and does not take into account the losses in the amplifiers ($G = 10\log_{10}\langle n_s\rangle_{out}/\langle n_s\rangle_{in} = \cosh\kappa + 2\sinh\kappa$). Without loss (red) the visibility tends to $1/3$ for large gain. The visibility in case losses are added to the system is plotted in grey for various amounts of loss in the TWPAs at (a) $T = 50\,\mathrm{mK}$ ($n_{th} = 8.3\times10^{-3}$) varying $\Gamma\Delta t_{TWPA}$ ($\Gamma = 100\,\mathrm{MHz}$, loss $\approx 4\Gamma\Delta t$ [dB]) and (b) $\Gamma\Delta t_{TWPA} = 0.50$ ($\Gamma = 100\,\mathrm{MHz}$) varying T. For each of the hybrids and the phase shifter the loss is set to $\Gamma\Delta t = 0.1$ and we have set $\omega_{s,i} = 2\pi\times 5\,\mathrm{GHz}$. The reduced Hilbert space calculations are presented in continous lines, whereas an analytical fit and extrapolation according to equation (4.15) is dashed. We find that even TWPA losses as high as 6 dB do not reduce the visibility to 0.*

operators $\hat{J}_{\text{out}}$ and $\hat{J}_{\text{in}}$. $\hat{J}_{\text{out}}$ describes a photon leaving the system and entering the bath,

$$\hat{J}_{\text{out},n} = \sqrt{\Gamma\,(1+n_{\text{th}})}\hat{a}_n, \tag{4.12}$$

where Γ is the loss rate and $n_{\text{th}} = 1/(\exp(\hbar\omega/k_{\text{B}}T)-1)$ is the thermal occupation number of photons in the bath. $\hat{J}_{\text{in}}$ describes a photon entering the system from the bath,

$$\hat{J}_{\text{in},n} = \sqrt{\Gamma n_{\text{th}}}\hat{a}_n^\dagger. \tag{4.13}$$

Here we again see the advantage of using a description in the time domain and putting Δt in the component Hamiltonians, equations (4.5), (4.7) and (4.8) in section 4.2. The total (specified) loss is mainly determined by the product $\Gamma\Delta t$ relating to the (insertion) loss as

$$\begin{aligned} IL &= -10\log_{10}\left((1-n_{\text{th}}/\langle n_{\text{in}}\rangle)\,\mathrm{e}^{-\Gamma\Delta t} + n_{\text{th}}/\langle n_{\text{in}}\rangle\right) \\ &\approx 4\Gamma\Delta t. \end{aligned} \tag{4.14}$$

The approximation holds for n_{th} small. This allows us to define a constant loss rate for the whole set-up, while adjusting Δt for each component to match the actual loss. Since the photon state in the interferometer is now described by a density matrix, the amount of memory for these calculations scales as N^8.

To study the effect, we set $\omega_{\text{s,i}} = 2\pi \times 5\,\text{GHz}$ for now. The loss rate Γ is set to 100 MHz for the full set-up. For the hybrids and the phase shifter, we choose $\Delta t_{(\text{h}_1,\text{ps},\text{h}_2)} = 1\,\text{ns}$ ($IL \approx 0.4\,\text{dB}$) and study the effect of losses in the TWPAs by varying Δt_{TWPA} and T. We evolve the state under the Hamiltonians $\hat{H}_{\text{h}_1} \to \hat{H}_{\text{ps}} \to \hat{H}_{\text{TWPA}}{}^{(\text{up/low})} \to \hat{H}_{\text{h}_2}$ as described in section 4.2.
Unfortunately, running the numeric calculation, we were not able to increase the amplification to $\kappa > 0.6$ due to QuTip working with a version of SciPy supporting only int32 for element indexing. However, again it appears that we can use the method of the reduced Hilbert space sketched in the last section. Thus, the problem only scales as $2N^4$, and we have performed the numeric calculation up to $\kappa = 1.0$.
Applying the reduced Hilbert space approach, we found that the parametric amplifier's output in presence of losses can be fitted according to

$$\langle\hat{n}_{\text{s(i)}}\rangle_{\text{out}} = \langle\hat{n}_{\text{s(i)}}\rangle_{\text{out}}|_{\kappa=0}\cosh^2\kappa + \left(\langle\hat{n}_{\text{i(s)}}\rangle_{\text{out}}|_{\kappa=0} + 1\right)\mathrm{e}^{-f}\sinh^2\kappa \tag{4.15}$$

where the fitting parameter f depends on Γ, the various Δts (if $T > 0$), n_{th} and the input state (see Appendix G). $\langle\hat{n}_{\text{s(i)}}\rangle_{\text{out}}|_{\kappa=0}$ is the number of photons leaving the amplifier in case no amplification is present,

$$\langle\hat{n}_{\text{s(i)}}\rangle_{\text{out}}|_{\kappa=0} = \left(\langle\hat{n}_{\text{s(i)}}\rangle_{\text{in}} - n_{\text{th}}\right)\mathrm{e}^{-\Gamma\Delta t_{\text{tot}}} + n_{\text{th}}. \tag{4.16}$$

This allows us to extrapolate the results to higher gain.

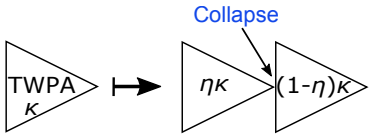


Figure 4.4: *Model of a TWPA in which a quantum state collapse takes place. The quantum TWPA, characterised by coupling constant κ is split in two parts. One is characterised by the coupling constant $\eta\kappa$ and the other by $(1-\eta)\,\kappa$, where $\eta \in [0,1]$ determines the position of the collapse. We assume that the state collapse takes place instantaneously between the two parts of the amplifier.*

The results of the calculations with loss are also depicted in figure 4.2 assuming the full set-up is at a constant temperature. Some plots of the visibility as function of loss for given κ are depicted in figure 4.11 in appendix F. In figure 4.2 we observe that losses decrease the interference visibility with respect to the case where losses were neglected. However, even for TWPA losses as high as 6 dB the interference visibility survives. As in the no-loss case the signal and idler visibility converge asymptotically to the same value.

4.5 Observing spontaneous collapse

Although there is currently no universally agreed-upon model that describes state collapse, we propose to mathematically investigate the effect of collapse on the proposed experiment using Born's rule in the following way.
To model the collapse we split each of the amplifiers in the upper and lower arm of the interferometer in two parts and we assume that the collapse takes place instantaneously in between these two parts, see figure 4.4. Thus, the first part of each amplifier can be characterised by a coupling constant $\eta\kappa$ and the second by a coupling constant $(1-\eta)\,\kappa$, where $\eta \in [0,1]$ sets the collapse position. If $\eta = 0$ the collapse takes place between the first hybrid and the amplifiers, while for $\eta = 1$ the collapse takes place between the amplifiers and the second hybrid. For $0 < \eta < 1$ the collapse takes place within the amplifiers. For simplicity, we ignore the fact that a photon is a spatially extended object.
Furthermore, by Born's rule we have to assume a collapse phenomenology. Regardless of the precise mechanism, such a collapse will destroy the entanglement between the two interferometer arms and yield a classical state. As for the type of classical state, we will consider two options: the state collapses onto (1) a number state, or (2) onto a coherent state. For both these options we will study the effect on the interference visibility below.

4.5.1 Collapse onto a number state

In case the collapse projects the instantaneous state onto a number state, the state after projection is given by $|\psi_{\text{coll}}\rangle(N,M) = |N+1\rangle_{\text{up,s}}|N\rangle_{\text{up,i}}|M\rangle_{\text{low,s}}|M\rangle_{\text{low,i}}$

or $|\psi_{\text{coll}}\rangle(N,M)=|N\rangle_{\text{up,s}}|N\rangle_{\text{up,i}}|M+1\rangle_{\text{low,s}}|M\rangle_{\text{low,i}}$, depending on whether the initial photon went through the upper or lower arm of the interferometer. Hence, this collapse phenomenology can be thought of as resulting from the collapse taking place as a consequence of a which-path detection or the consequence of a spontaneous collapse onto a number state due to some unknown mechanism. The second part of the amplifiers, characterised by the coupling constant $(1-\eta)\,\kappa$, evolves $|\psi_{\text{coll}}\rangle$ to $|\psi'_{\text{coll}}\rangle=\sum_{N,M}c_{NM}\,|\psi_{\text{coll}}\rangle\,(N,M)$, where c_{NM} are the weights determined by $(1-\eta)\,\kappa$ and $\sum_{N,M}|c_{NM}|^2=1$. $|\psi'_{\text{coll}}\rangle$ is the state just before the second hybrid.

To determine the effect on the interference visibility of such a collapse, we calculate $\langle n\rangle_{X,n}=\hat{a}^{\dagger}_{X,\,n}\hat{a}_{X,\,n}$, the number of photons arriving in detector $X\in\{\text{A,B}\}$ in mode $n\in\{\text{s,i}\}$. This equation can be rewritten in terms of creation and annihilation operators of the upper and lower arm of the interferometer by the standard hybrid transformation relations $\hat{a}_{[\text{A}]\{\text{B}\},n}\mapsto(\{1\}[i]\hat{a}_{\text{up},n}+\{i\}[1]\hat{a}_{\text{low},n})/\sqrt{2}$ to find

$$V_n^{\text{coll}}=\frac{i\,\langle\hat{a}^{\dagger}_{\text{up},n}\hat{a}_{\text{low},n}-\hat{a}_{\text{up},n}\hat{a}^{\dagger}_{\text{low},n}\rangle}{\langle\hat{a}^{\dagger}_{\text{up},n}\hat{a}_{\text{up},n}+\hat{a}^{\dagger}_{\text{low},n}\hat{a}_{\text{low},n}\rangle},\tag{4.17}$$

which equals 0 for any $|\psi'_{\text{coll}}\rangle$. Hence, we find that a collapse onto a number state within the interferometer causes a total loss of interference visibility.

4.5.2 Collapse onto a coherent state

If the collapse projects the quantum state onto a coherent state, the state after collapse is $|\psi_{\text{coll}}\rangle=|\alpha_{\text{up,s}}\rangle\,|\alpha_{\text{up,i}}\rangle\,|\alpha_{\text{low,s}}\rangle\,|\alpha_{\text{low,i}}\rangle$ with overlap $c_{\text{coll}}=\langle\psi_{\text{coll}}|\psi_{\text{q}}\rangle$. Here $|\psi_{\text{q}}\rangle$ is the instantaneous quantum state at the moment of collapse. This collapse phenomenology can be thought of as the electrons in the transmission lines connecting the different parts of the interferometer collapsing into position states.
In this case, the second part of the parametric amplifiers characterised by $(1-\eta)\,\kappa$ evolves the amplitudes α in $|\psi_{\text{coll}}\rangle$ into average amplitudes

$$\bar{\alpha}_{\text{up(low),s(i)}}=\alpha_{\text{up(low),s(i)}}\cosh(1-\eta)\,\kappa+i\alpha^{*}_{\text{up(low),i(s)}}\sinh(1-\eta)\,\kappa\tag{4.18}$$

by equation (4.2). Then the number of photons arriving in each detector is, for each individual collapse,

$$n^{\text{coll}}_{\text{A(B)},n}=\frac{1}{2}\left(|\bar{\alpha}_{\text{up},n}|^2+|\bar{\alpha}_{\text{low},n}|^2\mp\,2|\bar{\alpha}_{\text{up},n}||\bar{\alpha}_{\text{low},n}|\sin(\phi_{\text{low},n}-\phi_{\text{up},n})\right)\tag{4.19}$$

where ϕ_i is the phase of the state $\bar{\alpha}_i$. Thus, we can obtain the average number of photons arriving in each detector as an integration over all possible collapsed

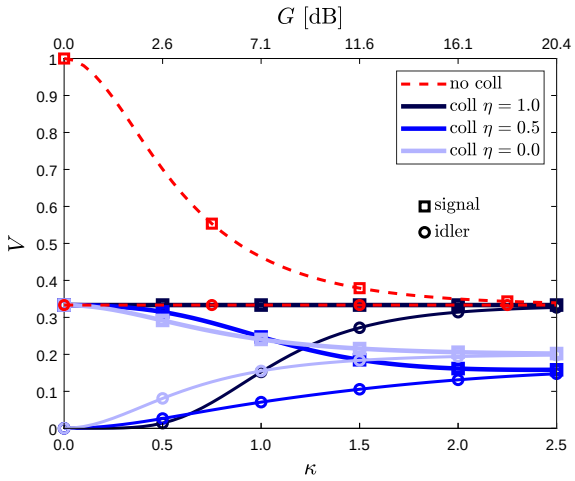


Figure 4.5: *Comparison of the interference visibility resulting from a full quantum calculation without collapse and under the assumption of state collapse to coherent states within the interferometer assuming no losses. If the state collapses between the amplifiers and the second hybrid ($\eta = 1$), the visibility is $1/3$ for the signal and rises to $1/3$ with increasing amplification for the idler. In case the collapse takes place halfway through the amplifiers ($\eta = 0.5$), the visibility tends to 0.15 for both signal and idler for high gain and if the collapse is between the first hybrid and the amplifiers ($\eta = 0$), the visibility goes to 0.2 for signal and idler.*

states weighed by their probability. That is

$$\langle n_{X,n}^{\text{coll}} \rangle = \frac{1}{\pi^4} \int n_{X,n}^{\text{coll}} |c_{\text{coll}}|^2 \, \mathrm{d}^2\alpha_{\text{up,s}} \mathrm{d}^2\alpha_{\text{up,i}} \mathrm{d}^2\alpha_{\text{low,s}} \mathrm{d}^2\alpha_{\text{low,i}} \tag{4.20}$$

in which $\mathrm{d}^2\alpha_n$ denotes the integration over the complex amplitude of the coherent state n. Then, we determine the interference visibility according to equation (4.10).

In case we assume that the interferometer is lossless, we can perform such a calculation analytically (see appendix H). The resulting interference visibility is plotted in figure 4.5 in which we can observe that the interference visibility at high gain depends on the location of collapse. For $\eta = 1$ the signal and idler visibility equals $1/3$. For $\eta = 0.5$ both visibilities tend to 0.15 at high gain and in case $\eta = 0$ the visibility tends to 0.2 for both signal and idler.

4.6 Experimental realisation and feasibility

As a single-photon source, we propose to use a qubit capacitively coupled to a microwave resonator [10]. For the amplifiers we can use TWPAs in which the non-linearity is provided by Josephson junctions. Currently, TWPAs providing

20 dB ($\kappa = 2.5$) of gain and 2 dB of (insertion) loss that operate at $T = 30$ mK have been developed [3].

The amplification process within the TWPAs is driven by a coherent pump signal. Instead of increasing the gain of the TWPAs by increasing the pump power, we propose to vary the amplification by varying the pump frequency. In the latter method the amplification varies due to phase-matching conditions within the amplifier. The advantage is that in this manner the transmission and reflection coefficients of the TWPA, which depend on the pump power [11], can be kept constant while varying the gain in the interferometer. Although we assumed perfect phase matching in the amplifiers for the results shown in this chapter, we do not expect a large difference if one changes from a varying pump-power approach to a varying phase-matching approach.

Our calculations are based on a Taylor expansion up to the third-order susceptibility of a parametric amplifier. Typically, microwave TWPAs work close to the critical current of the device, such that this assumption might break down and we need to take into account higher orders as well. For TWPAs based on Josephson junctions, we can estimate as follows at which current a higher order Taylor expansion would become necessary.
In the Hamiltonian of a TWPA with Josephson junctions the non-linearity providing wave mixing arises from the Josephson energy

$$E_{\mathrm{J}} = I_{\mathrm{c}}\varphi_0 \left(1 - \cos\left(\frac{\Phi}{\varphi_0}\right)\right) = I_{\mathrm{c}}\varphi_0 \sum_{n=1}^{\infty} \frac{(-1)^{n-1}}{(2n)!} \left(\frac{\Phi}{\varphi_0}\right)^{2n}. \tag{4.21}$$

Here, I_{c} is the junction's critical current and φ_0 is the reduced flux quantum $\Phi_0/2\pi$. Hence, the second-order ($n = 3$) non-linear effects have a factor $4!(\Phi_{\mathrm{p}}/\varphi_0)^2/6!$ smaller contribution than the first-order non-linear effects. This contribution causes the generation of secondary idlers and additional modulation effects. If we require that this contribution is less than 5% of the energy contribution of the first-order non-linear terms, we can estimate that the theory breaks down at $\Phi_{\mathrm{p}}/\varphi_0 \approx 1.2$ ($I_{\mathrm{p}}/I_{\mathrm{c}} \approx 0.78$). It is only in the third-order non-linearity that terms proportional to $(\hat{a}_{\mathrm{s}}^{\dagger}\hat{a}_{\mathrm{i}}^{\dagger})^n$ with $n > 1$ start to appear, apart from yet additional secondary idlers and further modulation effects. These terms have a maximal contribution of approximately $4!(\Phi_{\mathrm{p}}/\varphi_0)^4/8! \approx 4 \times 10^{-3}$ smaller than the first-order non-linear term at the critical flux ($\Phi_{\mathrm{p}}/\varphi_0 = \pi/2$) and are therefore negligible for practical purposes.

The other assumption that might break down is the assumption of an undepleted pump. If the signal power becomes too close to the pump power, the pump becomes depleted. Typically this happens at $P_{\mathrm{s}} \approx P_{\mathrm{p}}/100$ [11]. At $I_{\mathrm{p}}/I_{\mathrm{c}} = 0.9$, $P_{\mathrm{p}} \approx 1$ nW in a 50 Ω-transmission line with $I_{\mathrm{c}} = 5\,\mu$A. In case our qubit photon source has a T_1-time of approximately 100 ns [10], implying the photon has a duration in that order, the number of 5 GHz-pump photons available for amplification is in the order of 10^7. Hence, we expect that pump depletion only starts to play a significant role in case the amplification becomes about 50 dB.

In our calculations the only loss-effect that was not taken into account was the loss of pump photons due to the insertion loss of the TWPA. If the insertion loss amounts to 3 dB, half of the pump photons entering the device will be dissipated. To our knowledge, this effect has not been considered in literature. However, effectively this must lead to a non-linear coupling constant χ (equation (4.1)), which decreases in magnitude in time. In a more involved calculation this effect needs to be taken into account for a better prediction of the experimental outcome of the visibility.
Apart from making χ time-dependent, the loss of pump photons will be the main reason for an increase of temperature of the amplifiers. A dilution refrigerator is typically able to reach temperatures of 10 mK with a cooling power of 1 μW. The heat conductivity of the transmission line to the cold plate of the refrigerator will limit the temperature of the TWPA. Still, we estimate that a dissipation in the order of 0.5 nW will not heat up the amplifiers above 50 mK. However, as shown in figure 4.2, even if the amplifiers heat up to temperatures as large as 200 mK we still expect a visibility that should be easily measurable, if no collapse would occur.
Finally, a more accurate calculation of the expected interference visibility would need to take into account reflections within the set-up as well as the possible difference in gain between both amplifiers and other present decoherence mechanisms, which we have not considered here.

The results we obtained for the interference visibility with a collapse within the interferometer are only speculative as the mechanism of state collapse is currently not understood. In case the state collapses onto a number state, the resulting interference visibility is 0 for any gain. We anticipate that this number might increase in case losses are taken into account in the calculation, however, still we expect that the difference in interference visibility between the cases of no collapse and collapse within the interferometer should be easily detectable. Contrarily, if the state collapses onto a coherent state, the visibility depends on the location of the collapse. This result should be interpreted as follows. Let us assume that the state collapses at a gain of 20 dB ($\kappa = 2.5$). Then, neglecting losses, the predicted signal interference visibility is approximately $1/3$ in case the state does not collapse, whereas it equals $1/3$ in the case the state collapses between the amplifiers and the second hybrid ($\eta = 1$). However, if we increase the gain further, the expected location of collapse (the location at which the state is amplified by 20 dB) moves towards the first hybrid ($\eta < 1$), which will become apparent in the measurement result as an initial gradual drop in the interference visibility followed by an increase, see figure 4.5. Simultaneously, the idler visibility is expected to show the same behaviour.
It should be noted that the result for a calculation, in which one assumes a state collapse onto a coherent state between the interferometer and the detectors, is the same as when the state would collapse between the amplifiers and the second hybrid of the interferometer. However, even if this would be the case, one can observe a collapse within the interferometer if the collapse takes place

within the amplifiers. A second remark to this collapse phenomenology is that it does not conserve energy. If one considers some state $|\psi\rangle$ with an average photon number n, one finds that a collapse onto a coherent state adds one noise photon to the state. Such an increase in energy is a property of many spontaneous collapse models [12–16]. It is due to this added photon and its amplification in the classical part of the TWPAs that the differences in the predicted interference visibility with and without state collapse arise.
In case one assumes a collapse onto a coherent state one could calculate the expected interference visibility in case losses are included numerically by calculating the overlap between the state evolved until collapse and many (order 10^6) randomly chosen coherent states. However, due to the issue with Scipy noted in section 4.4, we could not perform this calculation for a reasonable number of photons. Still we expect that, although the difference in visibility between the situations with and without collapse in the interferometer might be decreased, this difference is measurable.

Under these considerations, an experiment with two 40 dB amplifiers ($\kappa = 4.7$) at 50 mK, which might be developed if losses are reduced, is feasible.

4.7 Conclusions

We conclude that it should be possible to determine whether or not a 40 dB-parametric amplifier causes a wave function to collapse. If we insert such an amplifier into each of the two arms of an interferometer, we can measure the visibility of the output radiation. Neglecting losses the interference visibility of both signal and idler tend to 1/3 with increasing gain, in case no collapse takes place. If the state collapses onto a number state within the interferometer, the visibility reduces to 0, whereas we found a significant deviation from 1/3 in the case that the state collapses onto a coherent state. In case the insertion loss of the amplifiers is 2.2 dB, while the temperature of the devices is 50 mK, we estimate an interference visibility of 0.26. In case wave function collapse sets in, we still expect the visibility to decrease measurably.

Acknowledgements

We would like to thank M.J.A. de Dood for fruitful discussions and C.W.J. Beenakker for the use of the computer cluster. We thank M. de Wit for proofreading this manuscript. We also express our gratitude to the Frontiers of Nanoscience programme, supported by the Netherlands Organisation for Scientific Research (NWO/OCW), for financial support.

References

[1] A. Bassi, K. Lochan, S. Satin, T. P. Singh, and H. Ulbricht. Models of wave-function collapse, underlying theories, and experimental tests. *Rev. Mod. Phys.*, 85:471–527, 2013.

[2] W. H. Louisell, A. Yariv, and A. E. Siegman. Quantum fluctuations and noise in parametric processes. i. *Phys. Rev.*, 124:1646–1654, 1961.

[3] C. Macklin, K. O'Brien, D. Hover, M. E. Schwartz, V. Bolkhovsky, X. Zhang, W. D. Oliver, and I. Siddiqi. A near–quantum-limited josephson traveling-wave parametric amplifier. *Science*, 2015.

[4] J. R. Johansson, P. D. Nation, and F. Nori. Qutip 2: A python framework for the dynamics of open quantum systems. *Comp. Phys. Comm.*, 184:1234–1240, 2013.

[5] D. I. Schuster, A. A. Houck, J. A. Schreier, A. Wallraff, J. M. Gambetta, A. Blais, L. Frunzio, J. Majer, B. Johnson, M. H. Devoret, S. M. Girvin, and R. J. Schoelkopf. Resolving photon number states in a superconducting circuit. *Nature*, 445:515–518, 2007.

[6] Y.-F. Chen, D. Hover, S. Sendelbach, L. Maurer, S. T. Merkel, E. J. Pritchett, F. K. Wilhelm, and R. McDermott. Microwave photon counter based on josephson junctions. *Phys. Rev. Lett.*, 107:217401, 2011.

[7] K. Inomata, Z. Lin, K. Koshino, W. D. Oliver, J.-S. Tsai, T. Yamamoto, and Y. Nakamura. Single microwave-photon detector using an artificial λ-type three-level system. *Nat. Commun.*, page 12303, 2016.

[8] L. Rademaker, T. van der Reep, N. Van den Broeck, B. van Waarde, M. de Voogd, and T. Oosterkamp. The instability of a quantum superposition of time dilations.

[9] H. P. Breuer and F. Petruccione. *The theory of open quantum systems.* Oxford Univ. Press, 2002.

[10] A. A. Houck, D. I. Schuster, J. M. Gambetta, J. A. Schreier, B. R. Johnson, J. M. Chow, L. Frunzio, J. Majer, M. H. Devoret, S. M. Girvin, and R. J. Schoelkopf. Generating single microwave photons in a circuit. *Nature*, 449:328–331, 2007.

[11] K. O'Brien, C. Macklin, I. Siddiqi, and X. Zhang. Resonant phase matching of josephson junction traveling wave parametric amplifiers. *Phys. Rev. Lett.*, 113:157001, 2014.

[12] M. Bahrami, M. Paternostro, A. Bassi, and H. Ulbricht. Proposal for a noninterferometric test of collapse models in optomechanical systems. *Phys. Rev. Lett.*, 112:210404, 2014.

[13] S. Nimmrichter, K. Hornberger, and K. Hammerer. Optomechanical sensing of spontaneous wave-function collapse. *Phys. Rev. Lett.*, 113:020405, 2014.

[14] L. Diósi. Testing spontaneous wave-function collapse models on classical mechanical oscillators. *Phys. Rev. Lett.*, 114:050403, 2015.

[15] A. Vinante, M. Bahrami, A. Bassi, O. Usenko, G. Wijts, and T. H. Oosterkamp. Upper bounds on spontaneous wave-function collapse models using millikelvin-cooled nanocantilevers. *Phys. Rev. Lett.*, 116:090402, 2016.

[16] A. Vinante, R. Mezzena, P. Falferi, M. Carlesso, and A. Bassi. Improved noninterferometric test of collapse models using ultracold cantilevers. *Phys. Rev. Lett.*, 119:110401, 2017.

[17] M. A. Castellanos-Beltran and K. W. Lehnert. Widely tunable parametric amplifier based on a superconducting quantum interference device array resonator. *Appl. Phys. Lett.*, 91:083509, 2007.

[18] S. M. Barnett and P. M. Radmore. *Methods in theoretical quantum optics.* Oxford University press, 2002.

Appendices

A Experimental realisation using resonator based parametric amplifiers

The discussed set-up is not the only conceivable realisation of the experiment. Instead of using a TWPA, it is also possible to use a resonator-based parametric amplifier, such as the Josephson parametric amplifier (JPA), if the bandwidth of the photons is smaller than the bandwidth of the amplifier. TWPAs are broadband ($BW \approx 5$GHz [3]), whereas JPAs are intrinsically limited in their bandwidth ($BW \approx 10$MHz [17]). However, both amplifiers are suitable to amplify a single photon with a 1 MHz-bandwidth, in case our photon source would have a T_1-time in excess of 1 μs.

As we want to minimise losses and reflections in the interferometer arms, using

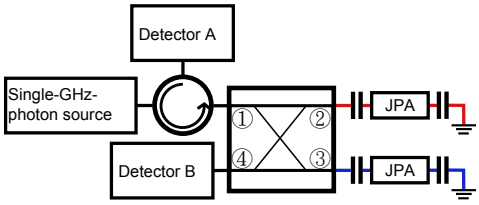


Figure 4.6: *Schematic overview of the implementation of the experiment using JPAs. In this case it is beneficial to use a Michelson type interferometer to minimise losses.*

a TWPA leads to a Mach-Zehnder type interferometer, whereas using a JPA results in a Michelson type interferometer, see figure 4.6. In case the JPA works in the non-degenerate regime ($\omega_s \neq \omega_i$), the results of the interference visibility as presented in this paper are the same.

B Non-degenerate vs. degenerate amplifiers

In the main text we considered the amplifiers to be non-degenerate, i.e. $\omega_s \neq \omega_i$. In case the amplifiers work in a degenerate regime,

$$\hat{H}_{\text{deg}} = -\hbar\chi \left(\hat{a}_s^\dagger \hat{a}_s^\dagger e^{i\Delta\phi} + \text{H.c.}\right) \tag{4.22}$$

and the amplification will be dependent on the relative phase, $\Delta\phi$, between the signal and the pump, see figure 4.7. In this case we can still measure a visibility – in fact, $\Delta\phi$ can be used as a phase shifter in the experiment – as can be observed in figure 4.8. In this figure, the expected interference visibility in case the quantum state does not collapse within the interferometer is depicted using continuous lines. In case we assume that the state collapses into a coherent state in between the amplifiers and the second hybrid, the resulting visibility can be calculated using the method outlined in section 4.5 and appendix H. The result is depicted in figure 4.8 using dashed lines. It is observed that for

large amplification κ the two results approach each other asymptotically.
The main advantage of using non-degenerate instead of degenerate amplifiers is that the latter have not been developed. In the microwave regime, parametric amplifiers have been developed using Josephson junctions and kinetic inductance as the source of non-linear wave mixing and the resulting amplification. Both these sources lead naturally to non-degenerate devices as the non-linearity scales quadratically with pump current. One can use these as quasi-degenerate amplifiers by, e.g., biasing the device using a DC-current. This complicates the set-ups as proposed in figures 4.1 and 4.6, which can be a source of reflections and decoherence. Moreover, such amplifiers will always have non-degenerate contributions to their amplification, which complicates the analysis of the experiment. Thirdly, non-degenerate amplifiers enable one to study two interference visibilities (of both signal and idler) instead of one. For these reasons, we consider non-degenerate amplifiers to be more suited for our proposed experiment.

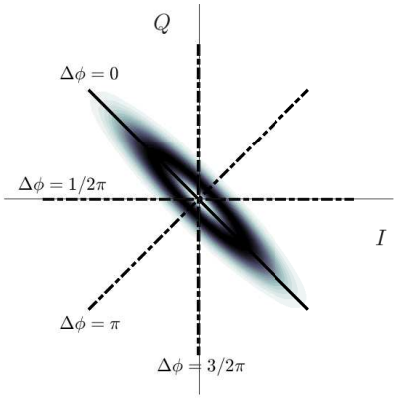


Figure 4.7: *Wigner function of the state entering the hybrid after amplification by a degenerate amplifier (equation (4.22)). Depicted is the case where the signal and pump are in phase ($\Delta\phi = 0$). If $\Delta\phi \neq 0$ the Wigner function rotates according to the dash-dotted lines.*

C Analytical model

Without losses and using the assumptions for the TWPAs as presented in section 4.2, we can obtain an analytical model for the output state. We start by creating a single signal photon in input channel 1.

$$|\psi\rangle_1 = \hat{a}^\dagger_{1\mathrm{s}} |0_{1\mathrm{s}}, 0_{1\mathrm{i}}, 0_{4\mathrm{s}}, 0_{4\mathrm{s}}\rangle = |1_{1\mathrm{s}}, 0_{1\mathrm{i}}, 0_{4\mathrm{s}}, 0_{4\mathrm{s}}\rangle \tag{4.23}$$

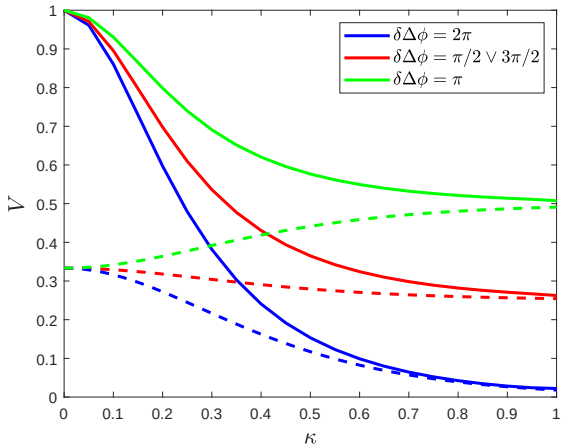


Figure 4.8: *Interference visibility of the experiment implementing degenerate parametric amplifiers as function of amplification $\kappa = \chi\Delta t_{deg}$ and the difference in relative phase of the two amplifiers, $\delta\Delta\phi = \Delta\phi_{up} - \Delta\phi_{low}$. $\delta\Delta\phi$ can effectively be used as a phase shifter and we assume the interferometer to be lossless. The continous lines represent the visibility resulting from a quantum calculation. The dashed lines result from a calculation in which we assume state collapse into coherent states between the amplifiers and the second hybrid ($\eta = 1$, see section 4.5 and appendix H).*

Here, $\hat{a}^\dagger$ is the creation operator working on the vacuum. We then incorporate the 90°-hybrid by making the transformation

$$\hat{a}^\dagger_{1\mathrm{s}} \mapsto \frac{1}{\sqrt{2}}\left(i\hat{a}^\dagger_{2\mathrm{s}} + \hat{a}^\dagger_{3\mathrm{s}}\right). \tag{4.24}$$

Next, a phase shift $\Delta\theta$ is applied to the upper arm,

$$\hat{a}^\dagger_{2\mathrm{s}} \mapsto \hat{a}^\dagger_{2\mathrm{s}} \mathrm{e}^{i\theta\hat{a}^\dagger_{2\mathrm{s}}\hat{a}_{2\mathrm{s}}} \tag{4.25}$$

at which the state just before the TWPAs is

$$|\psi\rangle_2 = \frac{1}{\sqrt{2}}\left(i\mathrm{e}^{i\Delta\theta\hat{a}^\dagger_{2\mathrm{s}}\hat{a}_{2\mathrm{s}}}\hat{a}^\dagger_{2\mathrm{s}} + \hat{a}^\dagger_{3\mathrm{s}}\right)|0_{2\mathrm{s}}, 0_{2\mathrm{i}}, 0_{3\mathrm{s}}0_{3\mathrm{s}}\rangle \tag{4.26}$$

$$= \frac{1}{\sqrt{2}}\left(i\mathrm{e}^{i\Delta\theta}|1_{2\mathrm{s}}, 0_{2\mathrm{i}}, 0_{3\mathrm{s}}0_{3\mathrm{s}}\rangle + |0_{2\mathrm{s}}, 0_{2\mathrm{i}}, 1_{3\mathrm{s}}0_{3\mathrm{s}}\rangle\right). \tag{4.27}$$

For the TWPAs we use the following Hamiltonian in the interaction picture

$$\hat{H}_{\mathrm{TWPA}}{}^{\mathrm{eff}} = -\hbar\chi\left(\hat{a}^\dagger_{\mathrm{s}}\hat{a}^\dagger_{\mathrm{i}} + \mathrm{H.c.}\right). \tag{4.28}$$

Evolving the state under this Hamiltonian as $|\psi\rangle_3 = \mathrm{e}^{-i\,\hat{H}_{\mathrm{TWPA}}{}^{\mathrm{eff}}t/\hbar}$, the output

for a single amplifier in a single arm is (cf. [18])

$$\mathrm{e}^{-i\,\hat{H}_{\mathrm{TWPA}^{\mathrm{eff}}}t/\hbar}\,|N_{\mathrm{s}},0_{\mathrm{i}}\rangle = (\cosh\kappa)^{-(1+N_{\mathrm{s}})}\sum_{n=0}^{\infty}\frac{(i\tanh\kappa)^n}{n!}\left(\hat{a}_{\mathrm{s}}^{\dagger}\hat{a}_{\mathrm{i}}^{\dagger}\right)^n|N_{\mathrm{s}},0_{\mathrm{i}}\rangle\,, \tag{4.29}$$

or, in case of a degenerate amplifier

$$\mathrm{e}^{-i\hat{H}_{\mathrm{deg}}t/\hbar}\,|N_{\mathrm{s}},0_{\mathrm{i}}\rangle = (\cosh 2\kappa)^{-1/2(1+2N_{\mathrm{s}})}\sum_{n=0}^{\infty}\frac{\left(i\mathrm{e}^{i\Delta\phi}/2\tanh 2\kappa\right)^n}{n!}\left(\hat{a}_{\mathrm{s}}^{\dagger}\hat{a}_{\mathrm{i}}^{\dagger}\right)^n|N_{\mathrm{s}}\rangle\,, \tag{4.30}$$

where N_{s} is the number of signal photons initially present and $\kappa \equiv \chi t$. Applying the former relation to $|\psi\rangle_2$, we obtain the state after the TWPAs.

$$\begin{aligned}|\psi\rangle_3 =& \frac{\cosh^{-1}\kappa\cosh^{-1}\kappa'}{\sqrt{2}}\left[\left(i\mathrm{e}^{i\Delta\theta}\cosh^{-1}\kappa\right)\hat{a}_{5\mathrm{s}}^{\dagger}+\left(\cosh^{-1}\kappa'\right)\hat{a}_{8\mathrm{s}}^{\dagger}\right]\cdot\\ &\cdot\sum_{n,m=0}^{\infty}\frac{i^n\tanh^n\kappa}{n!}\frac{i^m\tanh^m\kappa'}{m!}\left(\hat{a}_{5\mathrm{s}}^{\dagger}\hat{a}_{5\mathrm{i}}^{\dagger}\right)^n\left(\hat{a}_{8\mathrm{s}}^{\dagger}\hat{a}_{8\mathrm{i}}^{\dagger}\right)^m|0_{5\mathrm{s}},0_{5\mathrm{i}},0_{8\mathrm{s}}0_{8\mathrm{s}}\rangle\,.\end{aligned} \tag{4.31}$$

where κ and κ' are the amplification in the upper arm and lower arm respectively. Finally, the state traverses the second hybrid which is modelled by the transformations

$$\begin{aligned}\hat{a}_5^{\dagger} &\mapsto \frac{1}{\sqrt{2}}\left(i\hat{a}_6^{\dagger}+\hat{a}_7^{\dagger}\right)\\ \hat{a}_8^{\dagger} &\mapsto \frac{1}{\sqrt{2}}\left(\hat{a}_6^{\dagger}+i\hat{a}_7^{\dagger}\right)\end{aligned} \tag{4.32}$$

for both signal and idler. Thus, we arrive at the output state

$$\begin{aligned}|\psi\rangle_4 =& \frac{1}{2}\cosh^{-1}\kappa\cosh^{-1}\kappa'\left[\left(\frac{-\mathrm{e}^{i\Delta\theta}}{\cosh\kappa}+\frac{1}{\cosh\kappa'}\right)\hat{a}_{6\mathrm{s}}^{\dagger}+\left(\frac{i\mathrm{e}^{i\Delta\theta}}{\cosh\kappa}+\frac{i}{\cosh\kappa'}\right)\hat{a}_{7\mathrm{s}}^{\dagger}\right]\cdot\\ &\cdot\sum_{n,m=0}^{\infty}\frac{i^n\tanh^n\kappa}{2^n n!}\frac{i^m\tanh^m\kappa'}{2^m m!}\left(-\hat{a}_{6\mathrm{s}}^{\dagger}\hat{a}_{6\mathrm{i}}^{\dagger}+i\left\{\hat{a}_{6\mathrm{s}}^{\dagger}\hat{a}_{7\mathrm{i}}^{\dagger}+\hat{a}_{7\mathrm{s}}^{\dagger}\hat{a}_{6\mathrm{i}}^{\dagger}\right\}+\hat{a}_{7\mathrm{s}}^{\dagger}\hat{a}_{7\mathrm{i}}^{\dagger}\right)^n\cdot\\ &\cdot\left(\hat{a}_{6\mathrm{s}}^{\dagger}\hat{a}_{6\mathrm{i}}^{\dagger}+i\left\{\hat{a}_{6\mathrm{s}}^{\dagger}\hat{a}_{7\mathrm{i}}^{\dagger}+\hat{a}_{7\mathrm{s}}^{\dagger}\hat{a}_{6\mathrm{i}}^{\dagger}\right\}-\hat{a}_{7\mathrm{s}}^{\dagger}\hat{a}_{7\mathrm{i}}^{\dagger}\right)^m|0_{6\mathrm{s}},0_{6\mathrm{i}},0_{7\mathrm{s}}0_{7\mathrm{s}}\rangle\,.\end{aligned} \tag{4.33}$$

This equation reproduces the interference visibilities as presented in figure 4.2 in case losses are neglected.

D Output of numerical calculations

From our numerical calculations we obtain the probability distribution of number states, $P(\langle n\rangle_{\mathrm{A,s}}=i,\langle n\rangle_{\mathrm{A,i}}=j,\langle n\rangle_{\mathrm{B,s}}=k,\langle n\rangle_{\mathrm{B,i}}=l)$ in detectors A and B ($i,j,k,l\in[0,N-1]$). Using partial traces, we can compute the statistics and correlations for each of the four modes and between pairs of modes. E.g. the number state probability distribution for signal photons in detector B is depicted in figure 4.9.

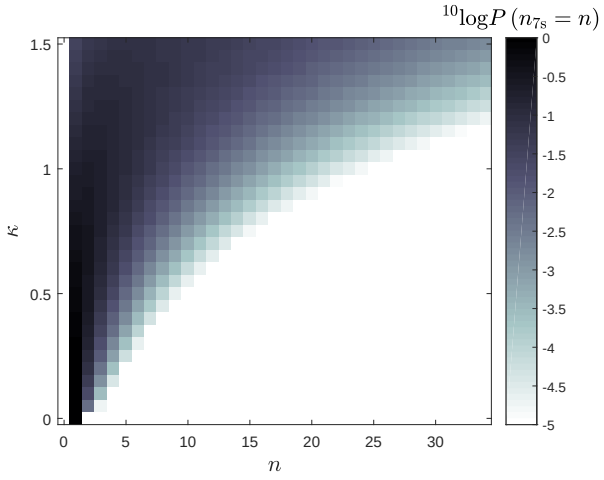


Figure 4.9: *Probability distribution of the interferometer's output in arm 7 (detector B) for the signal mode as a function of amplification κ.*

E Definition of interference visibility

In the main text the interference visibility is defined as

$$V_{\mathrm{s(i)}}\equiv\left.\frac{\langle n_{\mathrm{B,s(A,i)}}\rangle-\langle n_{\mathrm{A,s(B,i)}}\rangle}{\langle n_{\mathrm{B,s(A,i)}}\rangle+\langle n_{\mathrm{A,s(B,i)}}\rangle}\right|_{\Delta\theta=0}. \tag{4.34}$$

The rationale behind this definition can be found in figure 4.10. At $\Delta\theta=0$ we expect the maximum number of signal photons in detector B and the minimum in detector A. For the idler the opposite is the case.

F Comparison of full and reduced Hilbert space

As mentioned, the Hilbert space of the full interferometer scales as N^4 (no loss) and the number of entries in the density matrix scales as N^8 (with loss). However, if the amplifiers are identical, we can obtain the same results for the interference visibility if we perform the calculation twice – once with a $|1\rangle_{\mathrm{s}}|0\rangle_{\mathrm{i}}$-input state and once with a $|0\rangle_{\mathrm{s}}|0\rangle_{\mathrm{i}}$-input state. The first yields $\langle n_{\mathrm{B,s\ (A,i)}}\rangle$ and

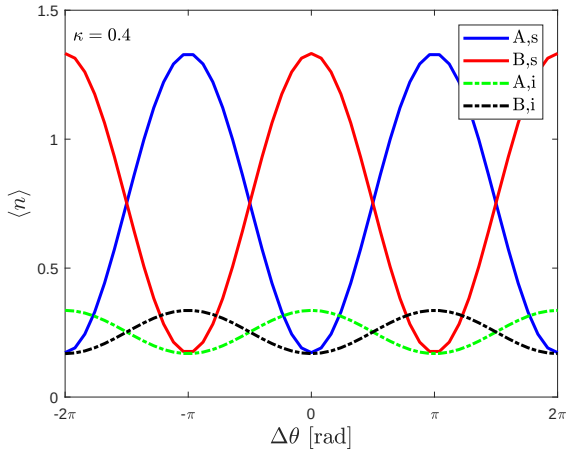


Figure 4.10: *Predicted interference pattern of the interferometer in figure 4.1 (losses neglected): the average number of signal and idler photons in detectors A and B for amplification* 0.4. *At phase shift* $\Delta\theta = 0$ *most of the signal photons are expected in detector A, whereas most of the idler photons end up in detector B.*

the second $\langle n_{\mathrm{A,s\ (B,i)}}\rangle$. This implies that the same results can be obtained with a Hilbert space of $2N^2$ (no loss) or $2N^4$ (with loss).
In figure 4.11 the result of the two calculations is compared as a function of $\Gamma\Delta t_{\mathrm{TWPA}}$ for $\kappa = 0.1$ to 0.4. In this figure, the grey solid data correspond to Qutip's master equation solver, whereas the black dashed data are obtained using the reduced Hilbert space approach. As can be seen, the results overlap very well, such that we can use the reduced Hilbert space for our calculations.

G Interference visibility with losses

In case transmission losses are taken into account, we can fit the average number of photons leaving the interferometer with the function

$$\langle n_{\mathrm{s(i)}}\rangle_{\mathrm{out}} = \langle n_{\mathrm{s(i)}}\rangle_{\mathrm{out}}\,|_{\kappa=0}\cosh^2\kappa + \left(\langle n_{\mathrm{i(s)}}\rangle_{\mathrm{out}}\,|_{\kappa=0} + 1\right)\mathrm{e}^{-f}\sinh^2\kappa \tag{4.35}$$

in which f is a fitting parameter depending on Γ, the various Δts, n_{th} and the input state.

$$\langle n\rangle_{\mathrm{out}}\,|_{\kappa=0} = \left(\langle n\rangle_{\mathrm{in}} - n_{\mathrm{th}}\right)\mathrm{e}^{-\Gamma\Delta t_{\mathrm{tot}}} + n_{\mathrm{th}} \tag{4.36}$$

is the number of photons leaving the interferometer in case the amplification κ equals 0. The result of a particular fit ($\Gamma = 100\,\mathrm{MHz}$, $\Delta t_{\mathrm{TWPA}} = 10\,\mathrm{ns}$ – other Δts are 1 ns, hence $\Gamma\Delta t_{\mathrm{tot}} = 1.3$ –, $n_{\mathrm{th}} = 8.3\times10^{-3}$) is presented in figure 4.12. In figure 4.13 the magnitude of the fitting factor f is plotted as a function of $\Gamma\Delta t_{\mathrm{tot}}$ and n_{th}.

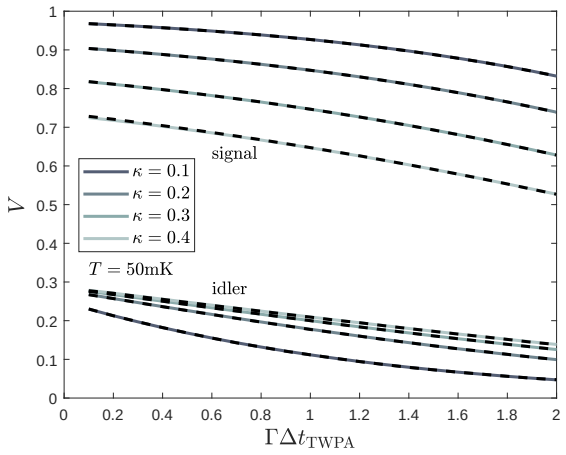


Figure 4.11: *Visibility as a a function of losses in the TWPAs for various κ. $\Gamma = 100\,\mathrm{MHz}$, $T = 50\,\mathrm{mK}$, $\omega_{s,i} = 2\pi \times 5\,\mathrm{GHz}$. $\Gamma\Delta t = 0.1$ in the other components of the set-up. The data in grey (solid) are obtained from* QuTip*'s master equation solver using a N^8 Hilbert space with $N = 5$. Overlain (black dashed) are the data obtained from the reduced Hilbert space ($2N^4$, see text). As can be observed, the overlap is very good.*

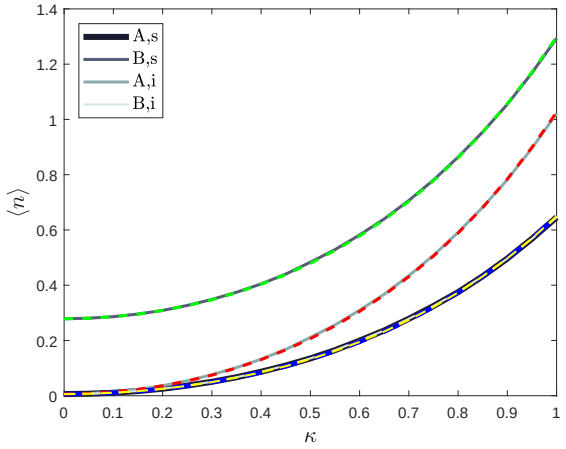
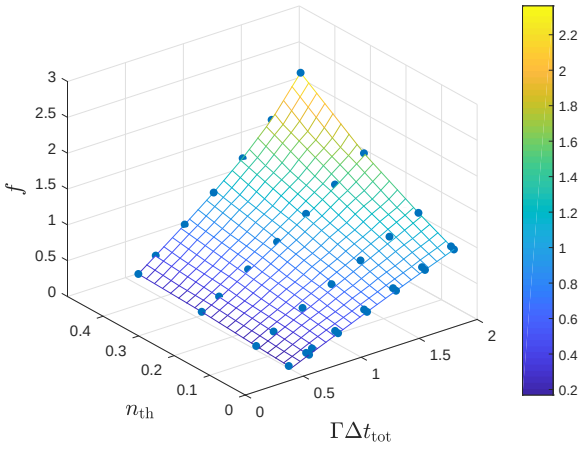
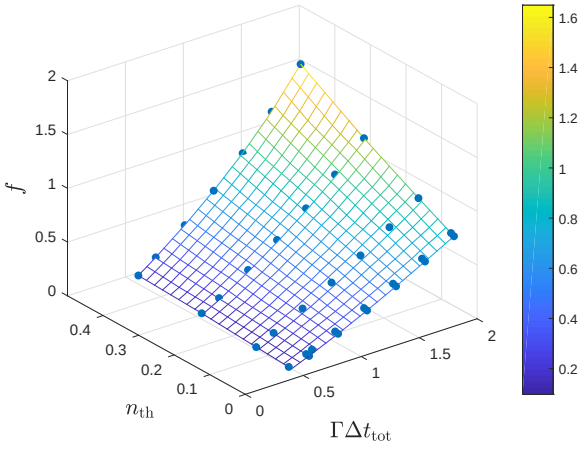


Figure 4.12: *Average number of signal and idler photons reaching the detector as a function of κ ($\Gamma = 100\,\mathrm{MHz}$, $\Delta t_{TWPA} = 10\,\mathrm{ns}$ – other Δts are $1\,\mathrm{ns}$, hence $\Gamma\Delta t_{tot} = 1.3$ –, $n_{th} = 8.3 \times 10^{-3}$). In grey the output from the reduced Hilbert space calculation. The coloured dashed lines are the result from a fit using equation (4.35). Note that the curves for signal photons in detector A and idler photons in detector B are overlapping.*



(a)



(b)

Figure 4.13: *Magnitude of the fitting factor f as function of $\Gamma\Delta t_{tot}$ and n_{th} for the case $\Gamma = 100\,\mathrm{MHz}$ and $\Delta t_{h_1,ps,h_2} = 1\,\mathrm{ns}$. (a) should be used for calculating (A,s), (B,s) and (B,i), whereas (b) should be used for (A,i). The dots represent the numerical data, whereas the mesh is a linear interpolation.*

H Interference visibility with collapse onto coherent states

To study the interference visibility in case of state collapse within the interferometer, we assume that the state collapses onto a coherent state, the most classical state available in quantum mechanics. Coherent states are expanded in Fock space as

$$|\alpha\rangle = \mathrm{e}^{-|\alpha|^2/2} \sum_{n=0}^{\infty} \frac{\alpha^n}{\sqrt{n!}} |n\rangle \tag{4.37}$$

in which $\alpha \in \mathbb{C}$ is the amplitude of the coherent state and $|n\rangle$ are the number states. The mean number of photons in a coherent state equals $|\alpha|^2$. From equation (4.37) we can easily compute the overlap between a coherent state and a number state as

$$\langle \alpha | n \rangle = \mathrm{e}^{-|\alpha|^2/2} \frac{(\alpha^*)^n}{\sqrt{n!}}. \tag{4.38}$$

Assuming that the interferometer is lossless and that the collapse takes place within the interferometer, the squared overlap between the collapsed coherent state $|\psi\rangle_{\mathrm{coll}} = |\alpha_{\mathrm{up,s}}\rangle |\alpha_{\mathrm{up,i}}\rangle |\alpha_{\mathrm{low,s}}\rangle |\alpha_{\mathrm{low,i}}\rangle$ and the instantaneous quantum state, given by equation (4.31) with $\kappa \mapsto \eta\kappa$, is

$$\begin{aligned} |c_{\mathrm{coll}}|^2 = |\langle \psi_{\mathrm{coll}} | \psi_3 \rangle|^2 = \\ = \frac{e^{-\left(|\alpha_{\mathrm{up,s}}|^2 + |\alpha_{\mathrm{up,i}}|^2 + |\alpha_{\mathrm{low,s}}|^2 + |\alpha_{\mathrm{low,i}}|^2\right)}}{2\cosh^6 \eta\kappa} \Big[|\alpha_{\mathrm{up,s}}|^2 + |\alpha_{\mathrm{low,s}}|^2 + \\ + \left(i\, |\alpha_{\mathrm{up,s}}|\, |\alpha_{\mathrm{low,s}}|\, \mathrm{e}^{i(\phi_{\mathrm{low,s}} - \phi_{\mathrm{up,s}})} + c.c. \right) \Big] \cdot \\ \cdot \sum_{n,m,l,k} \frac{(i)^{n+m-l-k} \tanh^{n+m+l+k} \eta\kappa}{n!m!l!k!} \left(|\alpha_{\mathrm{up,s}}|\, |\alpha_{\mathrm{up,i}}| \right)^{n+l} \cdot \\ \cdot \left(|\alpha_{\mathrm{low,s}}|\, |\alpha_{\mathrm{low,i}}| \right)^{m+k} \mathrm{e}^{i(n-l)(\phi_{\mathrm{up,s}} + \phi_{\mathrm{up,i}}) + (m-k)(\phi_{\mathrm{low,s}} + \phi_{\mathrm{low,i}})} \end{aligned} \tag{4.39}$$

in case the amplifiers are equal and setting the amplitudes to $\alpha = |\alpha|\, \mathrm{e}^{i\phi_\alpha}$. The amplifiers evolve the amplitudes of the collapsed state $|\psi_{\mathrm{coll}}\rangle$ further into average amplitudes

$$\bar{\alpha}_{\mathrm{up(low),s(i)}} = \alpha_{\mathrm{up(low),s(i)}} \cosh(1-\eta)\,\kappa + i\alpha^*_{\mathrm{up(low),i(s)}} \sinh(1-\eta)\,\kappa \tag{4.40}$$

and the number of photons arriving in each of the detectors for this particular collapse equals

$$n^{\mathrm{coll}}_{[\mathrm{A}]\{\mathrm{B}\},n} = \frac{1}{2} \left| [i]\{1\}\bar{\alpha}_{\mathrm{up},n} + [1]\{i\}\bar{\alpha}_{\mathrm{low},n} \right|^2. \tag{4.41}$$

In the last expression we have used the standard hybrid transformation relations

$$\alpha_{[\mathrm{A}]\{\mathrm{B}\},n} = \frac{1}{\sqrt{2}}\left([i]\{1\}\alpha_{\mathrm{up},n} + [1]\{i\}\alpha_{\mathrm{low},n}\right) \tag{4.42}$$

as well as that $n^{\mathrm{coll}}_{\mathrm{A(B)},n} = \left|\alpha_{\mathrm{A(B)},n}\right|^2$. Explicitly, using the shorthand notations $\mathrm{c}_{\kappa'} = \cosh\left(1-\eta\right)\kappa$ and $\mathrm{s}_{\kappa'} = \sinh\left(1-\eta\right)\kappa$,

$$\begin{aligned} n^{\mathrm{coll}}_{[\mathrm{A}]\{\mathrm{B}\},\mathrm{s}} = \frac{1}{2}\Bigg[& \left(\left|\alpha_{\mathrm{up,s}}\right|^2 + \left|\alpha_{\mathrm{low,s}}\right|^2\right)\mathrm{c}^2_{\kappa'} + \left(\left|\alpha_{\mathrm{up,i}}\right|^2 + \left|\alpha_{\mathrm{low,i}}\right|^2\right)\mathrm{s}^2_{\kappa'} - \\ & - \left(i\left|\alpha_{\mathrm{up,s}}\right|\left|\alpha_{\mathrm{up,i}}\right|\mathrm{e}^{i(\phi_{\mathrm{up,s}}+\phi_{\mathrm{up,i}})}\mathrm{c}_{\kappa'}\mathrm{s}_{\kappa'} + c.c.\right) + \\ & + [1]\{-1\}\left(i\left|\alpha_{\mathrm{up,s}}\right|\left|\alpha_{\mathrm{low,s}}\right|\mathrm{e}^{i(\phi_{\mathrm{up,s}}-\phi_{\mathrm{low,s}})}\mathrm{c}^2_{\kappa'} + c.c.\right) + \\ & + [1]\{-1\}\left(\left|\alpha_{\mathrm{up,s}}\right|\left|\alpha_{\mathrm{low,i}}\right|\mathrm{e}^{i(\phi_{\mathrm{up,s}}+\phi_{\mathrm{low,i}})}\mathrm{c}_{\kappa'}\mathrm{s}_{\kappa'} + c.c.\right) + \\ & + [-1]\{1\}\left(\left|\alpha_{\mathrm{up,i}}\right|\left|\alpha_{\mathrm{low,s}}\right|\mathrm{e}^{-i(\phi_{\mathrm{up,i}}+\phi_{\mathrm{low,s}})}\mathrm{c}_{\kappa'}\mathrm{s}_{\kappa'} + c.c.\right) + \\ & + [1]\{-1\}\left(i\left|\alpha_{\mathrm{up,i}}\right|\left|\alpha_{\mathrm{low,i}}\right|\mathrm{e}^{-i(\phi_{\mathrm{up,i}}-\phi_{\mathrm{low,i}})}\mathrm{s}^2_{\kappa'} + c.c.\right) - \\ & - \left(i\left|\alpha_{\mathrm{low,s}}\right|\left|\alpha_{\mathrm{low,i}}\right|\mathrm{e}^{i(\phi_{\mathrm{low,s}}+\phi_{\mathrm{low,i}})}\mathrm{c}_{\kappa'}\mathrm{s}_{\kappa'} + c.c.\right)\Bigg], \end{aligned} \tag{4.43}$$

$$\begin{aligned} n^{\mathrm{coll}}_{[\mathrm{A}]\{\mathrm{B}\},\mathrm{i}} = \frac{1}{2}\Bigg[& \left(\left|\alpha_{\mathrm{up,s}}\right|^2 + \left|\alpha_{\mathrm{low,s}}\right|^2\right)\mathrm{s}^2_{\kappa'} + \left(\left|\alpha_{\mathrm{up,i}}\right|^2 + \left|\alpha_{\mathrm{low,i}}\right|^2\right)\mathrm{c}^2_{\kappa'} - \\ & - \left(i\left|\alpha_{\mathrm{up,s}}\right|\left|\alpha_{\mathrm{up,i}}\right|\mathrm{e}^{i(\phi_{\mathrm{up,s}}+\phi_{\mathrm{up,i}})}\mathrm{s}_{\kappa'}\mathrm{c}_{\kappa'} + c.c.\right) + \\ & + [1]\{-1\}\left(i\left|\alpha_{\mathrm{up,s}}\right|\left|\alpha_{\mathrm{low,s}}\right|\mathrm{e}^{-i(\phi_{\mathrm{up,s}}-\phi_{\mathrm{low,s}})}\mathrm{s}^2_{\kappa'} + c.c.\right) + \\ & + [-1]\{1\}\left(\left|\alpha_{\mathrm{up,s}}\right|\left|\alpha_{\mathrm{low,i}}\right|\mathrm{e}^{-i(\phi_{\mathrm{up,s}}+\phi_{\mathrm{low,i}})}\mathrm{s}_{\kappa'}\mathrm{c}_{\kappa'} + c.c.\right) + \\ & + [1]\{-1\}\left(\left|\alpha_{\mathrm{up,i}}\right|\left|\alpha_{\mathrm{low,s}}\right|\mathrm{e}^{i(\phi_{\mathrm{up,i}}+\phi_{\mathrm{low,s}})}\mathrm{s}_{\kappa'}\mathrm{c}_{\kappa'} + c.c.\right) + \\ & + [1]\{-1\}\left(i\left|\alpha_{\mathrm{up,i}}\right|\left|\alpha_{\mathrm{low,i}}\right|\mathrm{e}^{i(\phi_{\mathrm{up,i}}-\phi_{\mathrm{low,i}})}\mathrm{c}^2_{\kappa'} + c.c.\right) - \\ & - \left(i\left|\alpha_{\mathrm{low,s}}\right|\left|\alpha_{\mathrm{low,i}}\right|\mathrm{e}^{i(\phi_{\mathrm{low,s}}+\phi_{\mathrm{low,i}})}\mathrm{s}_{\kappa'}\mathrm{c}_{\kappa'} + c.c.\right)\Bigg]. \end{aligned} \tag{4.44}$$

With these ingredients we can obtain the average number of photons arriving in each of the detectors as

$$\langle n^{\mathrm{coll}}_{X,n}\rangle = \frac{1}{\pi^4}\int n^{\mathrm{coll}}_{X,n}|c_{\mathrm{coll}}|^2\ \mathrm{d}^2\alpha_{\mathrm{up,s}}\mathrm{d}^2\alpha_{\mathrm{up,i}}\mathrm{d}^2\alpha_{\mathrm{low,s}}\mathrm{d}^2\alpha_{\mathrm{low,i}} \tag{4.45}$$

as discussed in the main text. Here, $\mathrm{d}^2\alpha = |\alpha|\,\mathrm{d}\phi_\alpha \mathrm{d}\alpha$ and the bounds of the integrals are $[0,\infty\rangle$ for integration over the amplitudes and $[0,2\pi\rangle$ for integration over the phases.
Due to the complex exponentials in equations (4.39) and (4.43) and the integration over the full $[0,2\pi\rangle$ for the phases, it is immediatelly observed that the integrand of equation (4.45) only contributes to the integral for integrand terms that are independent of $\phi_{\mathrm{up(low),s(i)}}$. Then, integration over the phases yields a factor $16\pi^4$.
For the calculation of $\langle n^{\mathrm{coll}}_{\mathrm{B,s}}\rangle - \langle n^{\mathrm{coll}}_{\mathrm{A,s}}\rangle$ and $\langle n^{\mathrm{coll}}_{\mathrm{A,i}}\rangle - \langle n^{\mathrm{coll}}_{\mathrm{B,i}}\rangle$ we find that only the terms scaling as $\mathrm{e}^{\pm i(\phi_{\mathrm{up,s}}-\phi_{\mathrm{low,s}})}$ and $\mathrm{e}^{\pm i(\phi_{\mathrm{up,i}}-\phi_{\mathrm{low,i}})}$ from equations (4.43) and (4.44) will contribute to the integral. For the term scaling as $\mathrm{e}^{i(\phi_{\mathrm{up,s}}-\phi_{\mathrm{low,s}})}$ we find a contribution to $\langle n^{\mathrm{coll}}_{\mathrm{B,s}}\rangle - \langle n^{\mathrm{coll}}_{\mathrm{A,s}}\rangle$

$$\begin{aligned}\Delta_{\mathrm{s},1} = &\frac{8\cosh^2(1-\eta)\,\kappa}{\cosh^6\eta\kappa}\cdot\\ &\cdot\int e^{-\left(|\alpha_{\mathrm{up,s}}|^2+|\alpha_{\mathrm{up,i}}|^2+|\alpha_{\mathrm{low,s}}|^2+|\alpha_{\mathrm{low,i}}|^2\right)}|\alpha_{\mathrm{up,s}}|^3|\alpha_{\mathrm{up,i}}||\alpha_{\mathrm{low,s}}|^3|\alpha_{\mathrm{low,i}}|\cdot\\ &\cdot B_0\left(2\,|\alpha_{\mathrm{up,s}}|\,|\alpha_{\mathrm{up,i}}|\tanh\eta\kappa\right)B_0\left(2\,|\alpha_{\mathrm{low,s}}|\,|\alpha_{\mathrm{low,i}}|\tanh\eta\kappa\right)\cdot\\ &\cdot\mathrm{d}\,|\alpha_{\mathrm{up,s}}|\,\mathrm{d}\,|\alpha_{\mathrm{up,i}}|\,\mathrm{d}\,|\alpha_{\mathrm{low,s}}|\,\mathrm{d}\,|\alpha_{\mathrm{low,i}}|\,,\end{aligned} \tag{4.46}$$

where we have used the identity $\sum_{n=0}^{\infty} x^{2n}/(n!)^2 = B_0(2x)$, in which $B_n(x)$ is the modified Bessel function of the first kind. For the contribution from equation (4.43) scaling as $\mathrm{e}^{-i(\phi_{\mathrm{up,s}}-\phi_{\mathrm{low,s}})}$ we find the same expression. For the term in equation (4.43) scaling as $\mathrm{e}^{i(\phi_{\mathrm{up,i}}-\phi_{\mathrm{low,i}})}$ we find a contribution

$$\begin{aligned}\Delta_{\mathrm{s},2} = &\frac{8\sinh^2(1-\eta)\,\kappa}{\cosh^6\eta\kappa}\cdot\\ &\cdot\int e^{-\left(|\alpha_{\mathrm{up,s}}|^2+|\alpha_{\mathrm{up,i}}|^2+|\alpha_{\mathrm{low,s}}|^2+|\alpha_{\mathrm{low,i}}|^2\right)}|\alpha_{\mathrm{up,s}}|^2|\alpha_{\mathrm{up,i}}|^2|\alpha_{\mathrm{low,s}}|^2|\alpha_{\mathrm{low,i}}|^2\cdot\\ &\cdot\left[B_1\left(2\,|\alpha_{\mathrm{up,s}}|\,|\alpha_{\mathrm{up,i}}|\tanh\eta\kappa\right)-|\alpha_{\mathrm{up,s}}|\,|\alpha_{\mathrm{up,i}}|\tanh\eta\kappa\right]\cdot\\ &\cdot\left[B_1\left(2\,|\alpha_{\mathrm{low,s}}|\,|\alpha_{\mathrm{low,i}}|\tanh\eta\kappa\right)-|\alpha_{\mathrm{low,s}}|\,|\alpha_{\mathrm{low,i}}|\tanh\eta\kappa\right]\cdot\\ &\cdot\mathrm{d}\,|\alpha_{\mathrm{up,s}}|\,\mathrm{d}\,|\alpha_{\mathrm{up,i}}|\,\mathrm{d}\,|\alpha_{\mathrm{low,s}}|\,\mathrm{d}\,|\alpha_{\mathrm{low,i}}|\end{aligned} \tag{4.47}$$

to $\langle n^{\mathrm{coll}}_{\mathrm{B,s}}\rangle - \langle n^{\mathrm{coll}}_{\mathrm{A,s}}\rangle$. Here we have used the identity $\sum_{n=0}^{\infty} x^{2n+1}/[(n+1)\,(n!)^2] = B_1(2x) - x$. Again, the contribution of the term in equation (4.43) scaling as $\mathrm{e}^{-i(\phi_{\mathrm{up,i}}-\phi_{\mathrm{low,i}})}$ yields an equal contrbution, such that

$$\langle n^{\mathrm{coll}}_{\mathrm{B,s}}\rangle - \langle n^{\mathrm{coll}}_{\mathrm{A,s}}\rangle = 2\left(\Delta_{\mathrm{s},1}+\Delta_{\mathrm{s},2}\right). \tag{4.48}$$

For $\langle n^{\mathrm{coll}}_{\mathrm{A,i}}\rangle - \langle n^{\mathrm{coll}}_{\mathrm{B,i}}\rangle$ we find the similar expression

$$\langle n^{\mathrm{coll}}_{\mathrm{A,i}}\rangle - \langle n^{\mathrm{coll}}_{\mathrm{B,i}}\rangle = 2\left(\Delta_{\mathrm{i},1}+\Delta_{\mathrm{i},2}\right), \tag{4.49}$$

in which $\Delta_{\mathrm{i},1(2)}$ follow from equations (4.46) and (4.47) by replacing $\cosh(1-\eta)\kappa$ with $\sinh(1-\eta)\kappa$ and vice versa.

Similarly, we find that for the calculation of $\langle n^{\mathrm{coll}}_{\mathrm{B,s}}\rangle + \langle n^{\mathrm{coll}}_{\mathrm{A,s}}\rangle$ and $\langle n^{\mathrm{coll}}_{\mathrm{A,i}}\rangle + \langle n^{\mathrm{coll}}_{\mathrm{B,i}}\rangle$ only the terms without exponential factor and the terms scaling as $\mathrm{e}^{\pm i(\phi_{\mathrm{up,s}}+\phi_{\mathrm{up,i}})}$ and $\mathrm{e}^{\pm i(\phi_{\mathrm{low,s}}+\phi_{\mathrm{low,i}})}$ from equations (4.43) and (4.44) will contribute to the integral. For the terms without exponential we find a contribution

$$\begin{aligned}\Sigma_{\mathrm{s},1} = &\frac{8}{\cosh^6\eta\kappa}\cdot\\ &\cdot\int \mathrm{e}^{-\left(|\alpha_{\mathrm{up,s}}|^2+|\alpha_{\mathrm{up,i}}|^2+|\alpha_{\mathrm{low,s}}|^2+|\alpha_{\mathrm{low,i}}|^2\right)}|\alpha_{\mathrm{up,s}}|\,|\alpha_{\mathrm{up,i}}|\,|\alpha_{\mathrm{low,s}}|\,|\alpha_{\mathrm{low,i}}|\cdot\\ &\cdot\left(|\alpha_{\mathrm{up,s}}|^2+|\alpha_{\mathrm{low,s}}|^2\right)\left[\left(|\alpha_{\mathrm{up,s}}|^2+|\alpha_{\mathrm{low,s}}|^2\right)\cosh^2(1-\eta)\kappa+\right.\\ &\left.+\left(|\alpha_{\mathrm{up,i}}|^2+|\alpha_{\mathrm{low,i}}|^2\right)\sinh^2(1-\eta)\kappa\right]\cdot\\ &\cdot B_0\left(2|\alpha_{\mathrm{up,s}}|\,|\alpha_{\mathrm{up,i}}|\tanh\eta\kappa\right)B_0\left(2|\alpha_{\mathrm{low,s}}|\,|\alpha_{\mathrm{low,i}}|\tanh\eta\kappa\right)\cdot\\ &\cdot\mathrm{d}\,|\alpha_{\mathrm{up,s}}|\,\mathrm{d}\,|\alpha_{\mathrm{up,i}}|\,\mathrm{d}\,|\alpha_{\mathrm{low,s}}|\,\mathrm{d}\,|\alpha_{\mathrm{low,i}}|\end{aligned} \tag{4.50}$$

to $\langle n^{\mathrm{coll}}_{\mathrm{B,s}}\rangle + \langle n^{\mathrm{coll}}_{\mathrm{A,s}}\rangle$. Again, the contribution to $\langle n^{\mathrm{coll}}_{\mathrm{A,i}}\rangle + \langle n^{\mathrm{coll}}_{\mathrm{B,i}}\rangle$, $\Sigma_{\mathrm{i},1}$, is the same except that $\cosh(1-\eta)\kappa \mapsto \sinh(1-\eta)\kappa$. For the term scaling as $\mathrm{e}^{i(\phi_{\mathrm{up,s}}+\phi_{\mathrm{up,i}})}$ we find a contribution

$$\begin{aligned}\Sigma_2 = &\frac{8\cosh(1-\eta)\kappa\sinh(1-\eta)\kappa}{\cosh^6\eta\kappa}\cdot\\ &\cdot\int \mathrm{e}^{-\left(|\alpha_{\mathrm{up,s}}|^2+|\alpha_{\mathrm{up,i}}|^2+|\alpha_{\mathrm{low,s}}|^2+|\alpha_{\mathrm{low,i}}|^2\right)}|\alpha_{\mathrm{up,s}}|^2\,|\alpha_{\mathrm{up,i}}|^2\,|\alpha_{\mathrm{low,s}}|\,|\alpha_{\mathrm{low,i}}|\cdot\\ &\cdot\left(|\alpha_{\mathrm{up,s}}|^2+|\alpha_{\mathrm{low,s}}|^2\right)B_0\left(2|\alpha_{\mathrm{low,s}}|\,|\alpha_{\mathrm{low,i}}|\tanh\eta\kappa\right)\cdot\\ &\cdot\left[B_1\left(2|\alpha_{\mathrm{up,s}}|\,|\alpha_{\mathrm{up,i}}|\tanh\eta\kappa\right)-|\alpha_{\mathrm{up,s}}|\,|\alpha_{\mathrm{up,i}}|\tanh\eta\kappa\right]\cdot\\ &\cdot\mathrm{d}\,|\alpha_{\mathrm{up,s}}|\,\mathrm{d}\,|\alpha_{\mathrm{up,i}}|\,\mathrm{d}\,|\alpha_{\mathrm{low,s}}|\,\mathrm{d}\,|\alpha_{\mathrm{low,i}}|\end{aligned} \tag{4.51}$$

to $\langle n^{\mathrm{coll}}_{\mathrm{B,s}}\rangle + \langle n^{\mathrm{coll}}_{\mathrm{A,s}}\rangle$ and $\langle n^{\mathrm{coll}}_{\mathrm{A,i}}\rangle + \langle n^{\mathrm{coll}}_{\mathrm{B,i}}\rangle$. The contribution from the other exponentially scaling terms from equations (4.43) and (4.44) contributing to the integral yield the same values, whence

$$\langle n^{\mathrm{coll}}_{\mathrm{B,s}}\rangle + \langle n^{\mathrm{coll}}_{\mathrm{A,s}}\rangle = \Sigma_{\mathrm{s},1} + 4\Sigma_2, \tag{4.52}$$

$$\langle n^{\mathrm{coll}}_{\mathrm{A,i}}\rangle + \langle n^{\mathrm{coll}}_{\mathrm{B,i}}\rangle = \Sigma_{\mathrm{i},1} + 4\Sigma_2. \tag{4.53}$$

Using equations (4.48), (4.52), (4.49) and (4.53) we easily compute the interference visibilities for signal and idler. We evaluated the integrals in these equations using Mathematica.

Chapter 5

Developing a travelling-wave parametric amplifier with low insertion loss

This chapter discusses the attempts to develop a Josephson travelling-wave parametric amplifier with low insertion loss. We present the design and fabrication procedure of the device. Then, we study one device in detail. We find that the presented device is mismatched to the 50 Ω-environment from which we estimate the device parameters. Then, we develop a model to study the non-linearity of the device including losses by measuring the combination of self- and cross-modulation resulting from exciting the device with a single tone. Finally, we present our non-linear wave mixing results and find that our device is able to deliver 10 dB of gain for certain frequency bands. We discuss improvements to the device and the experimental set-up.

5.1 Introduction

In recent years many microwave travelling-wave parametric amplifiers (TWPAs) have been developed [1–6]. These amplifiers are able to amplify a broad band of microwave signals with a low noise temperature by non-linear wave mixing and are therefore perfectly suited within multi-qubit read-out experiments, which typically have output signals on single photon level.
For microwave TWPAs, two sources of the non-linear wave mixing have been considered and developed, first the intrinsic kinetic inductance of superconductors [1, 4–6] and secondly the non-linear inductance of Josephson junctions [2, 3]. It was found that these devices were indeed able to amplify signals close to the standard quantum noise limit of a 1/2 added photon per unit bandwidth [7]. One reason for the developed amplifiers not to reach the quantum noise limit exactly is the intrinsic insertion loss of the device. For this reason we set out to develop a TWPA based on Josephson junctions, in which we attempt to minimise the device losses, which also is a key parameter in the experiment proposed in chapter 4.

In this chapter we present the design of the device in section 5.2. We propose to minimise the insertion loss of the device by removing the dielectrics commonly used to match a TWPA to its 50 Ω-environment and using low air bridges instead. These air bridges are separated from the transmission line by the lossless vacuum, instead of a lossy dielectric. In section 5.3 we present the important elements of fabrication for the devices. We characterise the Josephson junctions and show that the low air bridges can be fabricated. Finally, in section 5.4 we present one of the devices that was fabricated. From the impedance mismatch we extract the device parameters, which we use to study its non-linearity using the theory presented in chapter 3. We also present the results of the wave-mixing experiments showing that there is signal gain and idler generation. Necessary improvements of the device and measurement set-up are discussed where applicable.

5.2 Designing the TWPA

5.2.1 Design considerations

In principle, a TWPA is a simple device. There are three conditions that need to be fulfilled by a transmission line in order to become an effective amplifier.

1. Non-linearity: the transmission line should be non-linear, i.e. voltage and current should not be proportional to each other. This provides the wave mixing and thereby the amplification.

2. In general, the non-linearity should provide more amplification than the intrinsic loss of the transmission line. For our quantum experiment described in chapter 4 the losses should be as low as possible.

3. Impedance matching: In order to avoid unwanted reflections in the set-up, the transmission line should be impedance matched to its (electrical) environment. In general, the environment has a characteristic impedance of $50\,\Omega$.

5.2.2 From coplanar waveguide to TWPA

As the basic structure of our TWPA we will use a coplanar waveguide (CPW) structure. We fabricate CPWs using 200 nm-thick NbTiN ($T_c = 15.1\,\mathrm{K}$, $\sigma = 1.06\,\mu\Omega\mathrm{m}$) on a $525\,\mu$m-thick Si substrate. For a CPW that has a centre conductor width of $12\,\mu$m and gaps of $5\,\mu$m at mK-temperatures, we expect $\mathcal{L} = 470\,\mathrm{nH/m}$ and $\mathcal{C} = 177\,\mathrm{pF/m}$ indeed yielding $Z_c \approx 50\,\Omega$.
In our case the non-linearity is provided by Josephson junctions. These can be thought of as non-linear inductors, where the inductance changes as a function of the current running through the junction. When a Josephson junction is embedded in a transmission line, this Josephson inductance is to be added to the geometrical and kinetic contributions to the line inductance. If we assume a Josephson inductance of 100 pH, corresponding to a (DC-)critical current of $I_c = \varphi_0/L_{J,0} = 3.29\,\mu\mathrm{A}$, and a unit cell size of $10\,\mu$m, this amounts to $10\,\mu\mathrm{H/m}$ for the given parameters, a value 20 times larger than the "normal" CPW inductance.
As a consequence, to reach the $50\,\Omega$-characteristic impedance, we need to increase the capacitance of the line. Firstly, we can decrease the gap size of the CPW. Furthermore, we can add parallel-plate capacitors over the line. This method has been used previously by [2], which used parallel plates with a dielectric in between to increase the capacitance of the line. As we want to minimise the (capacitive) losses, we propose to use air bridges over the centre conductor rather than a dielectric. Such bridges do not only increase the capacitance, but also prevent slot modes to arise as it connects the two ground planes of the CPW [8–11].

5.2.3 Sonnet calculations

In order to design a transmission line embedded with Josephson junctions, we model it in Sonnet [12]. With this program, one can calculate the characteristics of planar circuits in a discretised box. The Josephson junctions are modelled as lumped-element inductors and the air bridges as parallel plate capacitors using a second layer and a via, as can be observed in figure 5.1. From a simulation, we get the inductance and capacitance per unit length of the line, while varying the Josephson inductance, $L_{J,0}$, the unit cell size, a, the CPW gap width, w_g and d_{AB}, the air bridge height, as our main design parameters.

First, we run several simulations to optimise the box size, in terms of the number of unit cells simulated, and the discretisation mesh. A larger box and finer mesh yield more precise results, but comes at a cost of computation time. It

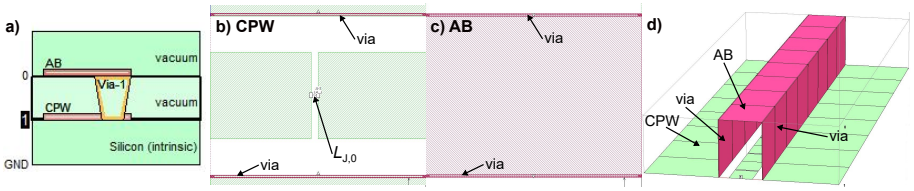


Figure 5.1: *Overview of the unit cell for* Sonnet *calculations. (a) The unit cell consists of* 3 *layers, a Si-substrate on top of which a NbTiN-CPW is positioned. The other two layers are vacua in between which the air bridge is modelled as a Al-parallel plate capacitor. The air bridge and CPW are connected using a via. (b) A unit cell of size* a *consisting of a CPW, parametrised by its centre conductor width* w_c *and gap width* w_g*, with embedded Josephson junction. The junction is modelled as a lumped-element inductor within a junction deposition gap* l_J*. (c) The air bridge layer of the unit cell. The height of the air bridge above the CPW is* d_{AB}*. (d) A* 3*D-view of a series of* 8 *unit cells.*

was found that the results converged more or less taking into account 8 unit cells and using a discretisation mesh of $500 \times 100\,\mathrm{nm}^2$, see figure 5.2.

From the simulations, taking into account technical constraints of fabrication, we found that $L_{\mathrm{J},0} \approx 60\,\mathrm{pH}$ ($I_\mathrm{c} = 5.5\,\mu\mathrm{A}$), $a = 20\,\mu\mathrm{m}$, $w_\mathrm{g} = 1.5\,\mu\mathrm{m}$ and $d_\mathrm{AB} = 100\,\mathrm{nm}$ ($\mathcal{L} = 3.021\,\mu\mathrm{H/m}$ and $\mathcal{C} = 1.294\,\mathrm{nF/m}$). These values yield a characteristic impedance of approximately $48\,\Omega$. However, as the inductance is current dependent, this number will rise to $50\,\Omega$ due to the large pump current in the regime where the device is used as an amplifier.

5.2.4 Analytical approximation

The Sonnet results can be approximated analytically under the following considerations. First, as the geometric and kinetic inductance of the CPW are small compared to the Josephson junction inductance, we assume that they can be neglected. Secondly, we assume that the capacitance can be approximated by

$$\mathcal{C}_\mathrm{g} = 2\epsilon_0\epsilon_\mathrm{r}\frac{E\left(k'\right)}{E\left(k\right)} + \frac{\epsilon_0 w_\mathrm{c}\left(a - l_\mathrm{J}\right)}{d_\mathrm{AB} a}, \tag{5.1}$$

where l_J is the length of the gap in which the Josephson junction is deposited, see figure 5.1. This approximation assumes that the electric field lines originating from the lower side of the centre conductor (the side facing the substrate) couple to the ground plane through the substrate. The electric field lines originating from the upper side of the centre conductor are assumed to couple to the air bridge according to a parallel plate capacitor approximation. The approximated expression for $\mathcal{C}_\mathrm{g}$ is expected to hold for $d_\mathrm{AB} < w_\mathrm{g}$.

In figure 5.3 the Sonnet results and the results of the analytical approximation are compared. The errors are defined as $error = (A - S)/S$, where A is the

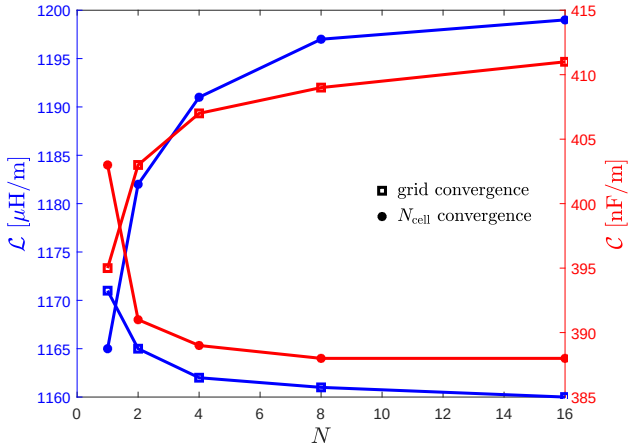


Figure 5.2: *Convergence tests of the* Sonnet *calculations for $\mathcal{L}$ and $\mathcal{C}$. For this simulation $L_{J,0} = 10\,\text{pH}$, $a = 30\,\mu\text{m}$, $w_c = 12\,\mu\text{m}$, $w_g = 0.2\,\mu\text{m}$, whereas we did not simulate the air bridge. In the grid convergence test (squares), the grid size is given by $1.0/N \times 0.2/N\,\mu\text{m}^2$. For the N_{cell} convergence test $N = N_{cell}$. We find that $\mathcal{L}$ and $\mathcal{C}$ have converged well for $N_{cell} = 8$. For the grid we take $N = 2$, which yields an estimate for $\mathcal{L}$ and $\mathcal{C}$ within 1% of the converged value and takes a reasonable amount of time to evaluate.*

approximated result and S is the Sonnet result. For $a = 30\,\mu\text{m}$, $w_c = 12\,\mu\text{m}$ and $l_J = 1.0\,\mu\text{m}$, while varying the Josephson inductance, the CPW gap width and the air bridge height. We find that the error in calculating $\mathcal{L}$ using Sonnet or our approximation is independent of w_g and decreases with increasing $L_{J,0}$ and decreasing d_{AB}. For this dataset the error is found to be less than 20%. This number decreases by decreasing a, since

$$error_{\mathcal{L}} = -\frac{a}{L_{J,0}/\left(\mathcal{L}_g + \mathcal{L}_k\right) + a}, \tag{5.2}$$

setting $A_{\mathcal{L}} = L_{J,0}/a$ and $S_{\mathcal{L}} = L_{J,0}/a + \mathcal{L}_g + \mathcal{L}_k$. Using this equation we expect the maximum error to be less than 14% for $a = 20\,\mu\text{m}$.
The error in $\mathcal{C}$ is found to be less than 3%. As expected the error decreases with decreasing w_g.

5.3 Elements of fabrication

As discussed in section 5.2.2, we want to develop a TWPA based on Josephson junctions and use an air bridge to provide the capacitance to match a characteristic impedance of $50\,\Omega$. In this section we will elaborate on the fabrication of the junctions and bridges.

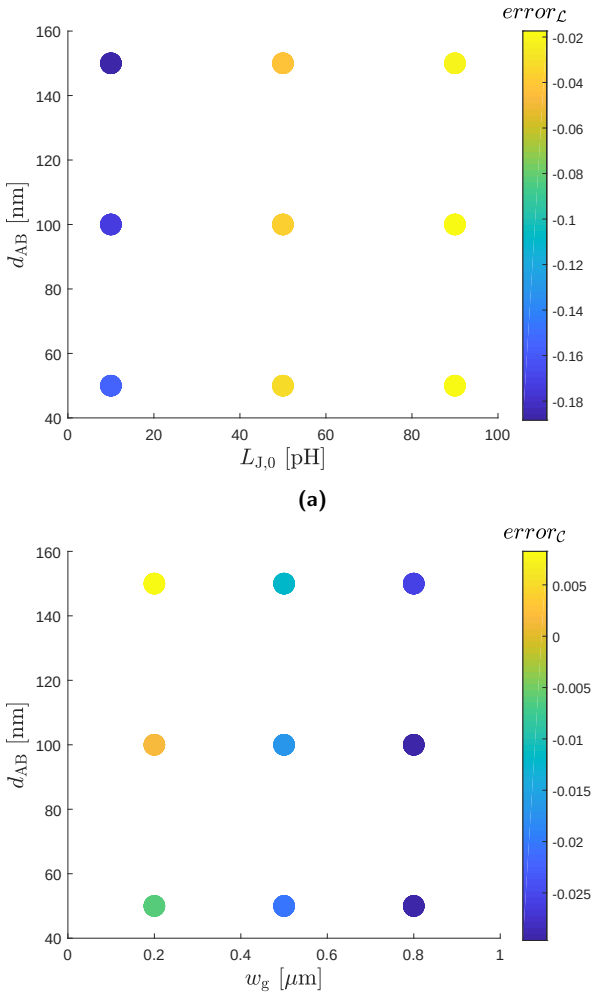


Figure 5.3: *Comparison of the* Sonnet *results and the results of our analytical approximation for* $a = 30\,\mu$m, $w_c = 12\,\mu$m *and* $l_J = 1.0\,\mu$m *varying the Josephson inductance, the CPW gap width and the air bridge height. The errors are defined as* $error = (A - S)/S$, *where* A *is the approximated result and* S *is the* Sonnet *result. Decreasing* a, $error_{\mathcal{L}}$ *will decrease as compared to the presented results as the geometric and kinetic inductance contributions of the CPW decrease relatively with respect to the Josephson inductance.*

5.3.1 Josephson junctions

The DiCarlo lab is specialised in fabricating Josephson junctions using a double angle shadow evaporator and the Dolan bridge technique [13]. Using this technique, two types of junctions can be produced as a result of the evaporation shadow cast by the Dolan bridge, see figure 5.4. Due to the shape of the resist mask for these two junction types, we will refer to these junction types as I-type and Z-type junctions.

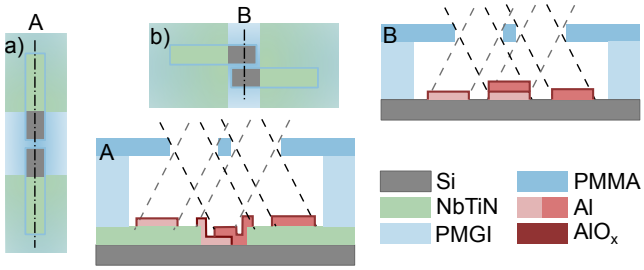


Figure 5.4: *Fabrication principle of Josephson junctions fabricated using the Dolan bridge technique. (a) and (b) show the patterns of the resist mask to produce (a) I-type junctions and (b) Z-type junctions, which are named after the respective patterns that resembles these letters. Al evaporation is from the top and bottom of the figure. A (view in direction of evaporation) and B (view perpendicular to evaporation direction) show the cross-section of the the Josephson junction resulting from double angle shadow evaporation of Al as indicated in (a) and (b). Since the Dolan bridge is only supported at its ends, the size of the resulting junctions is limited.*

Typically, in the DiCarlo lab I- and Z-type junctions are produced with a normal state resistance, R_n, of 3 to 30 kΩ for creating qubit resonators. From this magnitude we can calculate the critical current at $T \ll T_\mathrm{c}$ from the $I_\mathrm{c}R_\mathrm{n}$-product as

$$I_\mathrm{c} \approx \frac{\pi \Delta_\mathrm{sc}(0)}{2eR_\mathrm{n}}, \tag{5.3}$$

where $\Delta_\mathrm{sc}(0) = 1.76 k_\mathrm{B} T_\mathrm{c}$ is the superconducting gap energy at $T = 0\,\mathrm{K}$, which depends on the critical temperature T_c of the superconductor ($\Delta_\mathrm{sc}(0) = 180\,\mu\mathrm{eV}$ for Al with $T_\mathrm{c} = 1.2\,\mathrm{K}$) and e is the elementary charge, to find $I_\mathrm{c} = 10$ to 100 nA. Comparing these values to the design critical current of 5.5 μA, see section 5.2.3, we see that we must increase the junction size.
As the Dolan bridge is only supported at its ends, we cannot increase the junction size indefinitely, as the bridge will collapse. This is indeed what we observed. For this reason we developed the O-type junction using a rectangular pattern written into the resist, as schematically depicted in figures 5.5 and 5.6. This junction type does not use a bridge, but uses the resist (R-mask) or the electrodes (E-mask) as evaporation mask during the evaporation. A scanning electron microscope (SEM) image of these two sorts of junctions is

depicted in figure 5.7. For the data presented in this section, the lift-off step during fabrication of the junctions was performed using N-methyl-2-pyrrolidone (NMP).

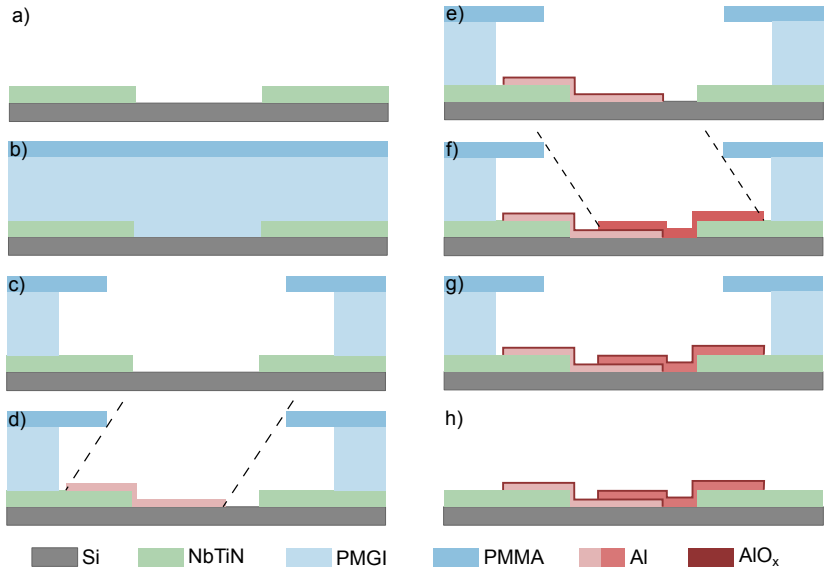


Figure 5.5: *Fabrication process of O-type Josephson junctions using the resist as evaporation mask (R-mask). (a) In a previous fabrication step, we etch the NbTiN that is sputtered onto a Si substrate as to accomodate the junction. (b) A bi-layer of PMGI and PMMA photoresist is spun onto the sample. (c) We pattern the resists using e-beam lithography. Using a larger dose in the middle of the junction as compared to its sides, one can create an overhang of PMMA after development of the resists as PMMA has a larger critical dose than PMGI. This overhang prevents the formation of dog ears during evaporation of the junction. (d) After performing O_2 plasma cleaning and an HF dip to remove the oxides from the NbTiN pads and the Si substrate, we load the sample into the shadow evaporator. The first Al junction electrode is evaporated onto the sample. (e) A small amount of O_2 is allowed into the vacuum chamber of the evaporator to create an AlO_x tunnel barrier in the junction. (f) The O_2 is removed and the second Al junction electrode is evaporated. (g) Again, O_2 is allowed into the vacuum chamber to create an AlO_x layer on top of the second electrode. (h) The sample is taken out of the shadow evaporator and the resists are lifted off. This technique can produce junctions of any size.*

In order to characterise the junctions, we measure the DC IV-curves in a He_3/He_4 dilution refrigerator with a base temperature of 50 mK. The four-point measurement set-up used for this purpose is schematically depicted in figure 5.15. As a current source we use the S4m-(current)module of the IVVI-rack that was developed at TU Delft [14]. We measure the voltage over the junctions using a Keithley digital multimeter. The DC lines going into the refrigerator

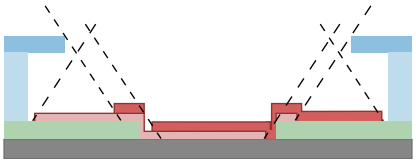
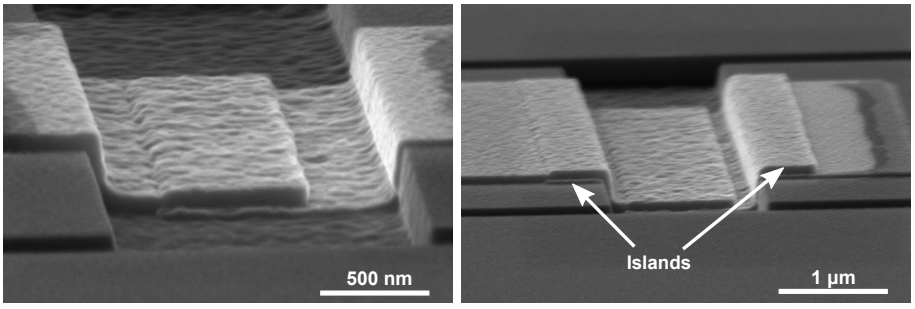


Figure 5.6: *Instead of using the PMMA resist as an evaporation mask (R-mask), one can also use the NbTiN electrodes as a mask (E-mask). The junction thus created is larger and has an "island" on either electrode. Legend as in figure 5.5.*



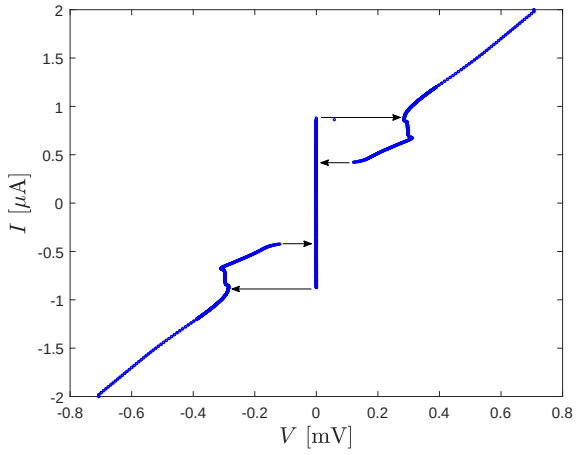
(a) **(b)**

Figure 5.7: *SEM images of a single (a) R-mask and (b) E-mask O-type Josephson junction. The islands, which are absent in the R-mask junction are clearly visible in the E-mask junction, as indicated by white arrows.*

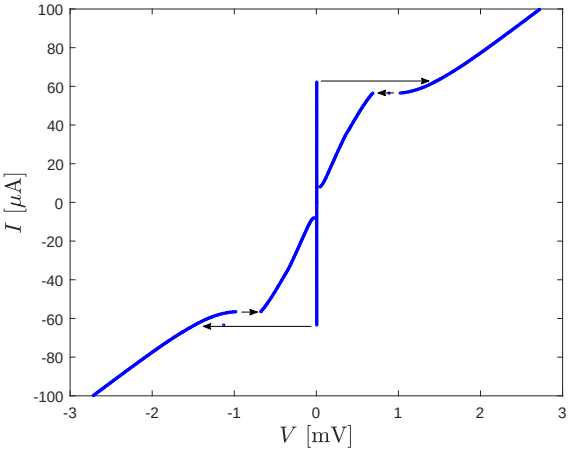
are filtered by a Cu-powder low-pass filter and an RC low-pass filter.
The resulting IV-curves for an R-mask O-type junction and an E-mask O-type junction (not the junctions of figure 5.7) are shown in figure 5.8. The R-mask junction with a junction size of $0.7 \times 1.0\,\mu\text{m}^2$ has a critical current of $0.86\,\mu\text{A}$ and its gap voltage is $290\,\mu\text{V}$, which is 20% lower than the expected gap voltage for Al ($2\Delta_{\text{sc}} = 360\,\mu\text{eV}$). The junction's normal state resistance is observed to be $350\,\Omega$. We ascribe the reduced gap voltage and the shape of the retrapping-current branch in the IV-curve to self-heating effects [15–17]. The E-mask junction has a junction size of $1.5 \times 1.0\,\mu\text{m}^2$ Although this is an increase of only a factor 2 with respect to the R-mask junction area, the normal state resistance of the junction is $27\,\Omega$, its gap voltage equals 1.5 mV and, correspondingly, it has a critical current of $63\,\mu\text{A}$. This might be an effect arising due to the proximity of the NbTiN ($2\Delta_{\text{sc}} = 4.5\,\text{meV}$ for $T_{\text{c}} = 15.0\,\text{K}$). The retrapping current branch shows two retrapping currents. The first is observed at $56\,\mu\text{A}$ and the second at $8.0\,\mu\text{A}$. Currently, we have no explanation for this behaviour, although the Al islands might play a role. Furthermore, it is striking that the final retrapping current lies close to the critical current found for an unproximitised Al junction ($\Delta_{\text{sc}} = 180\,\mu\text{eV}$) with a normal state resistance of $27\,\Omega$, which yields $I_{\text{c}} = 10\,\mu\text{A}$ by equation (5.3).

Furthermore, we test the uniformity of the junctions. We cooled down an array of 53 R-mask O-type junctions of size $1.0 \times 8.0\,\mu\text{m}^2$. As shown in figure 5.9a, we find a good uniformity of the junctions: 49 of the junctions switch at $I = 8.1\,\mu\text{A}$ with an average gap voltage of $264\,\mu\text{V}$ per junction. The other four junctions switch at $3.1\,\mu\text{A}$ ($V_{\text{g}} = 305\,\mu\text{V}$), 10.5, 16.2 ($V_{\text{g}} = 220\,\mu\text{V}$) and $17.6\,\mu\text{A}$ ($V_{\text{g}} = 250\,\mu\text{V}$) respectively. The switching junction at $10.5\,\mu\text{A}$ shows a negative gap voltage of $-20\,\mu\text{V}$, for which we have no explanation. The increased critical current might be explained by figure 5.9b: we observed a few junctions that showed a discontinuity in the junction's shape, which was absent in the rest of the junctions. As the critical current of a junction scales with the junction area, this would give a reason for the observed critical current increase.

To test the uniformity of the E-mask junctions, we cooled down an array of 212 junctions with a size of $0.73 \times 10.0\,\mu\text{m}^2$. This array was designed as an array of R-mask junctions, however, due to a patterning misalignment, the shadow of one side of the junctions was provided by the NbTiN-electrode, see figure 5.10. From the IV-curve of the array, one directly observes that the critical current of the junctions is rather non-uniform. The first junction switches at $I = 15.8\,\mu\text{A}$ and the last one at $86.2\,\mu\text{A}$. This can be explained as follows: the E-mask junction is close to the NbTiN electrode on one side, thus might be proximitised by this material. Then the non-uniformity of the junctions can be explained by the non-uniform NbTiN thickness of the sample arising from the initial sputtering of NbTiN onto the Si substrate [18]. This behaviour makes this junction type unsuited for use in a TWPA, in which one aims for identical junctions.

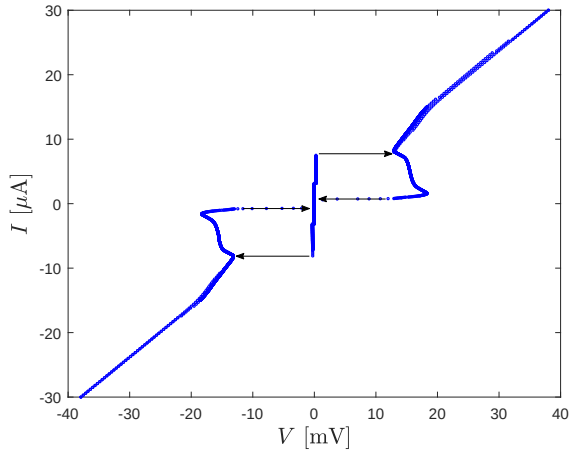


(a)

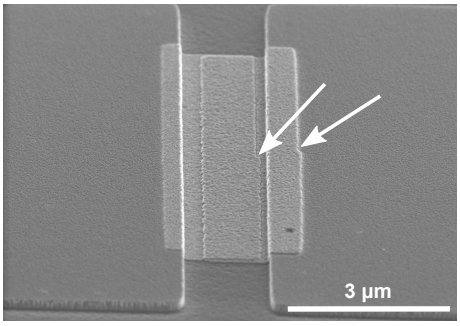


(b)

Figure 5.8: *IV-curves of a single (a) R-mask and (b) E-mask O-type Josephson junction at* $T \approx 50\,\mathrm{mK}$. *The R-mask junction with a junction size of* $0.7 \times 1.0\,\mu\mathrm{m}^2$ *has a critical current of* $0.86\,\mu\mathrm{A}$ *and a gap voltage of* $290\,\mu\mathrm{V}$. *The latter value is* 20% *lower than the expected* $360\,\mu\mathrm{V}$ *for Al, which is ascribed to from self-heating effects. The E-mask junction with a size of* $1.5 \times 1.0\,\mu\mathrm{m}^2$, *however, has* $I_c = 63\,\mu\mathrm{A}$ *and* $V_g = 1.5\,\mathrm{mV}$, *which might be due to the proximity of the NbTiN (*$2\Delta_{sc} = 4.54\,\mathrm{meV}$*).*

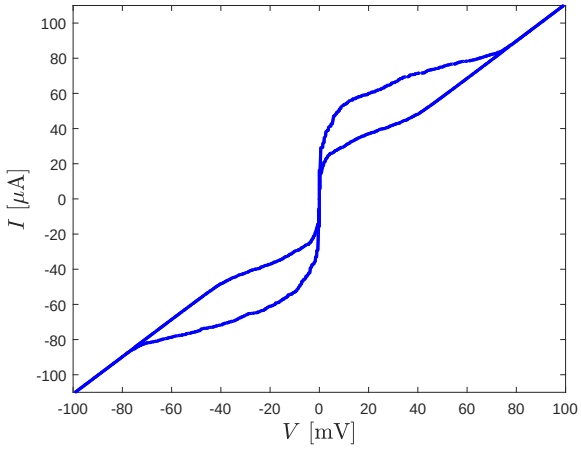


(a)

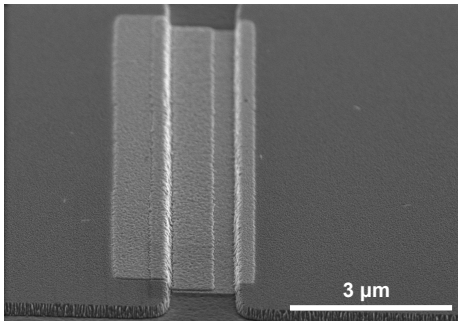


(b)

Figure 5.9: *(a) IV-curve of an array of* 53 *R-mask Josephson junctions of size* $1.0 \times 8.0\,\mu\text{m}^2$*. As can be observed, the uniformity of the E-mask junctions is not perfect:* 1 *junction switches to the normal state at* $I = 3.1\,\mu$A*,* 49 *junctions switch at* $8.1\,\mu$A *and the three last junctions switch at* 10.5*,* 16.2 *and* $17.4\,\mu$A *respectively. (b) SEM image of one of the junctions from the array. The step in junction length of the R-mask junction, indicated by white arrows, was only observed in a few junctions, which could be an explanation for the observed increased switching current of the three junctions.*



(a)



(b)

Figure 5.10: *(a) IV-curve of an array of* 212 *E-mask junctions with a size of* $0.73 \times 10.0\,\mu\text{m}^2$ *and (b) SEM image of one of the junctions of the array. The uniformity of the E-mask junctions in terms of critical current is bad, and is attributed to the proximity effect in combination with a non-uniform thickness of the NbTiN over the sample. This behaviour makes the E-mask O-type junction unsuited for TWPAs.*

5.3.2 Low air bridges

The second important element in our TWPA design is the low air bridge. Generally, air bridges are used to connect two sides of the CPW transmission line together in other to prevent slotline modes, however, they can also be used as parallel plate capacitors that increase the capacitance per unit length of the TWPA.

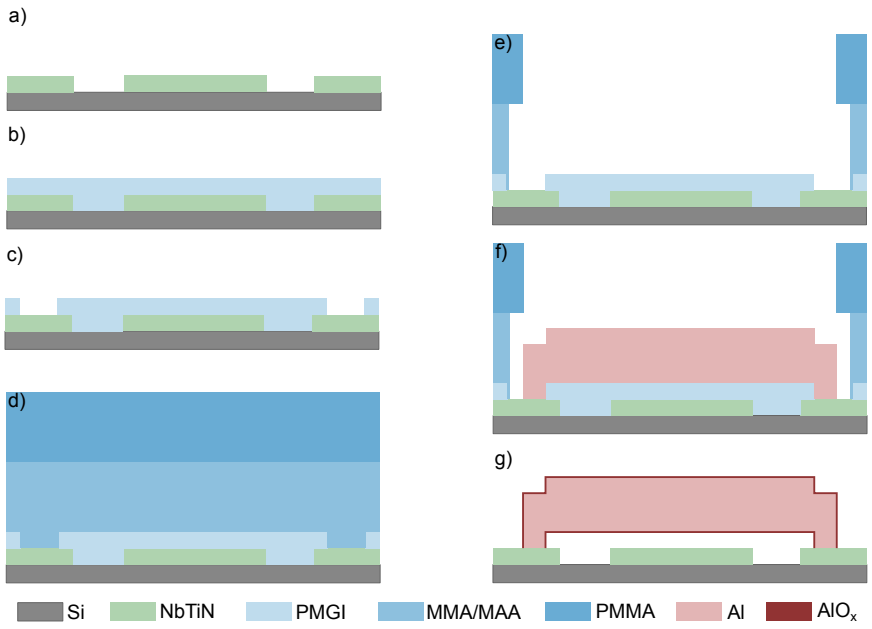
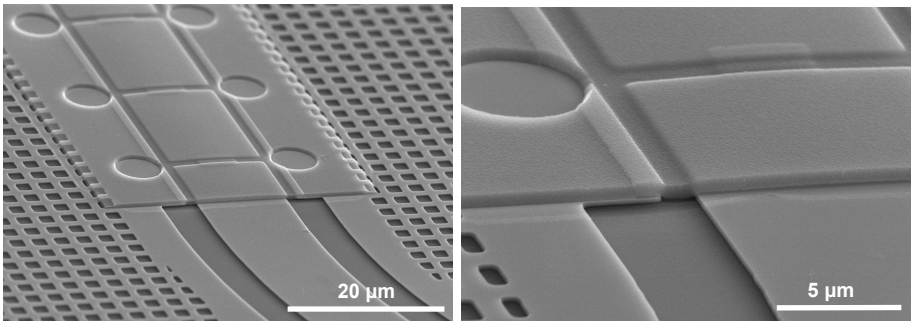


Figure 5.11: *Fabrication process of a low air bridge. (a) Front view of a CPW transmission line in NbTiN as etched in a previous fabrication step. (b) A layer of PMGI resist with the intended thickness of the bridge is spun onto the sample. (c) The "feet" of the air bridge are patterned into the PMGI using e-beam lithography and the resist is developed. Since the air bridge is low, we do not need a resist reflow step to smoothen the edges of the resist. (d) A double layer of MMA/MAA and PMMA is spun onto the sample. The MMA/MAA-layer serves to prevent dog ears from forming on the edges of the bridge. (e) In a second e-beam step, the double resist layer is patterned and developed afterwards. (f) After O_2 plasma cleaning and an HF dip, Al is evaporated onto the sample, creating the air bridge. (g) The resists are lifted off. Due to air contact an AlO_x layer will form around the air bridge.*

The general fabrication procedure for low air bridges is depicted in figure 5.11 and figure 5.12 shows a resulting air bridge. The holes on the sides of the bridge are created for the purpose of easier resist removal from underneath the air bridge in the final fabrication step.

There are three issues with the air bridge depicted in figure 5.12. First, the



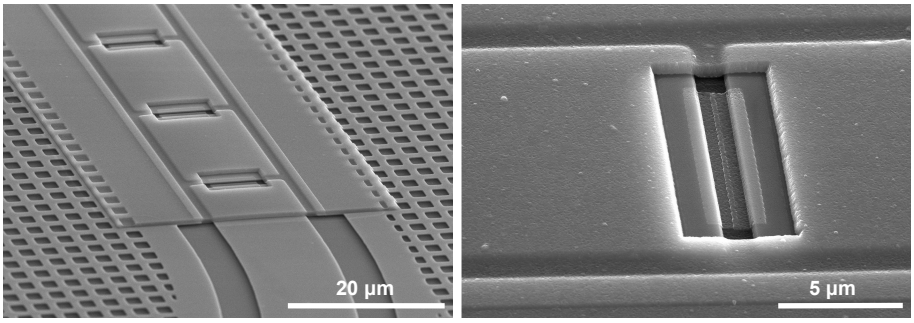
(a) (b)

Figure 5.12: *SEM images of an Al low air bridge over a CPW embedded with Josephson junctions. (a) shows the transition from an ordinary CPW transmission line to the junction embedded transmission line covered by a low air bridge. In (b) a detail of this transition is depicted.*

design of the air bridge makes it impossible to inspect the Josephson junctions after air bridge deposition ("closed" air bridge). To this end we place a resist removal hole directly over the junctions ("open" air bridge), see figure 5.13a.
The second issue arises upon inspection of the junctions after air bridge deposition. We observed that in some fabrication rounds the junctions are damaged, as can be seen in figure 5.13b. This damage occurs during the process of making air bridges. Unfortunately, we have not been able to resolve this issue.
Thirdly, upon measurement of successful devices it was found that the air bridge, although the resist underneath was at design thickness, provides a capacitance largely in excess of the design value, see section 5.4.3. This could be the result of the air bridge collapsing onto the CPW, in which case only the AlO_x layer prevents the line from shorting. To overcome this problem, we have tried to develop NbTiN air bridges. As NbTiN is a stiffer material than Al, a collapse would be less likely. Moreover, since no natural oxide layer forms on NbTiN, the intrinsic losses within a device with NbTiN air bridges might be less than for a device with Al air bridges. Although the fabrication process of NbTiN air bridges worked, the junctions were dissolved along with the resist in the final lift off step, as can be seen in figure 5.13c.

5.4 TWPA813

In this section we highlight one of the successful TWPA devices: TWPA813. We produced this device in the 8th fabrication round on the 1st chip of that round. On that chip it was the 3rd device, hence the name. The device contains 689 Josephson junctions, while for the final device we project to need ∼2000 junctions in order to obtain a gain of 20 dB in a 4 GHz-bandwidth. Here we will describe the design and fabrication of the device and the experimental



(a) (b)

(c)

Figure 5.13: *SEM images of the fabrication issues of the low air bridges. (a) Placing the resist removal hole directly over the Josephson junctions allows to image the junctions after air bridge deposition. (b) In some of the fabrication rounds the junctions appeared to be damaged on the sides after air bridge deposition. (c) Residue of a junction after deposition of a NbTiN air bridge over the junction. Before this image was made, the air bridge was removed by force using a pair of tweezers.*

results obtained from this device. We present single-tone measurements at low and high power. The former allows to estimate the line parameters, whereas from the latter we can study the non-linear behaviour of the device. Finally we will present double-tone measurements results with which one can study idler generation and estimate the gain of the device.

5.4.1 Design and fabrication

Since shadow evaporation of Josephson junctions occurs in a preferred direction, we choose the design methodology of [2] as a basis for our TWPAs. Such TWPAs are divided into sections of non-linear transmission line, which are connected using a linear CPW. TWPA813 contains 689 Josephson junctions, divided over 13 sections with 53 junction unit cells, as depicted in figure 5.14. Each junction unit cell is 20 μm long and consists of an interrupted NbTiN CPW with a central conductor width of 12 μm and a gap width of 1.5 μm. After etching the NbTiN we find that the gap width has become 1.2 μm, which might be due to an e-beam proximity effect. The interruption gap was designed to be 1.5 μm long and was also found to be 1.2 μm in length due to the same effect. The sections are connected by a linear piece of CPW with $w_c = 12\,\mu$m and $w_g = 5\,\mu$m. These connections have a length of 566 μm and are build up as follows: a 5 μm-long straight section followed by a curved section with a radius

of 100 μm. Then follows a larger straight section of length 241.8 μm, that leaves room for future phase-matching resonators, after which the connection connects to the following section by another curved section and a 5 μm-straight section. $2 \times 2\,\mu\text{m}^2$-holes are etched into the NbTiN ground plane with a lattice spacing of 3 μm. This "holey ground" ends 16 μm away from either side of the centre of the CPW central conductor and serves as a vortex pinning lattice to reduce vortex dissipation [19–22].

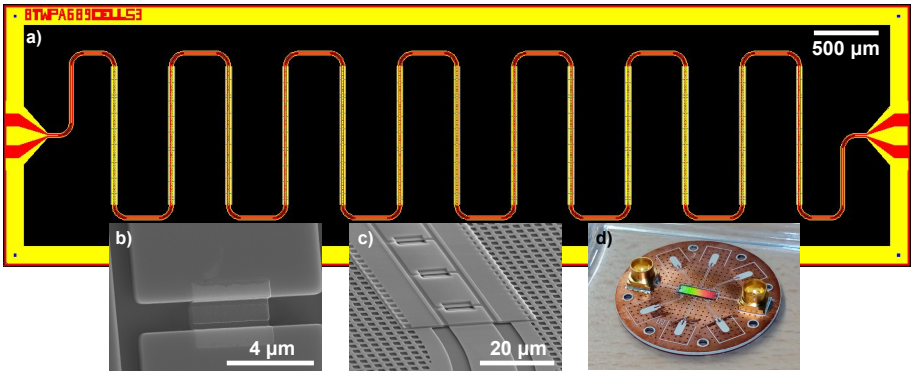


Figure 5.14: *Overview of TWPA813. (a) CAD drawing of the device with 13 TWPA sections each consisting of 53 unit cells. The TWPA sections are connected by a CPW with a length of 566 μm. Insets from left to right: (b) a Josephson junction of the device before air bridge deposition, (c) the beginning of a TWPA section from the finished device and (d) a device on PCB. The entire chip measures $7 \times 2\,\text{mm}^2$.*

The number of unit cells per section, N_{CS} and the length of the CPW connections, l_{conn} are chosen under the constraint that the sum of the section length and the connection length amounts to half a wavelength at the design frequency of the TWPA. That is

$$l_{\text{conn}} = \lambda_{\text{conn}} \left(\frac{1}{2} - \frac{N_{\text{CS}} a}{\lambda_{\text{C}}} \right), \tag{5.4}$$

where $\lambda_{\text{conn}} \approx 16\,\text{mm}$ and $\lambda_{\text{cell}} \approx 2.3\,\text{mm}$ are the instantaneous wavelengths in the CPW connection and the unit cells respectively, as given by

$$\lambda_n = \frac{2\pi}{\omega_{\text{d}} \sqrt{\mathcal{L}_n \mathcal{C}_n}}. \tag{5.5}$$

and using the design values from sections 5.2. For this device we choose a design frequency of $\omega_{\text{d}}/2\pi = 7\,\text{GHz}$.
The advantage of this constraint is that if phase matching $\lambda/4$-resonators (at $\omega_{\text{r}} = \omega_{\text{d}} \approx \omega_{\text{p}}$) are added to the design, a stop band is created around $\omega = 3\omega_{\text{d}}$. Thus, third harmonic generation corresponding to a Hamiltonian mixing term $\hat{a}_{3\text{p}}^\dagger \hat{a}_{\text{p}} \hat{a}_{\text{p}} \hat{a}_{\text{p}}$, where $\hat{a}_{3\text{p}}^\dagger$ is the creation operator for a photon at $\omega = 3\omega_{\text{p}}$ (see chapter 3), is suppressed [2].

The Josephson junctions are deposited in the CPW interruption gaps as described in section 5.3.1. The R-mask junctions have an area of $0.76 \times 5.0\,\mu m^2$, from which we estimate a critical current of 4.7 or 3.9 μA, based on the measurements presented in section 5.3.1 (figures 5.8a and 5.9a) and the linear scaling between critical current and Josephson junction area.
The air bridges are fabricated as described in section 5.3.2. The thickness of the PMGI layer that determines the height of the air bridge was measured to be 110 nm using a profilometer. For the lift off procedure during the fabrication of the junctions, as well as the air bridges, we used Dimethyl sulfoxide (DMSO).

5.4.2 Measurement set-up

The TWPA is cooled down to millikelvin temperatures using a He_3/He_4 dilution refrigerator with a base temperature of 10 mK. The measurement set-up is schematically depicted in figure 5.15. We use three microwave sources and measure the behaviour of the TWPA using a spectrum analyser. The first two sources are denoted "pump" and "signal" and can be used to measure the signal, pump and idler output power individually. The third source is the tracking generator for the spectrum analyser, which enables one to use it as a (quasi) network analyser. With the tracking generator one can study the single-tone non-linear behaviour of the TWPA as well as the signal output power in presence of a pump tone.
Using 3 dB-power dividers in reverse, the outputs of the three sources can be connected to one of the three input lines of the refrigerator. The first line (right) is coupled to the output of the TWPA by the use of a magnetically shielded circulator. This enables one to characterise the reflection of the device. The second line (middle) bypasses the TWPA and is coupled into the output line of the device using a directional coupler. This line characterises the set-up without the device, thus providing an indication for its insertion loss. The third line (right) is coupled to the input of the TWPA and can be used to characterise the device in transmission. The three input lines are attenuated by 20 dB on the 4 K-plate and the 10 mK-plate of the refrigerator, in order to thermalise the noise of the input radiation [23]. The output radiation is amplified by 40 dB using a High Mobility Electron Transistor (HEMT) mounted at the 4 K-plate, whose reflection is decoupled from the TWPA by the circulator.

The TWPA is mounted on a PCB using Al wire bonds and connected to the rest of the set-up by non-magnetic SMP connectors, as depicted in figure 5.14d. The PCB is covered by a metallic lid in order to protect the sample from its environment and then mounted on the 10 mK-plate of the refrigerator.

5.4.3 Results – single-tone excitation

First, we study the single-tone excitation of the device in transmission and reflection by the tracking generator. From measurements at low power compared to the critical power of the device, we determine the line characteristics.

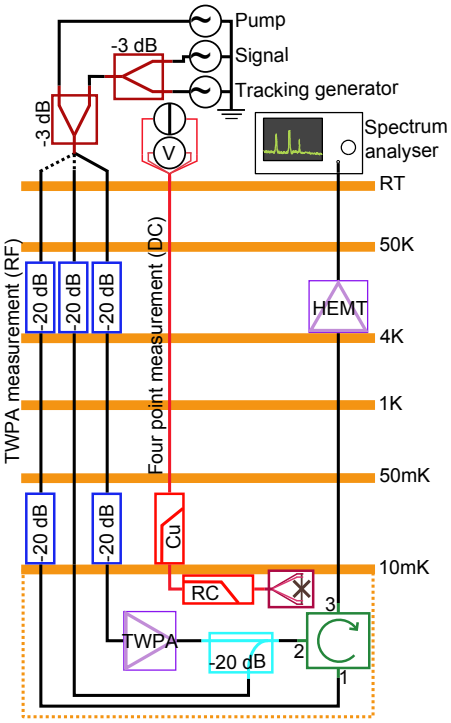


Figure 5.15: *Schematic overview of the setup for characterising TWPAs and Josephson junctions in a He_3/He_4 dilution refrigerator. The various coldplates with indicated temperature of the refridgerator are depicted in orange.*
For TWPA characterisation (black lines) we use a spectrum analyser with optional tracking generator. The setup is fed with three microwave sources. One serves as the input pump tone and the second as an input signal tone. The third source is used as the tracking generator of the spectrum analyser. The tones of the three sources are combined at room temperature using splitters. We have three microwave lines entering the refrigerator, two of which can be used to characterise the TWPA in transmission (right) and reflection (left). The latter is applied to the TWPA using a circulator. The third line serves as a through-line which bypasses the TWPA and is coupled into the output line using a directional coupler for characterising the set-up without TWPA. This also provides an indication of the TWPA's loss. The lines are attenuated by 20 dB *at the* 4 K*-plate and* 20 dB *at the* 10 mK*-plate to thermalise the noise of the input radiation. The output radiation is amplified by a HEMT, which is decoupled from the TWPA using the circulator.*
To characterise Josephson junctions (red lines) we perform a four-point measurement. We apply a DC current to and measure the voltage over the junction. The lines are filtered by a Cu-powder filter and an RC filter mounted on the 10 mK*-plate.*

Furthermore, we study the one-tone non-linear behaviour of the line by increasing the power. In the analysis we will neglect the influence of the Josephson capacitance.

Low power – line characteristics

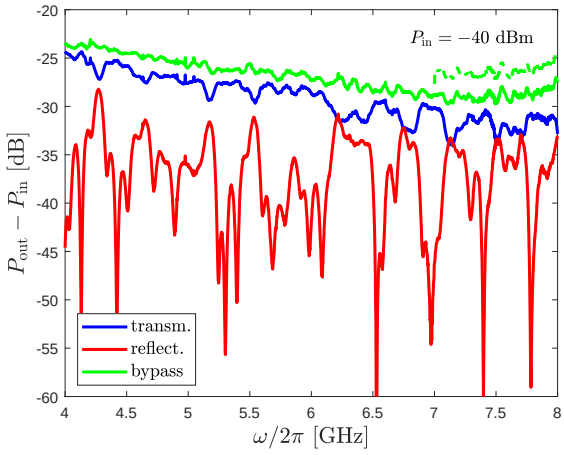
We can determine the line characteristics of the TWPA device by performing transmission and reflection measurements at low power. Figure 5.16a shows the output power of the three microwave lines corrected for the input power of −40 dBm. The power measured by the spectrum analyser shows a discontinuity of 2.5 dBm at 7 GHz, which is explicitly shown for the bypass measurement. This step has been removed manually in the transmission and reflection measurements. From the bypass measurement we estimate the line losses of the full set-up.

$$IL_{\text{lines}} = -\left(P_{\text{out}} - P_{\text{in}}\right) - IL_{\text{att}} + G_{\text{HEMT}}, \tag{5.6}$$

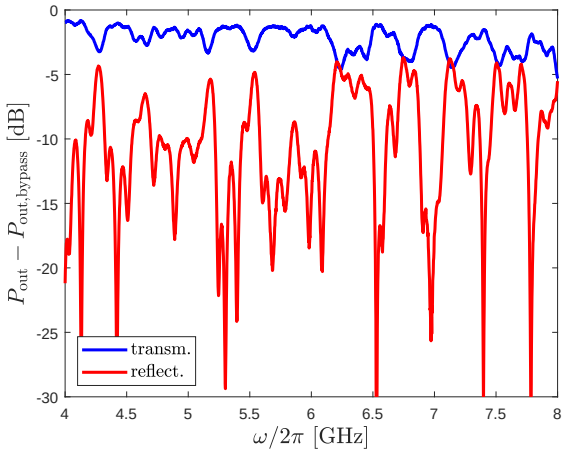
where $IL_{\text{att}} = 20 + 20 + 3 + 3\,\text{dB}$ is the attenuation due to the attenuators ($2 \times 20\,\text{dB}$) and the power splitters ($2 \times 3\,\text{dB}$) in the line. $G_{\text{HEMT}} = 37\,\text{dB}$ is the gain of the HEMT amplifier. For the bypass line we measure $(P_{\text{out}} - P_{\text{in}}) \approx -27\,\text{dB}$, hence the line losses are approximately 18 dB.

To obtain the transmission and reflection data for the device specifically, we subtract the bypass data (in dB) from the latter two, as depicted in figure 5.16b. As described in section 2.3, the observed wiggles indicate an impedance mismatch between the device and its environment.
We observe two wiggle frequencies in the data. We ascribe the first frequency of approximately 400 MHz to the impedance mismatch between the device and the 50 Ω-environment. The second frequency of 100 MHz is also visible in the bypass data for which reason we regard this wiggle as stemming from reflection planes of which at least one lies outside the device. Therefore we will disregard this wiggle frequency in further analysis.

In order to obtain a first estimate of the line characteristics, we ignore the internal reflections of the device resulting from the impedance mismatch between the TWPA sections and the 12 CPW connections. Then, we can determine the line characteristics of the device using the methods described in section 2.3. In this approximation, the device length equals the length of the 13 TWPA sections and 12 CPW connections, $l_{\text{d}} = 20.572\,\text{mm}$. We find $\Delta T_{[\text{dB}]} = 2.8\,\text{dB}$, $\omega_{\text{w}} = 2\pi \times 408\,\text{MHz}$ and $IL = 1.0\,\text{dB}$ at $\omega/2\pi = 7\,\text{GHz}$. However, since the loss diminishes $\Delta T_{[\text{dB}]}$ as discussed in section 2.3, we should choose $IL = 0.70\,\text{dB}$ in order to reproduce the apparent loss of 1 dB from theory. Secondly, the insertion loss that we find is an upper bound to the insertion loss of the device itself, because the bypass line and the transmission line are not equal: the transmission line is longer and passes through the SMP connectors and the Cu leads on the PCB before reaching the actual device. For this reason we will assume $IL \approx 0.35\,\text{dB}$ for the device. From these values we calculate $\mathcal{L}_{\text{d}} = 1.23 \vee 7.23\,\mu\text{H/m}$, $\mathcal{C}_{\text{d}} = 2.89 \vee 491\,\text{pF/m}$ and $r_{\text{d}} = 1.95\,\text{m}^{-1}$. Then, the



(a)



(b)

Figure 5.16: *Measurement of the transmission, reflection and bypass line for TWPA813 at low power compared to the critical power of the device. (a) The three frequency spectra corrected for input power. The discontinuity in output power shown in dashed lines for the bypass measurement is present in all measurements, but has been manually removed. (b) Transmission and reflection of the device corrected by the bypass frequency spectrum to isolate the behaviour of the device.*

phase velocity equals 1.69×10^7 m/s and the calculated characteristic impedance is $20.6 \vee 121\,\Omega$. The calculated transmission using these parameters is depicted in figure 5.17a, together with the data.
Under the assumption of ignoring the internal reflections of the device, we can discern the effective phase velocity in the TWPA sections from the phase velocity in the CPW connections as follows. For the wiggle frequency the relation

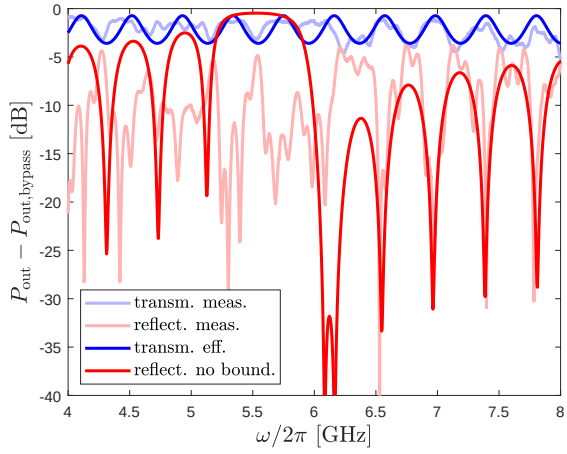
$$k_{\mathrm{w,cell}} l_{\mathrm{sect}} + k_{\mathrm{w,conn}} l_{\mathrm{conn}} = \pi \tag{5.7}$$

must hold. Here, $k_{\mathrm{w},n} = \omega_{\mathrm{w}}/v_{\mathrm{ph},n}$ is the wavenumber of the TWPA section unit cells and CPW connections respectively and l_n is the corresponding total length of the sections and connections. Solving this relation for the phase velocity within the TWPA sections, inserting the phase velocity within the CPW connections of $v_{\mathrm{ph,conn}} = 1.09 \times 10^8$ m/s from the values as given in section 5.2.2, we find $v^{\mathrm{eff}}_{\mathrm{ph,cell}} = 1.19 \times 10^7$ m/s.

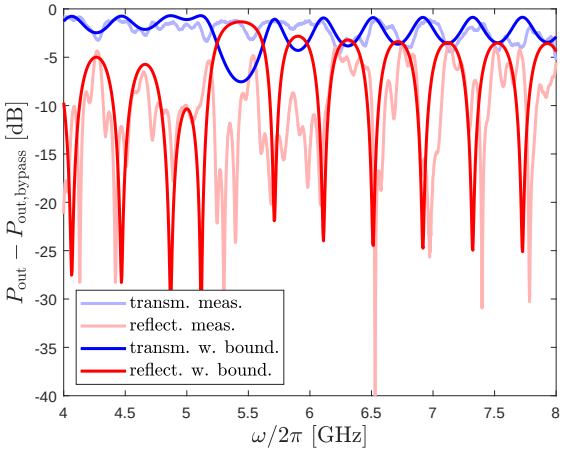
In order to determine whether the low- or high-impedance solution is correct for this device, we calculate the critical current and air bridge height corresponding to $Z_{\mathrm{c}} = 20.6 \vee 121\,\Omega$ and $v^{\mathrm{eff}}_{\mathrm{ph,cell}} = 1.19 \times 10^7$ m/s. $I_{\mathrm{c}} = \varphi_0/\mathcal{L}^{\mathrm{eff}} a = 9.5 \vee 1.6\,\mu$A, where as d_{AB} is obtained from equation 5.1 as $25.6 \vee 221$ nm.
Our estimates of the critical current and air bridge height were $4.3 \pm 0.4\,\mu$A and 110 nm respectively, see section 5.4.1. Comparing the calculated critical current and air bridge height to these numbers we cannot determine whether the low- or high-impedance solution is to be chosen for the TWPA sections. However, in the next section we will argue that we side with the low-impedance solution, because of the non-linearity effects at high pump power. We will adopt this solution for the remainder of this section.

In order to characterise the device further, we analyse the effect of internal reflections. We assume that the losses are evenly distributed over the device. Then, we use the transfer matrix method to model the device, modelling the CPW connections by a characteristic impedance of $51.5\,\Omega$ and a phase velocity equalling 1.09×10^7 m/s. Each TWPA unit cell is modelled by a characteristic impedance of $20.6\,\Omega$ and a phase velocity 1.29×10^7 m/s. This increase in phase velocity with respect to the effective phase velocity stated before is necessary to obtain a reasonable fit of the wiggle frequency. In figure 5.17a we depict the result of this calculation for the reflection of the device. From comparison of the calculation and the data, we directly observe that we are missing an ingredient in our calculation: the model predicts that the maxima in the reflection wiggles are higher for frequencies below 6 GHz than they are for frequencies above 6 GHz. In the data, however, the precise opposite behaviour is observed.

The behaviour of the reflection wiggles points at a missing ingredient. Such can be found in the boundaries between the TWPA sections and CPW connections. In our calculation we modelled these boundaries using the same parameters as for the sections and connections respectively. However, in presence of the air bridge over the TWPA section, the field lines of the CPW are expected to



(a)



(b)

Figure 5.17: *Comparison of theory and measurement of the transmission and reflection of TWPA 813 using the transfer matrix method. (a) Transmission: assuming no internal reflections within the device,* $Z_{c,d} = 20.6\,\Omega$ *and* $v_{ph,d} = 1.69 \times 10^7$ m/s. *Reflection: with internal reflections,* $Z_{c,d} = 20.6\,\Omega$ *and* $v_{ph,d} = 1.29 \times 10^7$ m/s. *The theory for the high-impedance solution provides almost identical results. (b) Theoretical transmission and reflection of the device after application of an additional transfer matrix modelling the boundary of the CPW connections and TWPA sections.* $Z_{c,cell} = 24\,\Omega$ *and* $v_{ph,cell} = 1.31 \times 10^7$ m/s *and for the boundary* $Z_{c,b} = 3.5\,\Omega$ *and* $v_{ph,b} = 5.0 \times 10^6$ m/s. *An almost identical result can be obtained for the high-impedance solution by adjusting the characteristics of the boundary and TWPA unit cell transfer matrix. For the TWPA unit cells, only a slight adjustment was to be made,* $v_{ph,cell} = 1.11 \times 10^7$ m/s.

couple to the air bridge rather than to the ground planes on the sides. We expect this to be an issue for the first and last $5\,\mu$m of each CPW connection, the CPW boundaries.
In principle, one could calculate the instantaneous characteristic impedance and phase velocity of the CPW boundary. Then, in order to fit the data, one could describe the boundary using an infinite amount of transfer matrices connecting the TWPA section and the rest of the CPW connection smoothly. However, this would be a tedious approach. Contrarily, we could describe the CPW boundary using an effective characteristic impedance and phase velocity in order to match the data. Inserting the necessary transfer matrices, indeed the behaviour of the wiggles can be matched to the data, as can be seen in figure 5.17b. Here, for the TWPA section we set $Z_{\mathrm{c,cell}} = 24\,\Omega$ and $v_{\mathrm{ph,cell}} = 1.31 \times 10^7\,\mathrm{m/s}$. For the CPW boundary we set $Z^{\mathrm{eff}}_{\mathrm{c,b}} = 3.5\,\Omega$ and $v^{\mathrm{eff}}_{\mathrm{ph,b}} = 5.0 \times 10^6\,\mathrm{m/s}$. For the rest of the CPW connection we use $Z_{\mathrm{c,conn}} = 51.5\,\Omega$ and $v_{\mathrm{ph,conn}} = 1.09 \times 10^8\,\mathrm{m/s}$ as calculated from the values stated in 5.2.2. From the figure it is observed that the theory describes the measurement well, except for $5 < \omega/2\pi < 6\,\mathrm{GHz}$. However, it was found that we can easily move the high-reflective feature by adjusting the parameters slightly. Moreover, 5.5 GHz corresponds to a line length of approximately 1.2 mm with $v_{\mathrm{ph}} = 1.3 \times 10^7\,\mathrm{m/s}$, which is close to the length of a TWPA section. This allows to interpret the deviation between theory and experiment as arising from the precise characteristics of each individual section to which we have no experimental access.

From fitting the theory to the data we can estimate the characteristic impedance and phase velocity of the sections. For, if the characteristic impedance is chosen either too small or too large, one cannot reproduce the wiggle amplitudes predicted by the theory by adjusting the other parameters. The same holds for the phase velocity and the wiggle frequency. Thus, we can make reasonable estimates of the characteristic impedance and phase velocity of the sections to be $23 \pm 2\,\Omega$ and $1.31 \pm 0.01 \times 10^7\,\mathrm{m/s}$. From these values we deduct a critical current of $9.5 \pm 1.0\,\mu$A and an effective air bridge height of $32 \pm 3\,$nm.
A summary of the results is given in table 5.1.

High power – studying the non-linearity

Increasing the power, we can study the non-linear behaviour of the TWPA device. This non-linear behaviour results from the Josephson inductance, which increases with current, and results in modulation effects.

These modulation effects become apparent in the interference wiggles which will shift if the input power is increased. In a linear system the wiggle frequency is given by $\omega_{\mathrm{w}}/2\pi = v_{\mathrm{ph}}/2l$ arising from the condition $l/\lambda = 1/2$ determining the frequency between two consecutive maxima in the frequency spectrum. In a non-linear system, however, the wavelength of the forward-travelling wave is not necessarily equal to the wavelength of the backward-travelling wave due to self- and cross-modulation between the forward- and backward-propagating

Table 5.1: *Summary of the device parameters of TWPA*813*. The device consists of* 13 *TWPA sections with* 12 *CPW connections in between.*

TWPA813 Device parameters		
Parameter name	symbol	magnitude
Si-substrate		
length/width	$l_{\mathrm{sub}}/w_{\mathrm{sub}}$	7 mm/2 mm
thickness	d_{sub}	525 μm
relative permittivity	$\epsilon_{\mathrm{r,sub}}$	11.45
NbTiN-conductor		
thickness	d_{NbTiN}	200 nm
critical temperature	$T_{\mathrm{c,NbTiN}}$	15.1 K
sheet resistivity at 300 K	σ_{NbTiN}	1.06 $\mu\Omega$m
device length	l_{d}	20.572 mm
loss coefficient	r_{d}	1.95 m^{-1}
CPW connection		
length	l_{conn}	566 μm
central conductor width	$w_{\mathrm{c,conn}}$	12 μm
gap width	$w_{\mathrm{g,conn}}$	5 μm
characteristic impedance	$Z_{\mathrm{c,conn}}$	51.5 Ω
phase velocity	$v_{\mathrm{ph,conn}}$	1.09×10^8 m/s
TWPA section		
# sections	N_{S}	13
# unit cells per section	N_{CS}	53
unit cell length	a	20 μm
central conductor width	$w_{\mathrm{c,cell}}$	12 μm
gap width	$w_{\mathrm{g,cell}}$	1.2 μm
junction gap	l_{J}	1.2 μm
–fabrication estimate–		
critical current	I_{c}	4.3 ± 0.4 μA
air bridge height	d_{AB}	110 nm
–wiggle estimate–		
characteristic impedance	$Z_{\mathrm{c,cell},0}$	23 ± 2 Ω
phase velocity	$v_{\mathrm{ph,cell},0}$	$1.31 \pm 0.01 \times 10^7$ m/s
inductance (/length)	$\mathcal{L}_{\mathrm{cell},0}$	1.75 ± 0.16 μH/m
capacitance (/length)	$\mathcal{C}_{\mathrm{cell}}$	3.35 ± 0.32 nF/m
Josephson inductance	$L_{\mathrm{J},0}$	35 ± 3 pH
critical current	I_{c}	9.5 ± 1.0 μA
air bridge height	d_{AB}	32 ± 3 nm
–no internal reflections estimate–		
characteristic impedance	$Z^{\mathrm{eff}}_{\mathrm{c,cell},0}$	20.6 Ω
phase velocity	$v^{\mathrm{eff}}_{\mathrm{ph,cell},0}$	1.19×10^7 m/s

wave. Moreover, due to losses these wavelengths are position dependent. This implies that the condition needs to be updated to $\Delta\phi_+ + \Delta\phi_- = 2\pi$, where $\Delta\phi_{+(-)}$ is the built-up phase in between the reflection planes in the forward (backward) direction.
In the previous section it was found that the interference wiggles can be described only by taking the reflections between the TWPA sections and the CPW connections into account explicitly. However, we also found that a reasonable fit can be made for frequencies $> 6.2\,\mathrm{GHz}$ in case these reflections are neglected, see figure 5.17a. As the internal reflections complicate the analysis to a great extent, we will assume them to be absent and work with the no-internal reflection parameters from table 5.1, except for the critical current, for which the value estimated including the assumption that there are internal reflections is appropriate.

Under the assumption that the internal reflections of the device can be neglected,

$$\Delta\phi_{+(-)} = \int_0^l K_{+(-)}(z)\,\mathrm{d}z. \tag{5.8}$$

The wavenumber K is non-linear and influenced by self-modulation and cross-modulation with the counter-propagating wave resulting from the reflections in the device. In chapter 3 we found for the wave number modulation

$$\Xi_n |A_\mathrm{p}|^2 = \frac{a^4 k_\mathrm{p}^2 k_n^3 (2-\delta_{\mathrm{p}n})}{16 C_\mathrm{g} I_\mathrm{c}^2 L_{\mathrm{J},0}^3 \omega_n^2} |A_\mathrm{p}|^2 = \frac{2-\delta_{\mathrm{p}n}}{16} k_n \left|\frac{I_\mathrm{p}}{I_\mathrm{c}}\right|^2 \tag{5.9}$$

where the last step follows from the substitutions $A_\mathrm{p} = -I_\mathrm{p} Z_\mathrm{c}/\omega_\mathrm{p}$ and $Z_\mathrm{c} = \sqrt{\mathcal{L}_{\mathrm{J},0}/\mathcal{C}_\mathrm{g}}$ (recall that we are neglecting the Josephson capacitance in this section). The factor 2 in this equation should be chosen for cross-modulation effects and a factor of 1 for self-modulation effects. Then, up to first non-linear order

$$K_{\{+\}[-]} = \begin{cases} k_{\mathrm{cell},0}\left(1 + \frac{1}{16}\left(\{1\}[2]\left|\frac{I_+(z)}{I_\mathrm{c}}\right|^2 + \{2\}[1]\left|\frac{I_-(z)}{I_\mathrm{c}}\right|^2\right)\right) & \text{if } z \text{ in TWPA section} \\ k_\mathrm{conn} & \text{else} \end{cases} \tag{5.10}$$

taking into account the cross-modulation between the forward- and backward-propagating waves. Here, $k_{\mathrm{cell},0} = \omega_\mathrm{w}\sqrt{\mathcal{L}_{\mathrm{cell},0}\mathcal{C}_\mathrm{cell}}$, the low-current wave number in the TWPA sections in the device. $k_\mathrm{conn} = \omega_\mathrm{w}\sqrt{\mathcal{L}_\mathrm{conn}\mathcal{C}_\mathrm{conn}}$.
If the loss is distributed uniformly over the device,

$$|I_+|^2 = \left|\frac{\tau_{\vec{0}\vec{\mathrm{d}}} I_{\mathrm{in},0}}{1 - \rho_{\vec{\mathrm{d}}\vec{\mathrm{d}}}\rho_{\vec{\mathrm{d}}\vec{\mathrm{d}}} \mathrm{e}^{-2r_\mathrm{d} l_\mathrm{d}}}\right|^2 \mathrm{e}^{-2r_\mathrm{d} z} \equiv |I_\mathrm{d}|^2 \mathrm{e}^{-2r_\mathrm{d} z} \tag{5.11}$$

$$|I_-|^2 = \left|\frac{\rho_{\vec{\mathrm{d}}\vec{\mathrm{d}}}\tau_{\vec{0}\vec{\mathrm{d}}} I_{\mathrm{in},0}}{1 - \rho_{\vec{\mathrm{d}}\vec{\mathrm{d}}}\rho_{\vec{\mathrm{d}}\vec{\mathrm{d}}} \mathrm{e}^{-2r_\mathrm{d} l_\mathrm{d}}}\right|^2 \mathrm{e}^{-2r_\mathrm{d}(2l_\mathrm{d}-z)} = \left|\rho_{\vec{\mathrm{d}}\vec{\mathrm{d}}} I_\mathrm{d}\right|^2 \mathrm{e}^{-2r_\mathrm{d}(2l_\mathrm{d}-z)}, \tag{5.12}$$

where τ and ρ are the transmission and reflection coefficients as indicated between the **d**evice and the 50 Ω-environment, which is indicated by a subscript 0. $I_{\mathrm{in},0}$ is the forward-propagating current entering the device, as would be measured in the 50 Ω-environment just before the device, i.e.

$$I_{\mathrm{in},0} = \sqrt{\frac{2P_{\mathrm{in},0}}{Z_{\mathrm{c},0}}}. \tag{5.13}$$

Although the transmission and reflection coefficients are affected by the non-linearity of the device due to their dependence on the device's characteristic impedance, the effect will only contribute to higher non-linear orders of the theory, such that we can treat the coefficient as constant. Then, $\tau_{\vec{0}\vec{\mathrm{d}}} \mapsto \tau$ and $\rho_{\vec{\mathrm{d}}\vec{\mathrm{d}}} = \rho_{\vec{0}\vec{\mathrm{d}}} \mapsto \rho$.

Substituting equation (5.10) into equation (5.8), we thus find

$$\begin{aligned}\Delta\phi_{\{+\}[-]} = {} & k_{\mathrm{conn}}\left(N_{\mathrm{S}}-1\right)l_{\mathrm{conn}} + k_{\mathrm{cell},0}N_{\mathrm{S}}N_{\mathrm{CS}}a + \\ & + \frac{k_{\mathrm{cell},0}}{32r_{\mathrm{d}}}\left|\frac{I_{\mathrm{d}}}{I_{\mathrm{c}}}\right|^2\left(\{1\}\,[2]E_+ + \{2\}\,[1]\rho^2\mathrm{e}^{-4r_{\mathrm{d}}l_{\mathrm{d}}}E_-\right)\end{aligned} \tag{5.14}$$

where, noting that $N_{\mathrm{S}}\left(N_{\mathrm{CS}}a + l_{\mathrm{conn}}\right) = l_{\mathrm{d}} - l_{\mathrm{conn}}$,

$$\begin{aligned}E_+ &\equiv \left(1-\mathrm{e}^{-2r_{\mathrm{d}}N_{\mathrm{CS}}a}\right)\sum_{n_{\mathrm{S}}=0}^{N_{\mathrm{S}}-1}\mathrm{e}^{-2r_{\mathrm{d}}n_{\mathrm{S}}\left(N_{\mathrm{CS}}a+l_{\mathrm{conn}}\right)} = \\ &= \left(1-\mathrm{e}^{-2r_{\mathrm{d}}N_{\mathrm{CS}}a}\right)\frac{\mathrm{e}^{-2r_{\mathrm{d}}\left(l_{\mathrm{d}}-N_{\mathrm{CS}}a\right)}\left(\mathrm{e}^{2r_{\mathrm{d}}\left(l_{\mathrm{d}}-l_{\mathrm{conn}}\right)}-1\right)}{\mathrm{e}^{2r_{\mathrm{d}}\left(N_{\mathrm{CS}}a+l_{\mathrm{conn}}\right)}-1}\end{aligned} \tag{5.15}$$

$$\begin{aligned}E_- &\equiv \left(\mathrm{e}^{2r_{\mathrm{d}}N_{\mathrm{CS}}a}-1\right)\sum_{n_{\mathrm{S}}=0}^{N_{\mathrm{S}}-1}\mathrm{e}^{2r_{\mathrm{d}}n_{\mathrm{S}}\left(N_{\mathrm{CS}}a+l_{\mathrm{conn}}\right)} = \\ &= \left(\mathrm{e}^{2r_{\mathrm{d}}N_{\mathrm{CS}}a}-1\right)\frac{\mathrm{e}^{2r_{\mathrm{d}}\left(l_{\mathrm{d}}-l_{\mathrm{conn}}\right)}}{\mathrm{e}^{2r_{\mathrm{d}}\left(N_{\mathrm{CS}}a+l_{\mathrm{conn}}\right)}-1} = \mathrm{e}^{2r_{\mathrm{d}}l_{\mathrm{d}}}E_+\end{aligned} \tag{5.16}$$

Inserting equation (5.14) into the wiggle frequency condition, $\Delta\phi_+ + \Delta\phi_- = 2\pi$, the wiggle frequency is found to be

$$\begin{aligned}\frac{\omega_{\mathrm{w}}}{2\pi} = {} & \Bigg(2v_{\mathrm{ph,conn}}^{-1}\left(N_{\mathrm{S}}-1\right)l_{\mathrm{conn}} + \\ & + v_{\mathrm{ph,cell},0}^{-1}\left(2N_{\mathrm{S}}N_{\mathrm{CS}}a + E_+\frac{\left|I_{\mathrm{d}}/I_{\mathrm{c}}\right|^2}{32r_{\mathrm{d}}}\left(3+3\rho^2\mathrm{e}^{-2r_{\mathrm{d}}l_{\mathrm{d}}}\right)\right)\Bigg)^{-1}\end{aligned} \tag{5.17}$$

up to first non-linear order.

To test this theory, we measure TWPA813 in transmission and in reflection while increasing the input power. The results of these measurements are shown in figures 5.18 and 5.19. The wiggles as observed in figure 5.16 are clearly moving as the input power is increased. Such a decrease of the wiggle frequency is expected from the non-linearity of the transmission line, i.e. the Josephson inductance, which increases with pump power.
From the transmission data we infer that the low-impedance solution found in previous section is correct. The amplitude of the wiggle present in the switching power of the device corresponds to the characteristic impedance of the device at this power. As can be observed in figure 5.18, this wiggle amplitude is approximately 2 dB, which is less than the 2.8 dB-wiggle amplitude observed for low-power transmission, see section 5.4.3. This implies that the characteristic impedance at the switching power has become closer to the 50 Ω-impedance of the environment. As $Z_{\mathrm{c,cell}} \propto \sqrt{L}$, we conclude that the low-impedance solution is correct.

The position of the transmission maxima in the frequency spectrum is most easily obtained from the reflection measurement, as a transmission maximum corresponds to a sharp reflection minimum. In this manner we extract the frequency of the four right-most transmission maxima in figure 5.18, corresponding to the 16th to the 19th overall transmission maxima. The wiggle frequency is obtained simply as $\omega_{\mathrm{w}} = \omega_{\mathrm{max},q}/q$, where $q \in \{16, 19\}$.
To compare theory and experiment we plot the expression $(\omega_{\mathrm{w},0}/\omega_{\mathrm{w}} - 1)$ in figure 5.20. Theoretically, from equation (5.17), this expression is given by

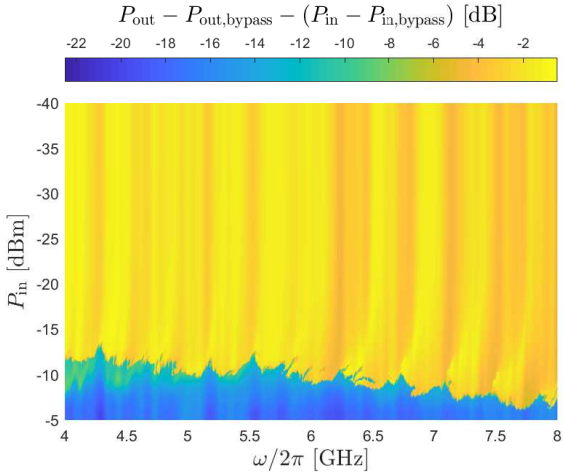
$$\frac{\omega_{\mathrm{w},0}}{\omega_{\mathrm{w}}} - 1 = \frac{E_+ \left|I_{\mathrm{d}}/I_{\mathrm{c}}\right|^2 \left(3 + 3\rho^2 \mathrm{e}^{-2r_{\mathrm{d}} l_{\mathrm{d}}}\right)}{64 r_{\mathrm{d}} \left(v_{\mathrm{ph,cell},0} v_{\mathrm{ph,conn}}^{-1} \left(N_{\mathrm{S}} - 1\right) l_{\mathrm{conn}} + N_{\mathrm{S}} N_{\mathrm{CS}} a\right)}. \tag{5.18}$$

where, from equations (5.11) and (5.13),

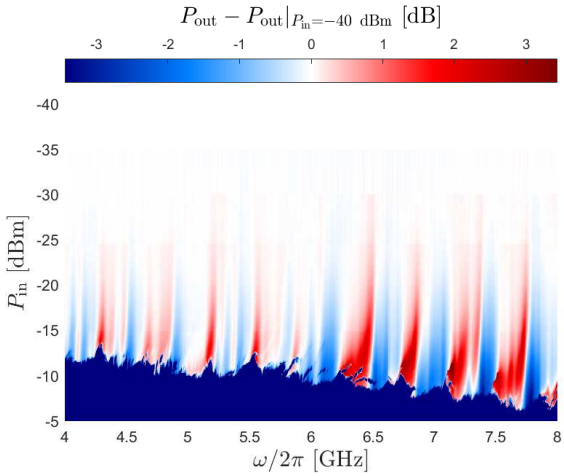
$$I_{\mathrm{d}} = \frac{\tau}{1 - \rho^2 \mathrm{e}^{-2r_{\mathrm{d}} l_{\mathrm{d}}}} \sqrt{\frac{2 \cdot 10^{\left(\left(P_{\mathrm{in,[dBm]}} - IL_{\mathrm{line,tot}}\right)/10 - 3\right)}}{Z_{\mathrm{c},0}}}. \tag{5.19}$$

Here, $IL_{\mathrm{line,tot}}$ is the total insertion loss of the set-up between the microwave source and the device. From the total line insertion loss, see equation (5.6), we estimate $IL_{\mathrm{line,tot}} = 55 \pm 1\,\mathrm{dB}$ and $IL_{\mathrm{TWPA}} = 0.35\,\mathrm{dB}$ where the error in $IL_{\mathrm{line,tot}}$ takes into account that the different microwave lines entering the dilution refrigerator may have a slightly different attenuation.

From a comparison of the theory and the experimental data we find that the critical current of 4.3 μA describes the data slightly better than a critical current of 9.5 μA. However, based on these measurements we cannot draw a firm conclusion on this matter. The main reason for uncertainty is the device loss. We estimated this loss at 0.35 dB in section 5.4.3, but, in fact, since there might be small differences in the lines entering the dilution refrigerator and we have no access to the losses within the PCB, a better estimate would be that

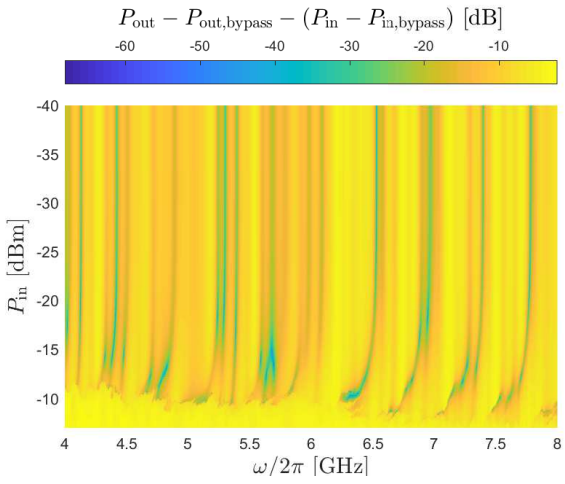


(a)

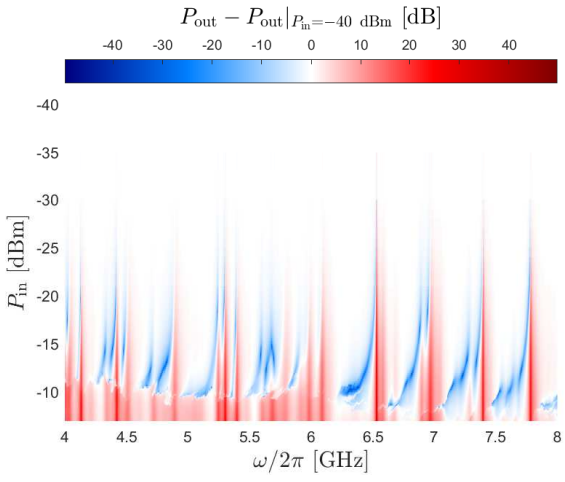


(b)

Figure 5.18: *Single-tone transmission of TWPA813 as function of frequency and input power. (a) Data scaled to the input power of the source and the measurement of the bypass line at* -40 dBm *input power. The wiggle frequency decreases due to the non-linear Josephson inductance. This process can be well-discerned in (b) in which we visualise the moving wiggles by subtracting the transmission output power at* -40 dBm *from all data.*



(a)



(b)

Figure 5.19: *Single-tone reflection of TWPA813 as function of frequency and input power. (a) Data scaled to the input power of the source and the measurement of the bypass line at* $-40\,\mathrm{dBm}$ *input power. The wiggle frequency decreases due to the non-linear Josephson inductance. (b) Visualisation of the moving wiggles by subtracting the transmission output power at* $-40\,\mathrm{dBm}$ *from all data.*

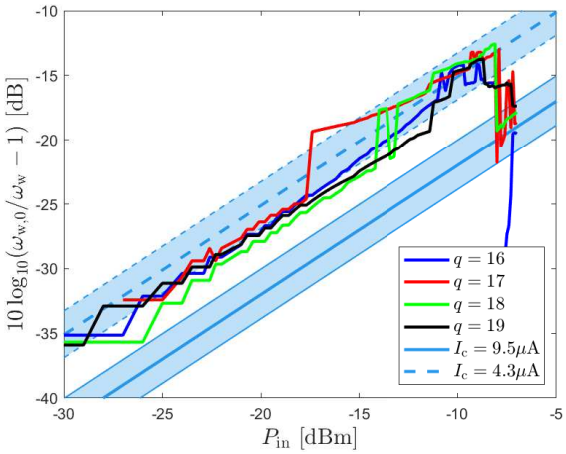


Figure 5.20: *Visualisation of the decreasing wiggle frequency in the transmission and reflection measurements in figures 5.18 and 5.19. We study the four right-most wiggles from these figures, which correspond to the* 16th *to* 19th *transmission maxima of the full frequency spectrum. The wiggle maxima correspond to the well-defined minima of the reflection measurement. The theory of equation (5.18) is plotted for both estimates of the critical current (*$I_c = 4.3 \pm 0.4 \vee 9.5 \pm 1.0\,\mu$A*).*

the device insertion loss is in between 0 and 1 dB ($0 \leq r_d \leq 5.6\,\mathrm{m}^{-1}$). Since the loss coefficient is inversely proportional to the factor $(\omega_{w,0}/\omega_w - 1)$ a small error in r_d influences the theoretical result to a great extent: a factor of 2 in r_d shifts the curves in figure 5.20 already by 3 dB. Furthermore, we do not know whether the loss coefficient is constant over the device, which yields another source of uncertainty in the theory.

From the observed switching power $P_{sw} \approx -9\,\mathrm{dBm}$ we determine the switching current of the device to be $I_{sw,+} = 2.7 \pm 0.4\,\mu$A by equation (5.19). This value equals $64 \pm 14\%$ or $29 \pm 7\%$ of the nominal critical current of $4.3 \pm 0.4\,\mu$A and $9.5 \pm 1.0\,\mu$A respectively. However, these numbers do only take into account the forward-propagating current. The switching current including both forward- and backward-propagating current, which is the total current flowing through a Josephson junction, is under the circumstances of transmission maxima maximised at the device port closest to the microwave source and is given by

$$I_{sw,tot} = I_{sw,+}\left(1 + \rho e^{-2r_d l_d}\right), \tag{5.20}$$

which amounts to $3.8 \pm 0.6\,\mu$A. Scaling the stated percentages by the same factor this equals $89 \pm 19\%$ or $40 \pm 10\%$ of the nominal critical currents of $4.3 \pm 0.4\,\mu$A or $9.5 \pm 1.0\,\mu$A. Of course, the obtained percentage cannot exceed 100%, which bounds the first stated value.

The observation that the switching current is not necessarily equal to the nominal

critical current can have several reasons. First, as found in section 5.3.1, our Josephson junctions are rather uniform in critical current, although there may be some outliers. Therefore, it could well be that some of the junctions have a lower critical current than the nominal critical current. The switching current of the device is determined by the junction with the lowest critical current and thus can be lower than the nominal critical current.
However, one can also think of more exotic explanations for this behaviour. One interaction, which has not been considered up to this point, is third harmonic generation. This effect appears in the Hamiltonian describing parametric amplification as $\hat{a}_{3\omega}^{\dagger}\,\hat{a}_{\omega}{}^{3}$, a term which describes the creation of a photon at $\omega = 3\omega_{\mathrm{p}}$ by annihilation of three photons at a frequency ω_{p}. The numerical factor in the coupled-mode equations belonging to this interaction equals $1/24$, see chapter 3, which is to be compared to the numerical factor of $1/16$ arising for the self-modulation interaction. Due to the phase mismatch between the modes at ω_{p} and $3\omega_{\mathrm{p}}$ the interaction is suppressed, however, it scales as the applied current I_{p}^{3}, instead of I_{p}^{2}, which would be the scaling for the generation of signal and idler photons if a signal would be present. Hence, third harmonic generation might be expected to play a non-negligible role in our measurements. The energy of the photons that are created due to third harmonic generation is in the order of $75\,\mu$eV if $\omega/2\pi = 6\,$GHz. Although this is not quite equal to the gap energy of the Josephson junctions, which was found to be $290\,\mu$eV for a single junction (figure 5.8) and $220\,\mu$eV for an array of junctions (figure 5.9), the energy of the photons created by third harmonic generation is a considerable fraction of this energy. Considering the fact that the third harmonic photons will mix again and generate photons of even higher frequency (although with a smaller probability), it is imaginable that these effects decrease the switching current of TWPAs as compared to the nominal critical current.

It should be noted that these results were obtained using many assumptions and estimations. Most importantly, we neglected the internal reflections of the device. The precise effect of this assumption has not been studied. The critical current of the device could have been obtained by a straightforward IV-measurement of the device. This measurement has not been performed. Thirdly, for the losses in the device we assumed a constant loss coefficient and a total loss of $0.35\,$dB. These assumptions influence the theoretical outcomes to a great extent, but were not obtained from direct measurement. A better estimate of the total device loss can be obtained by using two microwave switches. Placing the device in one channel between the switches and a bypass line in another, the uncertainty in input line insertion loss is removed.
However, even in this case one still obtains the device loss plus the losses in the PCB and connectors. One may disentangle the loss within the sample by performing a calorimetric experiment using a dual compensated calorimeter [24]. In such a measurement the device should be put on the sample bath of such a calorimeter, whereas the PCB is connected to the reference bath. The two baths are thermally weakly coupled via the Al wire bonds between the device

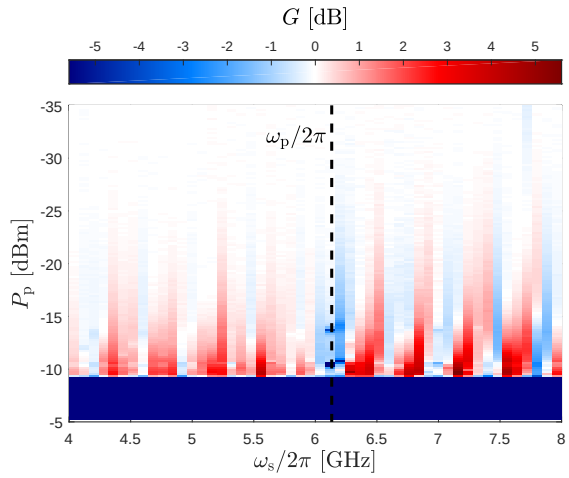
and the PCB. If this coupling proves to be insufficient the thermal resistivity between the two baths can be increased by additional thermal links. We believe that in this way, the total device loss can be extracted reliably.
Using this method one can estimate the loss in the TWPA sections by performing a second measurement. In this measurement, one puts a device on the sample bath that only contains the CPW. The difference in extracted loss rates between these two measurements will be a measure for the average loss coefficient in the TWPA sections.

An insertion loss of approximately 0.7 dB for 689 Josephson junctions is comparable to Josephson TWPAs described in literature: [2] finds 0.5 dB of insertion loss for a device with 663 Josephson junctions and [3] reports a loss of 2.5 dB (at $\omega = 7\,\mathrm{GHz}$) for a TWPA containing 2037 junctions. This implies that our approach of increasing the capacitance using low air bridges in this device does only reduce the device losses if the actual insertion loss of the device would be significantly less than 0.7 dB.

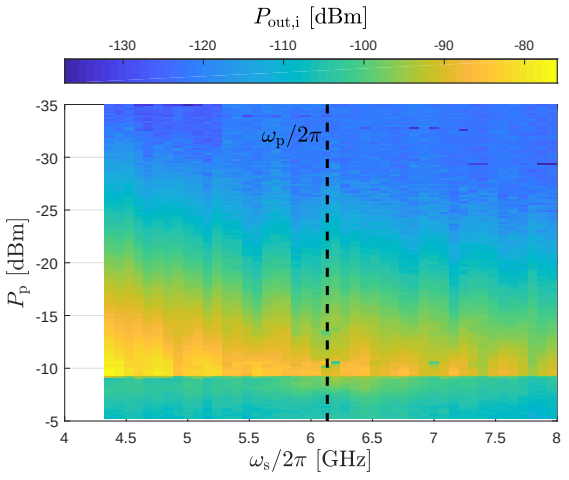
5.4.4 Results – double-tone excitation

In case we feed the TWPA device with a double-tone excitation, a pump and a signal, we can study the amplifier properties of TWPA813. Using the set-up depicted in figure 5.15, we can characterise the device in two manners: in case we use the pump generator and the signal generator, we can measure the power in the signal and idler mode using the spectrum analyser, whereas if we use the pump and tracking generator we can only study the behaviour of the signal mode resulting from transmission through the sample.
In this section we will only consider the measurements without developing a theory that describes the measurements. Such a theory would include losses and reflections for the three different modes of the field (actually six, because of the reflections). In principle, this can be developed by extending the single-tone reflection theory presented in last section by cross modulations between the pump (right-moving and left-moving) on the one hand, and signal and idler (both right-moving and left-moving) on the other. Furthermore, the different amplification coupling constants conserving both energy and momentum should be evaluated for the six modes.

In figure 5.21 we present a typical measurement using the pump and signal generators. Setting the pump frequency at 6.133 GHz we measure the output power in the signal and idler mode varying the pump power and signal frequency. We plot the signal gain, defined as $G = P_{\mathrm{out,s}} - P_{\mathrm{out,s0}}$ of the device, where $P_{\mathrm{out,s0}} = P_{\mathrm{out,s}}|_{P_{\mathrm{p}}=-39\,\mathrm{dBm}}$, as well as the measured power in the idler mode. It can be observed how the gain and idler power increase with pump power, as expected from the theory. However, the gain is also found to be less than unity for certain frequency ranges. This can be explained by the two contributions to the gain measurement. First, we have the direct gain given by the conversion of pump photons into signal and idler photons. However, due to modulation



(a)



(b)

Figure 5.21: *Double-tone measurement results using the pump generator (varying power) and the signal generator (varying frequency). The pump is at a fixed frequency of* 6.133 GHz*, indicated by the dashed lines. The signal generator is at a fixed power of* -50 dBm*. (a) Measuring with the spectrum analyser at* $\omega = \omega_s$ *we extract the gain* $G = P_{out,s} - P_{out,s0}$ *of the device, where* $P_{out,s0} = P_{out,s}|_{P_p=-39\,\text{dBm}}$*. The gain results from wiggle gain due to the moving wiggles, as well as non-linear gain due to wave mixing. (b) Measuring at* $\omega = 2\omega_p - \omega_s = \omega_i$ *we obtain the power generated in the idler mode due to wave mixing. Measurements for which* $\omega_i/2\pi > 8$ GHz *are excluded from the plot because of the bandwidth of the circulator and HEMT amplifier being* 4 *to* 8 GHz*.*

effects in the device we also have a contribution due to the moving wiggles, the wiggle gain. The former gain always contributes in excess of unity, whereas the latter contribution can be both larger and smaller than unity.

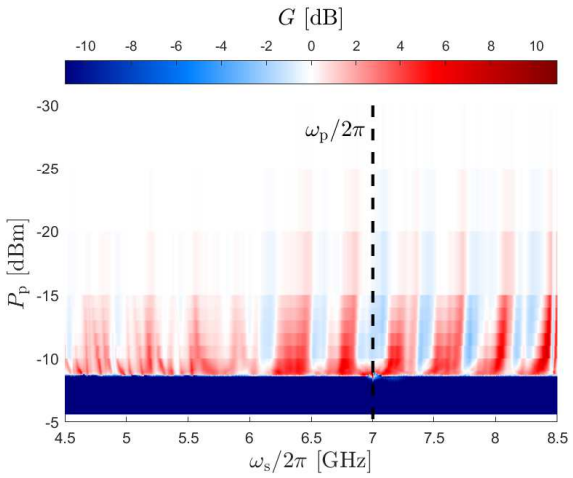


Figure 5.22: *Double mode measurement results using the pump (varying power, $\omega_p/2\pi = 7\,\mathrm{GHz}$) generator and tracking generator as signal ($P_s = -30\,\mathrm{dBm}$). The signal gain is determined as $G = P_{out,s} - P_{out,s}|_{pump\ off}$ and results from non-linear gain as well as wiggle gain.*

The same behaviour is observed in figure 5.22, which was measured using the pump generator at 7 GHz with varying power and the tracking generator as signal at −30 dBm. Interestingly, upon comparison with figure 5.16, we find a gain minimum around the pump frequency if it falls in a low-power transmission minimum, whereas a gain maximum is observed around the pump frequency in case it is chosen in a low-power transmission maximum.

From these measurements we find that TWPA813 can provide 10 dB of gain in case the pump and signal frequencies are chosen well. The gain heavily depends on both frequencies, because of the impedance mismatch of the device with its 50 Ω-environment, which therefore should be improved for a flatter gain spectrum. The gain can be enlarged by improving the phase matching between the transmitting modes and increasing the number of Josephson junctions embedded in the transmission line and increasing the total length of the device accordingly.

5.5 Conclusions

In this chapter we presented the design, fabrication and measurement procedure of our developed TWPAs. Our goal was to design a device that was matched to the 50 Ω-environment of typical microwave set-ups and provides gain at a

low intrinsic insertion loss. We have developed the O-type Josephson junction in two types: The R-mask type is defined by the resist, whereas the E-mask type is defined by the junction electrodes. It was found that R-mask type junctions have better properties in terms of critical current distribution than E-mask type junctions. In fact, unless the uniformity is improved, the latter type is not usable for the development of TWPAs. Secondly, we developed the low air bridge to increase the capacitance of the TWPA. It was found that Al can be used for this purpose. We have not been able to succeed in developing NbTiN air bridges for TWPAs, which would be stiffer and possibly more reliable. Depositing the NbTiN caused the Josephson junctions to be severely damaged.

We presented one of the successful devices, TWPA813, in detail. From single-tone measurements at low power we determined the device characteristics. Most notably, the characteristic impedance was found to be $23 \pm 2\,\Omega$ and the phase velocity was extracted as $1.31 \pm 0.01 \times 10^7$ m/s. Moreover, modelling the device using the matrix transfer method it was found that the boundaries between the TWPA sections and the CPW connections that connect the sections are to be taken into account explicitly. Comparing the estimated insertion loss of our device to values reported in literature, we did not find a significant decrease as projected. However, this estimate was obtained by indirect methods. A direct measurement should be performed to draw a conclusion on this matter.
We studied the non-linear behaviour of the device and developed a model to theoretically describe the interference wiggles, that arise as a result of the impedance mismatch between the device and its environment. This model depends critically on the loss coefficient of the device to which we have no experimental access.
Finally we performed double-tone experiments to study the gain behaviour of the device. The device was able to deliver a maximum of 10 dB of gain, which results from the combination of direct (non-linear) gain and a shift in the transmission maxima.

In order to improve the device and measurement analysis, the impedance matching of the device to its $50\,\Omega$-environment needs to be improved. This can be done by using smaller Josephson junctions (increase inductance) or increasing the air bridge height (decrease capacitance). It is beneficial to determine the critical current (distribution) of the device before studying its non-linear behaviour, e.g. by measuring its IV-curve. Furthermore, using microwave switches a better estimate of the insertion loss of the device can be obtained. Even better in this respect would be the use of a dual compensated calorimeter.

Acknowledgements

The results presented in this chapter have been obtained in the group of L. DiCarlo at Delft university of Technology. We are very grateful to A. Bruno and L. DiCarlo for the close collaboration.

References

[1] B. Ho Eom, P. K. Day, H. G. LeDuc, and J. Zmuidzinas. A wideband, low-noise superconducting amplifier with high dynamic range. *Nature Phys.*, 8:623–627, 2012.

[2] T. C. White, J. Y. Mutus, I.-C. Hoi, R. Barends, B. Campbell, Y. Chen, Z. Chen, B. Chiaro, A. Dunsworth, E. Jeffrey, J. Kelly, A. Megrant, C. Neill, P. J. J. O'Malley, P. Roushan, D. Sank, A. Vainsencher, J. Wenner, S. Chaudhuri, J. Gao, and J. M. Martinis. Traveling wave parametric amplifier with josephson junctions using minimal resonator phase matching. *Appl. Phys. Lett.*, 106:242601, 2015.

[3] C. Macklin, K. O'Brien, D. Hover, M. E. Schwartz, V. Bolkhovsky, X. Zhang, W. D. Oliver, and I. Siddiqi. A near–quantum-limited josephson traveling-wave parametric amplifier. *Science*, 350:307–310, 2015.

[4] M. R. Vissers, R. P. Erickson, H.-S. Ku, L. Vale, X. Wu, G. C. Hilton, and D. P. Pappas. Low-noise kinetic inductance traveling-wave amplifier using three-wave mixing. *Appl. Phys. Lett.*, 108:012601, 2016.

[5] A. A. Adamyan, S. E. de Graaf, S. E. Kubatkin, and A. V. Danilov. Superconducting microwave parametric amplifier based on a quasi-fractal slow propagation line. *J. Appl. Phys.*, 119:083901, 2016.

[6] S. Chaudhuri, D. Li, K. D. Irwin, C. Bockstiegel, J. Hubmayr, J. N. Ullom, M. R. Vissers, and J. Gao. Broadband parametric amplifiers based on nonlinear kinetic inductance artificial transmission lines. *Appl. Phys. Lett.*, 110:152601, 2017.

[7] C. M. Caves. Quantum limits on noise in linear amplifiers. *Phys. Rev. D*, 26:1817–1839, 1982.

[8] S. Alexandrou, R. Sobolewski, and T. Y. Hsiang. Bend-induced even and odd modes in picosecond electrical transients propagated on a coplanar waveguide. *Appl. Phys. Lett.*, 60(15):1836–1838, 1992.

[9] Chung-Yi Lee, Yaozhong Liu, and Tatsuo Itoh. The effects of the coupled slotline mode and air-bridges on CPW and NLC waveguide discontinuities. *IEEE Trans. Microw. Theory Tech.*, 43:2759–2765, 1995.

[10] Jongjoo Lee, Heeseok Lee, Woopoung Kim, Jaehoon Lee, and Joungho Kim. Suppression of coupled-slotline mode on CPW using air-bridges measured by picosecond photoconductive sampling. *IEEE Microw. Guid. Wave Lett.*, 9:265–267, 1999.

[11] G. E. Ponchak, J. Papapolymerou, and M. M. Tentzeris. Excitation of coupled slotline mode in finite-ground CPW with unequal ground-plane widths. *IEEE Trans. Microw. Theory Tech.*, 53:713–717, 2005.

[12] Sonnet software. https://www.sonnetsoftware.com. Accessed: Dec. 7, 2018.

[13] G. J. Dolan. Offset masks for lift-off photoprocessing. *Appl. Phys. Lett.*, 31:337–339, 1977.

[14] IVVI rack. http://qtwork.tudelft.nl/~schouten/ivvi/index-ivvi.htm. Accessed: Dec. 7, 2018.

[15] E. Ben-Jacob, D. J. Bergman, B. J. Matkowsky, and Z. Schuss. Lifetime of oscillatory steady states. *Phys. Rev. A*, 26:2805–2816, 1982.

[16] S. V. Lotkhov, E. M. Tolkacheva, D. V. Balashov, M. I. Khabipov, F.-I. Buchholz, and A. B. Zorin. Low hysteretic behavior of $Al/AlO_x/Al$ josephson junctions. *Appl. Phys. Lett.*, 89:132115, 2006.

[17] A. V. Shcherbakova, K. G. Fedorov, K. V. Shulga, V. V. Ryazanov, V. V. Bolginov, V. A. Oboznov, S. V. Egorov, V. O. Shkolnikov, M. J. Wolf, D. Beckmann, and A. V. Ustinov. Fabrication and measurements of hybrid Nb/Al josephson junctions and flux qubits with π-shifters. *Supercond. Sci. Technol.*, 28:025009, 2015.

[18] D. J. Thoen, B. G. C. Bos, E. A. F. Haalebos, T. M. Klapwijk, J. J. A. Baselmans, and A. Endo. Superconducting NbTiN thin films with highly uniform properties over a $\varnothing$ 100 mm wafer. *IEEE Trans. Appl. Supercond.*, 27:1–5, 2017.

[19] C. Song, M. P. DeFeo, K. Yu, and B. L. T. Plourde. Reducing microwave loss in superconducting resonators due to trapped vortices. *Appl. Phys. Lett.*, 95:232501, 2009.

[20] D. Bothner, T. Gaber, M. Kemmler, D. Koelle, and R. Kleiner. Improving the performance of superconducting microwave resonators in magnetic fields. *Appl. Phys. Lett.*, 98:102504, 2011.

[21] D. Bothner, C. Clauss, E. Koroknay, M. Kemmler, T. Gaber, M. Jetter, M. Scheffler, P. Michler, M. Dressel, D. Koelle, and R. Kleiner. Reducing vortex losses in superconducting microwave resonators with microsphere patterned antidot arrays. *Appl. Phys. Lett.*, 100:012601, 2012.

[22] B. Chiaro, A. Megrant, A. Dunsworth, Z. Chen, R. Barends, B. Campbell, Y. Chen, A. Fowler, I. C. Hoi, E. Jeffrey, J. Kelly, J. Mutus, C. Neill, P. J. J. O'Malley, C. Quintana, P. Roushan, D. Sank, A. Vainsencher, J. Wenner, T. C. White, and J. M. Martinis. Dielectric surface loss in superconducting resonators with flux-trapping holes. *Supercond. Sci. Technol.*, 29:104006, 2016.

[23] S. Krinner, S. Storz, P. Kurpiers, P. Magnard, J. Heinsoo, R. Keller, J. Luetolf, C. Eichler, and A. Wallraff. Engineering cryogenic setups for 100-qubit scale superconducting circuit systems. *Arxiv*, 1806.07862, 2018.

[24] H. Kajastie, K. K. Nummila, A. Rautiainen, K. Riski, and A. Satrapinski. Loss measurements on superconducting Nb by a cryogenic dual compensated calorimeter for the implementation of the kilogram standard by the levitation mass method. *Metrologia*, 45:68–74, 2008.

Acknowledgements

No PhD is an island. It is therefore that I would like to take the opportunity to express my gratitude to all who supported and helped me, knowingly and unknowingly, during the past four years.
First and foremost, thank you, Tjerk! I am very grateful for your guidance and advice, and the freedom you gave me to choose my own problems to work on. You gave me the opportunity to think about and work on a topic, which, I think, is one of the most interesting problems in contemporary physics: the quantum measurement problem. I would also like to thank you for your support when I needed to get my head out of research for a bit, and for inviting me to explore my limits a little further.
Thank you, Oosterkamp-group! Arthur, Bob, Gesa, Jelmer, Louk, Lucia, Marc and Martin, you brought colour and joy to the group. The random and less-random discussions we had during lunch, the group outings and, most of all, our epic journey to Iceland, Canada and the United States are memories making me smile, while crossing my mind. Here, I would also like to thank all students that worked in the group, especially Xavier and Ruben, who worked with me on the results presented in chapter 4. Also, thank you, Max, for all the nice discussions we had about ice skating. Last but not least, thank you, Ellie, for taking care of all the non-science related issues in the group.
Thank you, DiCarlo-group! Leo, I am grateful for your hospitality. Alessandro, thank you for showing me the ropes in the cleanroom and all the discussions we had on the design of travelling-wave parametric amplifiers and cleanroom issues. But most of all, thanks for always having a positive attitude. Jacob, I really enjoyed our after-lunch walks around campus.
Thank you, Michiel, Gerard and Wolfgang! It was great that your doors were always open for discussions on quantum optics.
Thank you, Bert, Merlijn and Gert! By providing technical support, you literally made the experiments in Leiden work. It was always nice to scooter to the new Gorlaeus building for a question on quick fixes or a more elaborate discussion on microwave technology or designed parts.
And last, but not least, I would like to thank my parents and siblings Els, Bas and Klaartje, and, of course, Franka. You were always there for me to listen to my stories and to stroke my head gently when it was most needed.

Samenvatting

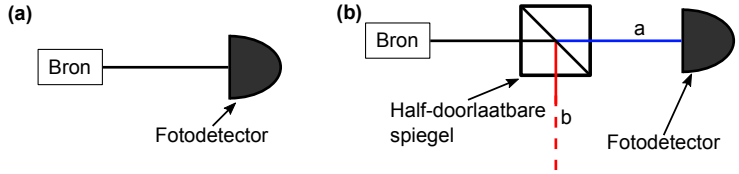
In de zogenaamde Kopenhaagse interpretatie van de kwantummechanica wordt een duidelijk onderscheid gemaakt tussen de macroscopische en de microscopische wereld. De eerste is de wereld zoals wij mensen haar kennen en wordt beschreven door de klassieke mechanica. De tweede is de wereld van elementaire deeltjes, atomen en moleculen of kleine verzamelingen daarvan, en wordt beschreven met kwantummechanica.
Deze twee beschrijvingen geven een totaal ander beeld van de fysische werkelijkheid. Waar de klassieke mechanica deterministisch is en de evolutie van systemen geheel kan worden beschreven met gebruik van de wetten van Newton, wordt – in ieder geval vanuit menselijk oogpunt – de kwantummechanica geregeerd door kansen. Dat, terwijl de kwantummechanica op zich ook geheel deterministisch is en de evolutie van systemen volledig kan worden beschreven door de (unitaire) Schrödingervergelijking.

Het moge duidelijk zijn dat het wringt op het raakvlak tussen de klassieke mechanica en kwantummechanica: beide theorieën zijn inherent deterministisch, maar toch lijkt het vanuit menselijk perspectief alsof de kwantummechanica probabilistisch is. Het raakvlak tussen beide theorieën is het duidelijkst te illustreren aan de hand van het concept "meting". Stel, men neme een bron van individuele fotonen (lichtdeeltjes) en laat de uittredende fotonen op een fotodetector vallen, zoals weergegeven in figuur 1a. Dan moge het niet verrassend zijn dat de fotodetector een "klikje" geeft, elke keer als er een foton wordt uitgezonden door de bron en ontvangen door de detector.

Echter, zetten we nu een half-doorlaatbare spiegel in het pad tussen de bron en de detector, zoals in figuur 1b, dan geraakt het foton in een superpositie die als volgt beschreven kan worden,

$$|\psi\rangle = \frac{1}{\sqrt{2}} \left(|1\rangle_{\mathrm{a}} |0\rangle_{\mathrm{b}} + |0\rangle_{\mathrm{a}} |1\rangle_{\mathrm{b}} \right). \tag{1}$$

In deze vergelijking zijn a en b de uitgangsarmen van de half-doorlaatbare spiegel. $|1\rangle_{\mathrm{a}} |0\rangle_{\mathrm{b}}$ geeft weer dat het foton in arm a zit, terwijl arm b geen foton bevat. Het omgekeerde geldt voor de term $|0\rangle_{\mathrm{a}} |1\rangle_{\mathrm{b}}$. Tenslotte geeft de factor



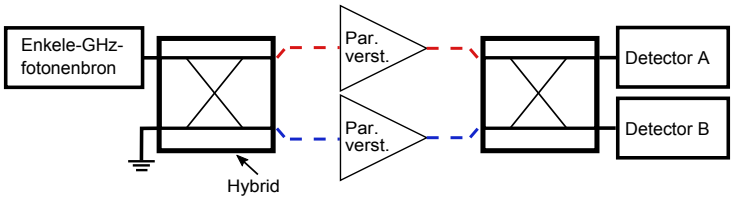
Figuur 1: *Schematische weergave van een experiment om het kwantummeetprobleem toe te lichten. (a) Wanneer een bron van individuele fotonen gericht wordt op een fotodetector, produceert de detector een "klikje" voor ieder ontvangen foton. (b) Indien er een half-doorlaatbare spiegel tussen bron en detector wordt geplaatst zou men op basis van de unitariteit van de Schrödingervergelijking voorspellen dat de detector een superpositie aanneemt van een "klikje" en een "geen-klikje". Dit wordt echter nooit waargenomen.*

$1/\sqrt{2}$ in de vergelijking aan dat de kans om het foton te meten in elk van de armen gelijk is aan $1/2$.
De deterministische Schrödingervergelijking zou nu voorspellen dat de detector – laten we aannemen dat deze 100% efficiënt is, hetgeen betekent dat voor ieder binnenkomend foton precies één klikje geproduceerd wordt – een superpositie zou moeten aannemen van een klikje (het foton is gedetecteerd) en een "geen-klikje" (het foton is niet gedetecteerd). Bij metingen aan kwantumsystemen wordt zo'n superpositie echter nooit waargenomen. In plaats daarvan zal de detector óf klikken óf niet-klikken – met andere woorden: de meting aan het systeem laat de toestand van het systeem instorten naar één van de mogelijke uitkomsten. Het feit dat dit proces niet door de Schrödingervergelijking beschreven wordt, wordt het kwantummeetprobleem genoemd.

Er zijn verschillende interpretaties van het kwantummeetprobleem. Hoewel ze alle totaal verschillend zijn, zijn ze het eens over het volgende: "grote" systemen gedragen zich klassiek, terwijl "kleine" systemen kwantummechanisch gedrag kunnen vertonen. Wat de woorden "groot" (macroscopisch) en "klein" (microscopisch) hier precies betekenen is niet duidelijk, maar men is het erover eens dat een meetinstrument "groot" is (immers, een meetinstrument zoals de fotodetector uit de vorige paragraaf zal altijd een enkele meetuitkomst geven). Echter, hierdoor kan men zich even goed afvragen wat precies een "meting" is.

In dit proefschrift stellen we een experiment voor dat deze vraag misschien kan beantwoorden. Specifieker, we vragen ons af of een elektronische microgolfversterker een kwantumtoestand zal laten instorten. Immers, in meetinstrumenten zoals fotodetectoren is dikwijls een versterkingsmechanisme ingebouwd. Het heeft verschillende voordelen om een elektronische versterker te gebruiken. Ten eerste, aangezien men vermoedt dat massa sterk bijdraagt aan de "grootte" van een systeem, wordt door middel van een elektronische versterker direct massa toegevoegd aan het experiment. Deze massa komt van de elektronen die zich als stromen door de versterker bewegen. Ten tweede staat het ons vrij om supergeleiding toe te passen, welke een sterke ontkoppeling van de omgeving

garanderen in het microgolfregime en bij zeer lage temperaturen – een van de vereisten voor successvolle kwantumexperimenten. Verder eisen we van de versterker dat deze weinig ruis genereert en een aanpasbare versterkingsfactor heeft.
Aan al deze voorwaarden kan worden voldaan door de zogenaamde microgolf parametrische versterkers. Deze versterkers werken op hetzelfde principe als waarop schommels werken. Op een schommel beweegt men zijn benen om de schommel een grotere schommelamplitude te geven. Wat er hier gebeurt is dat men door het bewegen van zijn benen voortdurend zijn zwaartepunt (de parameter) wat verplaatst. Door deze verplaatsing raken de beweging van de benen (grote amplitude) en schommel (kleine amplitude) gekoppeld, waardoor er bewegingsenergie van de benen naar de schommel gepompt wordt.



Figuur 2: *Schematische weergave van het in dit proefschrift voorgestelde experiment. Individuele microgolffotonen worden door middel van een* hybrid *(microgolf-analoog van een half-doorlaatbare spiegel) in een toestand van superpositie gebracht, zoals beschreven in vergelijking (1). Deze toestand wordt versterkt door twee parametrische versterkers. Vervolgens kan, door gebruik te maken van een tweede* hybrid*, de interferentie van de uitgangssignalen van beide versterkers bestudeerd worden met behulp van detectoren A en B.*

Het idee is nu om twee van deze parametrische versterkers toe te voegen aan elk van beide armen van een interferometer, zie figuur 2. Deze interferometer wordt gevormd door twee half-doorlaatbare spiegels (*hybrids* genoemd binnen de microgolftechnologie), waarvan de ingangskanalen van de laatste spiegel gekoppeld zijn aan de uitgangskanalen van de eerste spiegel. Als we deze interferometer nu voeden met één enkel microgolffoton ontstaat er achter de eerste half-doorlaatbare spiegel een superpositie, zoals weergegeven in vergelijking (1). Deze kwantumtoestand wordt versterkt door beide versterkers en middels de tweede half-doorlaatbare spiegel kunnen we de kwantuminterferentie van de uitgangssignalen van de versterkers in de beide interferometerarmen bestuderen. De hoop is dat deze interferentie ons zal vertellen of de toestand zich in de interferometer volgens de wetten van de kwantummechnica heeft gedragen, of dat er een instorting van de golffunctie heeft plaatsgehad, doordat de versterkers fungeren als detectoren.

Dit proefschrift beschrijft de eerste stappen naar het voorgestelde experiment. Na een algemene inleiding, bespreken we in hoofdstuk 2 enkele belangrijke elementen van de microgolftechologie die van belang zijn voor het verdere proef-

schrift. In dit licht behandelen we transmissielijnen en microgolfresonatoren. Verder ontwikkelen we in dit hoofdstuk een theorie om de eigenschappen van een transmissielijn te bepalen die aangesloten is op een netwerk van transmissielijnen met een verschillende karakteristieke impedantie. Deze theorie stoelt op microgolfreflecties, ontstaan door het verschil in karakteritieke impedantie. Echter, ook microgolfcomponenten die qua specificatie gelijk zijn in impedantie aan het netwerk kunnen nog kleine reflecties veroorzaken. In hoofdstuk 2 illustreren we op basis hiervan hoe de fysieke lengte van deze componenten verkregen kan worden.
In hoofdstuk 3 wordt de theorie die parametrische versterkers beschrijft besproken, in het bijzonder die van lopende-golf parametrische versterkers gebaseerd op Josephson juncties. Deze juncties kunnen beschreven worden als een stroomafhankelijke inductie, waardoor stromen bij verschillende frequenties gekoppeld worden, analoog aan de koppeling die plaatsvindt bij het schommelen. In dit hoofdstuk wordt in eerste instantie de benodigde terminologie geïntroduceerd, waarna de klassieke theorie kort aan bod komt. Dan leiden we een kwantumtheorie af voor de versterkers met speciale aandacht voor de verschillende aannamen die gedaan worden. Dit resulteert in een Hamiltoniaan op basis waarvan we de klassieke theorie nogmaals afleiden en we bespreken de verschillen tussen beide aanpakken. Tenslotte besteden we in dit hoofdstuk aandacht aan de geldigheid van de theorie.
Het proefschrift wordt vervolgd door berekeningen aan het voorgestelde experiment in hoofdstuk 4. Door middel van analytische en numerieke methoden bepalen we de verwachte zichtbaarheid van het interferentiepatroon voor het geval de versterkers zich gedragen volgens de kwantummechanica. We tonen aan dat deze zichtbaarheid niet verdwijnt als functie van de versterking en ook niet wanneer er verliezen aan het model worden toegevoegd. Dan bespreken we twee gevallen waarop het instorten van de kwantumtoestand in de interferometer zich zou kunnen manifesteren. Hieruit volgt dat we, in het geval dat de toestand instort naar een exact aantal fotonen (een aantallentoestand), mogen verwachten dat de interferentiezichtbaarheid verdwijnt. Als we er echter vanuit gaan dat de toestand instort naar een (klassieke) sinusoïde (een coherente toestand), dan verdwijnt de interferentiezichtbaarheid niet, maar zal hij zich toch anders gedragen dan de unitaire kwantummechanica voorspelt. Het hoofdstuk wordt afgesloten met enkele opmerkingen over de uitvoerbaarheid en uitvoering van het experiment.
Tenslotte, in hoofdstuk 5, bespreken we onze experimentele voortgang op het gebied van lopende-golf parametrische versterkers. We gaan in op het ontwerpen van dergelijke versterkers en op de fabricage ervan. In het bijzonder lichten we de fabricage van de Josephson juncties toe, waarvoor we twee eigen ontwerpen introduceren. We tonen aan dat het ene ontwerp geschikter is voor de fabricage van versterkers dan het andere. Ook lichten we de fabricage van “lage” luchtbruggen toe – het andere noodzakelijke element in ons versterkerontwerp. Na deze cruciale onderwerpen bespreken we de meetopstelling en de metingen aan een preparaat. We bepalen de transmissielijnparameters (in het bijzonder

de kritieke stroom van de juncties en de effectieve hoogte van de luchtbruggen) en meten aan het niet-lineaire gedrag van het preparaat in aanwezigheid van microgolfreflecties. Tenslotte bepalen we de versterking die het preparaat verschaft en vinden dat deze kan oplopen tot ongeveer 10 dB.

Curriculum vitae

Thomas Hendrik Abraham (Tom) van der Reep was born on 25 October 1989 in Rotterdam, where he also grew up. After graduating from the Marnix Gymnasium in Rotterdam in 2008, he started his studies in Aerospace Engineering at Delft University of Technology. He obtained his BSc-degree *cum laude* after a feasibility study for an asteroid sample-return mission, performed with a group of 9 other students under supervision of Ir. R. Noomen.
Following this, Tom switched his field of studies towards Physics, in which he obtained a BSc-degree *cum laude* at Leiden University. During his studies, he worked under supervision of Prof. dr. J. Aarts and Prof. dr. ir. S.J. van der Molen on the question whether a study of magnetic phenomena using a low-energy electron microscope could be a fruitful endeavour. During this research project, he used magnetic vortex disks as a specific physical system.
Continuing his studies in Physics, Tom enrolled in the MSc-programme at Leiden university, in which he followed the Casimir pre-PhD-track. During his MSc-studies, he performed three research projects. First, he worked under supervision of Dr. D.F.E. Samtleben at Nikhef on the expected distinguishability of shower-like and track-like events within the ORCA experiment, a study which was necessary in view of a proposed experiment to shed light on the neutrino mass hierarchy. Secondly, Tom worked under supervision of Dr. M. Blaauwboer at Delft University of Technology, performing a theoretical study into the effects of noise in reference-frame-independent quantum key distribution, in light of eavesdropping. Finally, he worked under supervision of Prof. dr. ir. T.H. Oosterkamp on the skating project, which aims to measure the thickness of the water layer that supposedly forms while an ice skate slides over a layer of ice.
Tom completed his MSc-studies *cum laude* in 2014 by writing a PhD-research proposal. After the proposal was granted, he pursued a PhD under supervision of Prof. dr. ir. T.H. Oosterkamp. During his PhD, he made the initial steps towards an experiment that aims to entangle two parametric amplifiers in order to study whether such amplifiers could give rise to spontaneous wavefunction collapse – in other words, whether such amplifiers turn into detectors at a large gain. He worked on the development of travelling-wave parametric amplifiers using Josephson junctions and built a microwave set-up to characterise the devices. The former work was done at Delft University of Technology in close

collaboration with Dr. A. Bruno and Prof. dr. L. DiCarlo. Furthermore, Tom worked on the quantum description of travelling-wave parametric amplifiers and on the theoretical description and expected output of the proposed experiment, specifically in the presence of quantum state collapse.

In his spare time, Tom enjoys singing, hiking, reading and riding his bicycle.

List of publications

1. T.H.A. van der Reep. A mesoscopic Hamiltonian for Josephson travelling-wave parametric amplifiers. *Submitted*, arXiv:1812.05907 (2018).
2. T.H.A. van der Reep, L. Rademaker, X.G.A. Le Large, R.H. Guis, T.H. Oosterkamp. An experimental proposal to study spontaneous collapse of the wave function using two travelling-wave parametric amplifiers. *Submitted*, arXiv:1811.01698 (2018).
3. L. Rademaker, T. van der Reep, N. Van den Broeck, B. van Waarde, M. de Voogd, T. Oosterkamp. The instability of a quantum superposition of time dilations. arXiv:1410.2303 (2014).